High Throughput Microfluidic Technologies for Cell Separation and Single-Cell Analysis

by

Lidan Wu

B.S. Biology, University of Science and Technology of China (2010)

Submitted to the Department of Biological Engineering
In Partial Fulfillment of the Requirements for the Degree of

Doctor of Philosophy

at the

MASSACHUSETTS INSTITUTE OF TECHNOLOGY

February 2016

Signature of Author: Signature redacted
Department of Biological Engineering
Jan 8, 2016

Certified by: Signature redacted
Jongyoon Han
Professor of Electrical Engineering and Computer Science
Professor of Biological Engineering
Thesis Supervisor

Accepted by: Signature redacted
Forest M. White
Chairman, Graduate Program Committee
Professor of Biological Engineering

High Throughput Microfluidic Technologies for Cell Separation and Single-Cell Analysis

by

Lidan Wu

Submitted to the Department of Biological Engineering
on Jan 8th, 2016, in partial fulfillment of the
requirements for the degree of
Doctor of Philosophy in Biological Engineering

Abstract

The heterogeneity of individual cellular behavior in response to physical and chemical stimuli has raised increasing attention in many biological processes. There is great incentive in developing techniques for high throughput single-cell measurements and manipulations. Particularly, cell size has been recognized as an important parameter in single cell study and pericellular protease activity plays a key role in regulating the microenvironment of individual cells. Therefore, this thesis focuses on establishing new methods to address the issues of cell size and single cell protease measurement.

We first develop a size-based cell separation technique using Dean-coupled inertial microfluidic sorter. Separation of cells by size before downstream assays might be beneficial in simplifying the system and facilitating the discovery of rare subpopulations through enrichment of cells with certain size range or cell cycle phase. By investigating the particle focusing and separation mechanisms in curved microfluidic channel, we develop a novel design of inertial microfluidic sorter with higher separation resolution and then demonstrate its capacity in leukocyte isolation from blood. This novel cell sorter would be a promising alternative to many other cell separation problems.

We then establish a microfluidic platform for functional measurement of single cell pericellular proteases, including both those secreted and expressed on cell surface. We apply the platform to studying the PMA-mediated protease response of HepG2 cells at single-cell level and reveal the diversity in the dynamic patterns of single-cell protease activity profile upon drug stimulation. We also present the preliminary exploration of single-cell protease activity behavior in anti-cancer drug resistance development.

Lastly, we explore the applicability of our platform for single-cell shedding measurement. Protease-mediated molecular shedding is one of the key mechanisms through which individual cells actively regulate their own microenvironment. However, the amount of molecules being shed for individual cells is extremely low, posing significant challenges in detecting shedding quantitatively. By means of analytical analysis and numerical simulations, we investigate the intrinsic noise of low-abundance molecule detection. Experimental characterizations have also been performed to evaluate the impact of practical factors on actual readout variation.

Thesis Supervisor: Jongyoon Han
Title: Professor of Electrical Engineering and Computer Science, and Biological Engineering

Acknowledgements

The past years at MIT has been an incredible and enriching learning experience during which I meet amazing people.

Foremost, I would like to express my heartfelt gratitude to my research advisor, Prof. Jongyoon Han, who introduced me into the amazing field of BioMEMS and guided me with his insightful thoughts. I have greatly benefited from his passion and vision for science in addition to his generous support and encouragements throughout my doctoral studies. With his kind advice and help, I have been very fortunate to have the freedom to explore various research problems and try out new ideas, even though many of them did not work out well. I could not have imaged for a better advisor.

My committee members, Prof. Douglas A. Lauffenburger and Prof. Darrell J. Irvine, have also been a great source of advice and knowledge. I would like to thank them for reviewing my progress and keeping me on my toes. I do very much appreciate their time, encouragement and enlightening input. It is my great honor to have them on my thesis committee.

This work is done in collaborations with many others. Dr. Guofeng Guan, Dr. Ali Asgar. S. Bhagat in Singapore and Dr. Han Wei Hou here at MIT have been closely involved during the development of size-based cell sorter. Ms. Allison M. Claas in Lauffenburger Lab has been very helpful when it comes to cell culture and the conventional assays at bulk level. I am grateful for their efforts and critical inputs in shaping the projects. I must also acknowledge the funding sources of my doctoral studies, including Singapore-MIT Alliance for Research and Technology (SMART), DARPA Dialysis-Like Therapeutics (DLT) program and NIH grant R01-CA096504.

My sincere thanks also go to all the Han group members who have been very supportive and a joy to work with. I am indebted to Yong-Ak Song for setting me on my feet as a new graduate student, and to Aniruddh Sarkar for the helpful discussions and brilliant suggestions over the past years. It is also a great pleasure to work and spend time with other group members (listed in no particular order), including Sunghee Ko, Taehong Kwon, Wei Ouyang, Sha Huang, Chia-Chen Yu, Siwon Choi, Bumjoo Kim, Lih-Feng Cheow, Leoni Li, Rhokyun Kwak, Chia-Hung Chen, Hiong Yap Gan, and Sung Jae Kim.

I thank members of the RLE 8th floor community, especially the members of Voldman and Yanik labs, for sharing the lab facilities and tips of their use. I would like to acknowledge staff members at MIT Microsystems Technology Laboratories for their help in microfabrication. I would also like to express my appreciation for the camaraderie provided by my old friends from my undergraduate college, USTC, and the new friends I found at MIT including my classmates of BE'10 and many others. My time at MIT was made enjoyable with many cherished moments in large part due to those many friends.

Last but not least, I am deeply indebted to my parents, Chengming Wu and Ying Li, for their unconditioned love and support, as I have ventured beyond my home country to another side of the earth. Their love of science and way of critical thinking has been the seed of my pursuit in scientific research. I would like to dedicate this thesis to them to express my utmost love and gratitude.

This doctoral thesis has been examined by a Committee of the Department of Biological Engineering as follows:

Professor Douglas A. Lauffenburger .....

Chairman, Thesis Committee

Professor of Biological Engineering, Chemical Engineering and Biology

Professor Jongyoon Han .....

Thesis Supervisor

Professor of Electrical Engineering & Computer Science, and Biological Engineering

Professor Darrell J. Irvine .....

Member, Thesis Committee

Professor of Materials Science & Engineering, and Biological Engineering

Table of Contents

List of Figures

List of Tables

List of Abbreviations

ADAM	A Disintegrin and Metalloproteinase
AI	Activity index
c-Met	Hepatocyte growth factor receptor
CV	Coefficient of variation
CTC	Circulating tumor cell
DMSO	Dimethyl sulfoxide
EGFR	Epidermal growth factor receptor
ERK	Extracellular signal-regulated kinase
FRET	Fluorescence resonance energy transfer
MET	Hepatocyte growth factor receptor
MMP	Matrix metalloproteinase
MNL	Mononuclear leukocyte
NAI	Normalized activity index
SAPE	Streptavidin-conjugated phycoerythrin
PDMS	Polydimethysiloxane
PMMA	Poly(methy methacrylate)
PFF	Pinched-flow fractionation
PKC	Protein kinase C
PMA	Phorbol 12-myristate 13-acetate
PMN	Polymorphonuclear leukocyte
TIMP	Tissue inhibitor of metalloproteinase
TKI	Tyrosine kinase inhibitor
TNF-α	Tumor necrosis factor alpha
WBC	White blood cell

Chapter 1 Introduction

This thesis describes the development of two microfluidic techniques that facilitate single-cell study and also discusses the theoretical limits of antibody-based single-cell secretory molecule detection. This chapter first gives an introduction of cellular heterogeneity and the motivation for single-cell study. Secondly, we point out the challenges and requirements in single-cell measurements, and discuss the unique advantages of microfluidic technologies. Lastly, we outline the scope of this thesis and how it would facilitate single-cell study.

1.1 Cellular Heterogeneity: A Hidden World Behind Population Averages

1.1.1 Characteristics of Cellular Heterogeneity

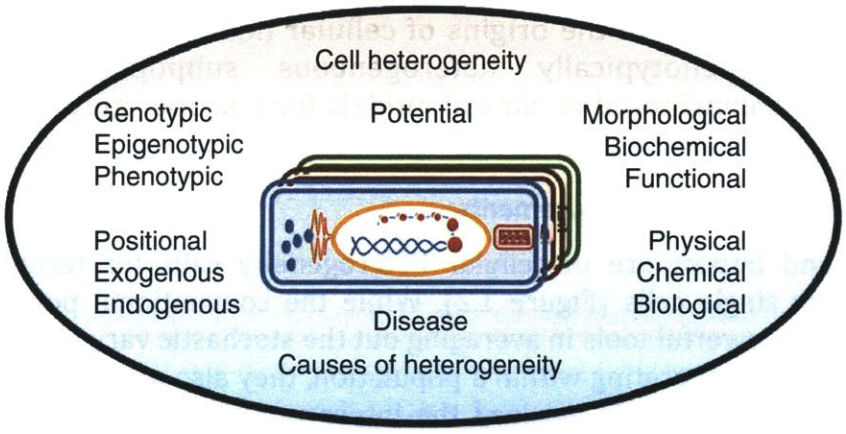

Figure 1.1 Cell-to-cell heterogeneity has many different manifestations and causes. Potential heterogeneity represents the cell's capability to change its function, chemical composition and structure. The figure and caption are adapted from [1].

With decades of efforts in measuring and analyzing cellular properties at single-cell level, people are now convinced that cellular heterogeneity is a ubiquitous feature of various biological systems, ranging from a complex tissue of a multicellular organism to the isogenic colony derived from a single mammalian cell or a bacterium *in vitro*. Furthermore, as an inevitable outcome of the variability in cellular response, the cell-to-cell heterogeneity in a given system can have many causes and manifestations in nearly the full spectrum of cellular properties (Figure 1.1). In general, cell-to-cell variability could be divided into two categories, the stochastic and the deterministic variability, based on its origins and functional outcomes. The stochastic cell-to-cell variability arises from the probabilistic and discrete nature of biochemical reactions. Along with the exquisite architecture of intracellular signaling network, the stochastic variability in cellular properties could enhance the capability of cells to maintain a state against small fluctuations [2] and thus is a desirable feature of cells. Meanwhile, many cellular properties present in a prior time point have been shown to influence the cell fate decision of individual cells in response to subsequent internal and external stimuli [3]. This

phenomenon reveals deterministic effects of cell-to-cell variability. Factors frequently used to explain cell-to-cell variability include molecular marker (indicating the presence of subpopulation with distinct phenotypes), cell size, cell cycle phase, spatial cell population context and cell history.

1.1.2 Implications of Cellular Heterogeneity

Whatever the category, cell-to-cell variability has significant implications in many biological processes. The most famous example can be found in the cases of leukemia and solid tumors, where rare subpopulations, termed as "cancer stem cells", with different proliferative and differentiative capacities from the bulk cancer cells have been identified and shown to play an important role in tumorigenesis and response to cancer therapy [4-7]. Moreover, recent studies of genetically homogenous populations revealed that non-genetic variability, such as fluctuations of intracellular biochemical reaction and subtle differences in the local microenvironment, could lead to significantly diverse responsiveness to drugs and stimuli [8-12]. Regardless of the origins of cellular heterogeneity, it's clear that the functionally or phenotypically heterogeneous subpopulations should be acknowledged and considered in clinical models for a proper guide to diagnosis and treatment of the disease [13, 14].

1.1.3 Necessity of Single-Cell Measurements

The presence and importance of cellular heterogeneity calls for technologies making measurements on single cells (Figure 1.2). While the conventional population-averaged measurements are powerful tools in averaging out the stochastic variability to highlight the dominant mechanisms operating within a population, they also mask the behavior of small subpopulations, or, even worse, mislead the interpretation of experimental results. The latter case can occur when several phenotypically distinct subpopulations are present in the same population at comparable quantities. A typical example can be found in the case of hormone-induced maturation of *Xenopus* oocytes [15], where a graded input is correlated with a graded output based on population-averaged measurements. An intuitive interpretation of the result would predict an intermediate output signal for an "average" oocyte upon the treatment of intermediate input. However, individual oocytes actually exhibit all-or-none characteristics in their response. Similarly, the ensemble averages would also fail to capture the dynamics of cellular response when the actual response is asynchronous or out-of-phase at single-cell level (Figure 1.2b). In fact, numerous key signaling and transcriptional processes show pulsatile, or even oscillatory, behaviors [16], emphasizing the necessity in measuring and analyzing single cells. Moreover, analysis of single cells is the first step to understand cell-cell interactions in populations. It can help separate cell-specific response (limited to individual cells) from those population-specific responses (involving cell-cell communication) and provide unique insights in the functioning of an entire system.

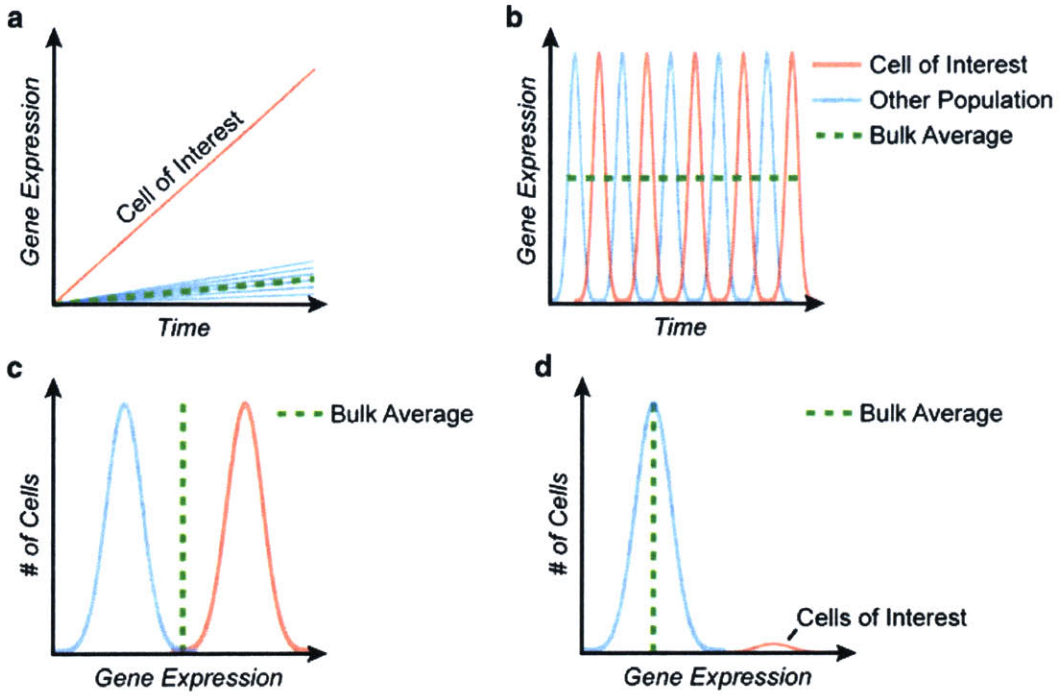

Figure 1.2 Ensemble average and heterogeneity, with gene expression as an example. (**a**) Population-averaged measurements mask amplitude differences between cells of interest and the majority population and (**b**) out-of-phase dynamics. (**c**) Subpopulation in multimodal distributions and (**d**) rare cell populations are not accurately represented by ensemble end-point assays. The figure and caption are adapted from [17].

1.2 Measuring Cell-To-Cell Variability: An Emerging Role for Microfluidic Technologies

Science and technology are the two pedals of the same wheel, as scientific knowledge allows the development of new technology, which in turn becomes the driving force of new scientific discoveries. A lot of progress has been achieved in single-cell measurements since the importance of cellular heterogeneity was first recognized in biological study. Whereas, the demands will only increase for methods to read out cellular properties at single-cell resolution, given the fact that cell-to-cell variability is increasingly applied to many biological and clinical questions.

1.2.1 Technical Challenges for Single-Cell Measurements

To enable meaningful single-cell study, technical advances should be achieved in several fronts: sensitivity, time resolution, throughput, and multiplexing capacity. Firstly, a single cell contains limited amount of material that exists with a very large dynamic range in abundances, for an astronomical large number of different species in molecule identities. It requires molecular analysis methods to have very high detection sensitivity to accurately probe on a particular molecule or at an "-omics" scale. Secondly, the dynamic range of time scale is also very large for molecular events involved in cell fate decision process. Considering a typical downstream signaling process of cell surface receptor ligation as an example, early responses like calcium flux could happen within several seconds to minutes.

And the subsequent intracellular signaling processes including the kinase reaction cascade and transcriptional changes might take minutes to hours to occur. Whereas, phenotypic difference determining the cell fate could be observed in a timescale of hours or days, as changes in molecules abundances and activities accumulate in response to the propagating signaling flux. Methods with suitable time resolution and wide operational range in acquiring single-cell dynamics of molecular events are therefore in demand. Thirdly, considerable throughput is necessary to extracting meaningful information based on single-cell measurements. Because the critical behaviors of minority cell subpopulations still needs to be measured with statistical significance, requiring sufficient number of measurements for (often rare) subpopulation cells. While one can achieve this goal by simply increasing the total number of single cells measured and monitored, it is often necessary to enrich those minority subpopulations of interest. In such cases, cell separation or enrichment technology also needs to be capable of processing large number of cells efficiently, in order to address problems involving rare cells. Finally, a crucial question of any single-cell study is whether the observed cell-to-cell variability has any biological function or practical impact. The key to this question is to create a mechanistic link between many different parameters of the cell fate decision process of the same cell. Therefore, it's highly desirable to have the capacity in analyzing single cells in multiplexed fashion, not only in terms of the "-omics" measurement for fully characterization of cellular components within system, but also with respect to putting the single-cell readouts in the context of extracellular microenvironment and the corresponding phenotypic outcomes.

1.2.2 Microfluidics for Single-Cell Measurements

There are many technical advances on all of these critical aspects of single-cell measurements and multiple reviews are available for analyzing single cells at almost the full spectrum of cellular state [18, 19], ranging from nucleic acid levels [20], epigenetics status [21], to proteomics [22] and metabolomics [23] characteristics. Particularly, various microfluidic systems have emerged as powerful tools expanding upon and beyond the existing capabilities of convention tools for single-cell analysis.

On one hand, there is a trend in miniaturizing the conventional analysis methods, such as the nucleic acid sequencing [24] and antibody-based molecular detection [25]. The miniaturized systems allow the compartmentalization and precise manipulation of small volumes of liquid, making it ideal for single-cell isolation and the downstream processes. Furthermore, microfluidic devices offer higher throughput, improved accuracy and the capacity in detecting multiple target molecules simultaneously, owing to its power in integrating multiple processing modules and the ability for parallelization and automation.

On the other hand, microfluidic technologies enable single-cell studies that are otherwise impossible. Firstly, taking advantage of many unique physical phenomenon – such as the cell trapping/separation using hydrodynamic [26], dielectric [27] or acoustic [28] forces – in microscale system, microfluidics enable precise manipulation of many single cells. Precise positioning of cells in space would not only provide the spatial registration of individual cells for long-term study on cellular response and history [29], but also enable the pairing between two different cells for cell-cell interaction study [26]. Moreover, when using as a sample preparation step, microfluidic technologies enabling positioning cells in flow can fractionate cell sample to enrich cells within certain size range or expressing

certain surface marker. In fact, sample preparation is highly recommended for single-cell analysis and often a necessary step when populations of interest are rare cells in complex tissues, like blood. Such examples include single-cell studies on circulating tumor cells, hematopoietic stem cells, and antigen specific T cells, whose abundance ranges from several to thousands among the billions of non-target cells in one millimeter of blood. Secondly, microfluidics has a tight control on the microenvironment of individual cells. Due to its comparable length scale in respect to the size of single cells (~10 μm), microfluidics provides a compatible interface for mimicking the physiological *in vivo* environments around the cells, in terms of the chemical cues like the gradients of diffusive and immobilized molecules, and the mechanical cues provided by interstitial flow or extracellular matrix. Moreover, one can introduce spatio-temporally precise perturbation of extracellular molecules [30] and shear stress [31] in microfluidic systems by exploiting the laminar flow feature of fluid at microscale. All these manipulations on single cells and their environment would greatly simplify the interpretation of cell behavior and therefore are beneficial for many single cell studies.

1.3 Thesis Scope and Outlines

Any single-cell study is usually composed of three phases: sample preparation, single-cell measurement, and data interpretation. In the sample preparation phase, various cell-sorting techniques are frequently used to isolate or enrich the population of interest from complex sample. And for a hypothesis-driven study, cells are often arranged in desirable fashion using cell-manipulation techniques to investigate the impact of particular factors on cellular response. In the single-cell measurement phase, various molecular analytes/events or other phenotypic parameters are measured and registered to individual cells for downstream mechanistic investigation. In the data interpretation phase, data analysis should be performed on the readouts with consideration on limits in experimental design and implementation. Despite the blossoming of tools and methodologies for single-cell study, certain unfulfilled needs remain in each phase. This thesis seeks to contribute to the field by providing tool facilitating sample preparation, platform enabling activity measurement of cellular microenvironment, and critical analysis on the limits of antibody-based analyte quantification for single-cell proteomic study.

We begin with the development of high-throughput size-based cell separation technique in Chapter 2. Various cell separation techniques have been developed for sample preparation of downstream assays. With a long history in sample preparation, affinity-based cell sorting has been employed in both bulk and microfluidic platforms – in forms of fluorescence activated cell sorting (FACS), magnetic activated cell sorting (MACS) and affinity-mediated cell capture/trapping. However, these methods rely closely on affinity labeling, whose performance depends on the quality of capture reagents and the presence of corresponding binding targets on cells. Besides, the labeling process, i.e. molecule binding to cell surface, could potentially alter the state of the target cells and thus not ideal for downstream studies involving functional characterization. Alternatively, several intrinsic biophysical properties, such as cell size, density, electrical properties and deformability, have also been exploited for cell sorting and even single-cell measurements of cellular physical attributes in a label-free manner. But the throughput, separation resolution and artificial impact on

cell state remain problematic, especially when dealing with sensitive blood cells. In Chapter 2, we introduce a novel size-based cell separation technique to address those issues.

While many previous single-cell studies primarily focus on the intracellular signaling events, the role of extracellular signaling in the regulation of cellular response is relatively unexplored in the field of single-cell study. Given the increasingly recognition of pericellular protease in extracellular signaling network, in Chapter 3, we develop a microfluidic platform for single-cell measurement of pericellular protease and investigate in both the amplitude and dynamic behavior of single-cell pericellular protease. Moreover, since protease-mediated molecular shedding is one of the key mechanisms through which individual cell actively regulates its own microenvironment, we further explore the applicability of our platform for single-cell shedding measurement. Chapter 4 hence presents a critical analysis on the theoretical limits of low-abundance molecule detection using antibody. A summary of this thesis and directions for future work would then be listed in Chapter 5.

1.4 References

[1] Rubakhin, S.S., Romanova, E.V., Nemes, P., and Sweedler, J.V., *Profiling metabolites and peptides in single cells.* Nat Meth, 2011. **8**(4s): p. S20-S29.

[2] Süel, G.M., Garcia-Ojalvo, J., Liberman, L.M., and Elowitz, M.B., *An excitable gene regulatory circuit induces transient cellular differentiation.* Nature, 2006. **440**(7083): p. 545-550.

[3] Snijder, B. and Pelkmans, L., *Origins of regulated cell-to-cell variability.* Nat Rev Mol Cell Biol, 2011. **12**(2): p. 119-125.

[4] Bonnet, D. and Dick, J.E., *Human acute myeloid leukemia is organized as a hierarchy that originates from a primitive hematopoietic cell.* Nat Med, 1997. **3**(7): p. 730-737.

[5] Singh, S.K., et al., *Identification of a Cancer Stem Cell in Human Brain Tumors.* Cancer Research, 2003. **63**(18): p. 5821-5828.

[6] O/'Brien, C.A., Pollett, A., Gallinger, S., and Dick, J.E., *A human colon cancer cell capable of initiating tumour growth in immunodeficient mice.* Nature, 2007. **445**(7123): p. 106-110.

[7] Boiko, A.D., et al., *Human melanoma-initiating cells express neural crest nerve growth factor receptor CD271.* Nature, 2010. **466**(7302): p. 133-137.

[8] Albeck, J.G., et al., *Quantitative Analysis of Pathways Controlling Extrinsic Apoptosis in Single Cells.* Molecular Cell, 2008. **30**(1): p. 11-25.

[9] Gascoigne, K.E. and Taylor, S.S., *Cancer Cells Display Profound Intra- and Interline Variation following Prolonged Exposure to Antimitotic Drugs.* Cancer Cell, 2008. **14**(2): p. 111-122.

[10] Spencer, S.L., Gaudet, S., Albeck, J.G., Burke, J.M., and Sorger, P.K., *Non-genetic origins of cell-to-cell variability in TRAIL-induced apoptosis.* Nature, 2009. **459**(7245): p. 428-432.

[11] Orth, J.D., et al., *Quantitative live imaging of cancer and normal cells treated with Kinesin-5 inhibitors indicates significant differences in phenotypic responses and cell fate.* Molecular Cancer Therapeutics, 2008. **7**(11): p. 3480-3489.

[12] Feinerman, O., Veiga, J., Dorfman, J.R., Germain, R.N., and Altan-Bonnet, G., *Variability and robustness in T cell activation from regulated heterogeneity in protein levels.* Science, 2008. **321**(5892): p. 1081-1084.

[13] Merlo, L.M.F., Pepper, J.W., Reid, B.J., and Maley, C.C., *Cancer as an evolutionary and ecological process.* Nat Rev Cancer, 2006. **6**(12): p. 924-935.
[14] Niepel, M., Spencer, S.L., and Sorger, P.K., *Non-genetic cell-to-cell variability and the consequences for pharmacology.* Current Opinion in Chemical Biology, 2009. **13**(5–6): p. 556-561.
[15] Ferrell, J.E. and Machleder, E.M., *The Biochemical Basis of an All-or-None Cell Fate Switch in Xenopus Oocytes.* Science, 1998. **280**(5365): p. 895-898.
[16] Spiller, D.G., Wood, C.D., Rand, D.A., and White, M.R.H., *Measurement of single-cell dynamics.* Nature, 2010. **465**(7299): p. 736-745.
[17] Di Carlo, D., Tse, H., and Gossett, D., *Introduction: Why Analyze Single Cells?*, in *Single-Cell Analysis*, S. Lindström and H. Andersson-Svahn, Editors. 2012, Humana Press. p. 1-10.
[18] Galler, K., Brautigam, K., Gro, Popp, J., and Neugebauer, U., *Making a big thing of a small cell - recent advances in single cell analysis.* Analyst, 2014. **139**(6): p. 1237-1273.
[19] Wang, D. and Bodovitz, S., *Single cell analysis: the new frontier in 'omics'.* Trends in Biotechnology, 2010. **28**(6): p. 281-290.
[20] Kalisky, T., Blainey, P., and Quake, S.R., *Genomic Analysis at the Single-Cell Level.* Annual Review of Genetics, 2011. **45**(1): p. 431-445.
[21] Schwartzman, O. and Tanay, A., *Single-cell epigenomics: techniques and emerging applications.* Nat Rev Genet, 2015. **advance online publication**.
[22] Yu, J., et al., *Microfluidics-Based Single-Cell Functional Proteomics for Fundamental and Applied Biomedical Applications.* Annual Review of Analytical Chemistry, 2014. **7**(1): p. 275-295.
[23] Zenobi, R., *Single-Cell Metabolomics: Analytical and Biological Perspectives.* Science, 2013. **342**(6163).
[24] Streets, A.M., et al., *Microfluidic single-cell whole-transcriptome sequencing.* Proceedings of the National Academy of Sciences, 2014. **111**(19): p. 7048-7053.
[25] Ma, C., et al., *A clinical microchip for evaluation of single immune cells reveals high functional heterogeneity in phenotypically similar T cells.* Nat Med, 2011. **17**(6): p. 738-743.
[26] Skelley, A.M., Kirak, O., Suh, H., Jaenisch, R., and Voldman, J., *Microfluidic control of cell pairing and fusion.* Nat Meth, 2009. **6**(2): p. 147-152.
[27] Wang, X.-B., et al., *Cell Separation by Dielectrophoretic Field-flow-fractionation.* Analytical chemistry, 2000. **72**(4): p. 832-839.
[28] Evander, M., et al., *Noninvasive Acoustic Cell Trapping in a Microfluidic Perfusion System for Online Bioassays.* Analytical Chemistry, 2007. **79**(7): p. 2984-2991.
[29] Rowat, A.C., Bird, J.C., Agresti, J.J., Rando, O.J., and Weitz, D.A., *Tracking lineages of single cells in lines using a microfluidic device.* Proceedings of the National Academy of Sciences, 2009. **106**(43): p. 18149-18154.
[30] Dertinger, S.K.W., Chiu, D.T., Jeon, N.L., and Whitesides, G.M., *Generation of Gradients Having Complex Shapes Using Microfluidic Networks.* Analytical Chemistry, 2001. **73**(6): p. 1240-1246.
[31] Lu, H., et al., *Microfluidic Shear Devices for Quantitative Analysis of Cell Adhesion.* Analytical Chemistry, 2004. **76**(18): p. 5257-5264.

Chapter 2 Size-Based Cell Separation Using Spiral Microchannel

This section contains extracted text and results from previous publication by the thesis contributor:

- *"Separation of leukocytes from blood using spiral channel with trapezoid cross-section", Analytical Chemistry, 2012, 84(21): p. 9324-9331, authored by Lidan Wu, Guofeng Guan, Han Wei Hou, Ali Asgar. S. Bhagat and Jongyoon Han. Lidan Wu (thesis author) was the first author of this publication, where she designed and carried out the experiments. Guofeng Guan helped out in fabricating the PMMA master for spiral microchannels with trapezoidal cross-section. Jongyoon Han supervised the research. All authors listed have contributed in the data analysis and writing.*

Cell size, a fundamental attribute resulting from both cell growth and cell division, impacts the cellular design and function of individual cells [1], thus being recognized as an important parameter in single cell study. Cell size has been correlated to the functional state of individual cells via cell cycle phase, since various eukaryotic cells have been reported to undergo size-dependent cell cycle transition. It has been shown that many growth factors [2, 3] and anti-cancer drugs [4] work in a cell cycle-dependent manner through their action on cell-cycle dependent kinases, providing a possible explanation for the role of cell size in relevant study. Additional, cell size has also been linked to the functional capacity of individual cells. One such example could be found in the study of human mesenchymal stem cells [5], where smaller cells displayed a faster proliferation cycle and more primitive form in terms of clonogenic potential and multipotent differentiation capacity. Therefore, separation cell population based on size might serve to enrich rare subpopulation with distinct functionality. And this kind of cell separation is especially useful when populations of interest are minority cells in blood and other biological fluids.

Inertial microfluidics has recently drawn wide attention as an efficient, high-throughput microfluidic cell separation method. However, the achieved separation resolution and throughput, as well as the issues with cell dispersion due to cell- cell interaction, has appeared to be limiting factors in the application of the technique to real-world samples such as blood and other biological fluids. In this chapter, we present a novel design of spiral inertial microfluidic (trapezoidal cross section) sorter with enhanced separation resolution. As a proof-of-concept, we demonstrate its ability in isolating leukocytes from diluted human blood (1-2% hematocrit) with high efficiency (>80%). Polymorphonuclear leukocytes (PMNs) enriched by our method also showed negligible activation as compared to original input sample, while conventional RBC lysis method clearly induced artificial activation to the sensitive PMNs. Therefore, the developed technique would be a promising solution for many other size-based cell separation problems.

2.1 Introduction

2.1.1 Cell Separation Problem for Blood Sample

Red blood cells (RBCs) or erythrocytes are the most abundant cell component in many biological fluids, including blood (where it makes up ~45% of the volume), bone marrow aspirate and peritoneal aspirate. Depletion of contaminating RBCs from those samples is often an indispensable sample preparation step before the application of any scientific, clinical and diagnostic tests due to various reasons [6]. For example, inadvertent lysis of RBCs releases hemoglobin, leading to chemical interference and deteriorating the PCR-based test performances [7]. Reports supporting the anti-proliferative and pro-apoptotic role of RBCs in primary cell culture of human cells have also been published [8, 9]. While the required degree of RBC removal varies widely depending on the downstream applications, avoiding artificial alteration on the phenotypes of sorted cells is an important criterion for all studies. This is especially important in the case of removing RBCs from human blood to isolate white blood cells (WBCs) or leukocytes, which play a key role in carrying out and mediating the immune response to various pathogens. The information extracted from the isolated leukocytes would be meaningful to facilitate disease prognosis only when the key features of leukocytes' original state are not masked by the sample preparation artifacts.

2.1.2 Current Technologies for Blood Cell Separation

Conventional methodologies for blood cell separation on the macroscale include differential centrifugation and selective RBC lysis. While the performance of differential centrifugation is affected by the blood source, especially for blood from individuals with diseases, such as recurrent infections [10], the RBC lysis method, which is usually used in combination with the centrifugation to get complete RBC removal, exposes the cells to hypotonic environment, altering cell metabolism in a cell type-specific manner [11]. Besides, several cases have been reported that those sample preparation procedures could result in altered immuno-phenotype [12, 13] or impaired viability [14, 15] of the isolated WBCs. Moreover, the macroscale sample handling introduces variability to the separation and downstream application results due to imprecise control and non-uniform conditions, making the comparison of analogous results across different laboratories and platforms non trivial [16].

Several high-resolution, continuous microfluidic separation techniques [17-20] utilizing the size-dependent hydrodynamic effects have been reported to achieve the discrimination of few-micrometers particle size differences, which is comparable to the intrinsic difference in size observed among blood cells (RBCs: 6~8 μm discoid; mononuclear leukocytes (MNLs): 7~10 μm sphere; polymorphonuclear leukocytes (PMNs): 10~12 μm sphere; WBCs include both MNLs and PMNs) [21, 22]. These approaches are considered to be promising alternatives to bypass the issues associated with macroscale blood cell separation methods mentioned above and are able to process the sample in a label-free and continuous manner. Size-based microfluidic separation techniques do not require the addition of any lytic agent or prior cell labeling treatment and allow better control of the microenvironment during the blood sample handling. The cell separation is achieved by driving individual cells uniformly through a microchannel with well-designed geometry,

which leads to the alignment of cells in different positions across the channel width in a cell-size-dependent manner, followed by continuous sample collection at different outlets. The channel design is extremely critical for both the separation resolution and throughput, and differs as the working principle of the exact size-based hydrodynamic effects varies. In one example, "deterministic lateral displacement (DLD)", microchannel containing an array of microposts leads to differential lateral displacement for particles above or below the critical hydrodynamic diameter as a result of the asymmetric bifurcation of laminar flow around the microposts [19]. In another type of microfluidic device, "pinched-flow fractionation (PFF)", patterned with a contraction-expansion segment [20], the parabolic velocity profile of laminar flow within the contraction region leads to the alignment of particles near the channel sidewall in a size-based manner so that large particles with comparable diameter to the channel width of contraction region stay closer to the middle streamlines but smaller particles have their center closer to the channel sidewall. This difference in lateral positions of particles with varying size is further amplified upon entering the expansion region, resulting in efficient separation. Both techniques have the high resolution required for separating RBCs from other cell types but are severely limited in their practical application on clinical samples by the low working flow rates.

2.1.3 Our Approach for Blood Cell Separation Based on Size

To increase throughput, several groups have demonstrated the use of inertial lift forces and Dean forces in straight [23, 24] or spiral microchannels respectively [25-29] to precisely manipulate cell/particle positions within channel based on their size for high throughput separation(> 10^6 cells/min or ~1 mL/min flow rate). While spiral microchanel has also been previous applied for efficient affinity-based capture of endothelial cells, smooth muscle cells and fibroblasts on functionalized surfaces [30], the working flow rate and throughput (7.54 μL/min for 10^6 cells/mL input sample) is considered lower than that required for inertial focusing of cells in spiral channel, and thus not suitable for blood cell separation applications due to the large RBC background in blood samples. In this work, we further improve the separation resolution of spiral microchannel while maintaining the high-throughput feature by modifying the shape of channel cross-section to be trapezoidal instead of conventional rectangular, and demonstrate its ability for efficient RBC depletion from human blood sample with negligible effects on PMN immuno-phenotype. Moreover, to fit the needs of processing sample with volume ranging from microliter to milliliter scale, the current design can directly process the diluted whole blood sample when the blood sample volume is in the order of microliter, (e.g. fingerprick) and as a replacement for RBC lysis method, it can also be used in combination with differential centrifugation to get pure WBCs with no sign of alteration in activation status of the sorted cells for larger sample volume (~mL). We envision that the novel trapezoid cross-sectional spiral microchannel developed can be used as a generic, high-throughput method for removing RBCs and enriching target cells from other biological fluids, such as harvesting mesenchymal stem cells (MSCs) from bone marrow aspirates.

2.3 Materials and Methods

2.3.1 Microchannel Fabrication

The trapezoid cross-sectional spiral channels were made of polydimethylsiloxane polymer (PDMS, Sylard 184 Silicone Elastomer Kit, Dow Corning, USA) using standard soft lithography techniques from a poly(methyl methacrylate) (PMMA) master template. The PMMA template master was fabricated by a milling process (Whits Technologies, Singapore) to meet the special requirement in cross-sectional geometry. Given the available milling machine capability, the actual pattern of template mold has a tolerance of ± 10 μm compared to the virtual design and a surface roughness of R_a = 0.8 μm. Subsequently, PDMS prepolymer mixed with curing agent in a 10:1 (w/w) ratio was then cast on the PMMA template master and cured under 80°C for 2h to replicate the microchannel features. The cured PDMS molds were peeled off from the PMMA master and punched for the inlet and outlet reservoirs using 1.5 mm-diameter biopsy punch. Finally, the PDMS molds were irreversibly bonded to another flat 0.5 cm-thick PDMS sheet following oxygen plasma treatment (Harrick Plasma Cleaner/Sterilizer, Harrick Plasma, Inc., USA). The resulting PDMS devices were cut at four different locations and the cross-sections were measured under microscope to determine the exact dimensions of the devices.

The rectangular cross-sectional spiral channels were also fabricated in PDMS polymer but using a double molding process from a etched silicon wafer master [31]. Briefly, positive AZ4620 photoresist was first patterned on a 6-inch silicon wafer to define the microchannel features. Then, the patterned wafer was etched to desired depth using deep reactive ion etching (DRIE), followed by residual photoresist removal using oxygen plasma treatment. Next, trichloro(1H,1H,2H,2H-perfluorooctyl)silane (Sigma-Aldrich, USA) was coated on the etched wafer for 1.5 h to assist PDMS mold release. PDMS liquid mixture with 5 parts of prepolymer and 1 part of curing agent was then poured to the silicon wafer and cured under 80 °C for 2 h. The resulting PDMS mold has channel features obtruding from the surface and will served as a master for subsequent PDMS molding. The silane treatment and PDMS curing was repeated with this PDMS master to get negative replica. As a last step, the negative replica with inlet and outlet reservoirs punched was bonded to another PDMS substrate by standard plasma-assisted bonding.

2.3.2 Sample Preparation

For bead experiments, fluorescent polystyrene particles (1 wt. % solid content) with diameter of 6 μm (5.518 μm ± 0.122 μm), 10 μm (10.3 μm ± 0.4 μm) (Polysciences, Inc., USA), or 15.5 μm (15.5 μm ± 1.52 μm, Bangs Laboratories, Inc.) were diluted in deionized water (0.1% volume fraction) containing 0.025 mg/mL PEG-PPG-PEG Pluronic® F-108 (Sigma-Aldrich, USA), respectively, serving as the input sample. The small amount of PEG-PEG-PEG Pluronic® F-108 added was not enough to change the viscosity and density of fluid but rather minimized the non-specific adherence of particles to channel walls [32].

For experiments with blood sample, fresh human whole blood from healthy donors with sodium heparin as anti-coagulant was purchased from Research Blood Component, LLC (Boston, MA, USA) and processed within 6 h after collection to ensure viability of PMNs.

The PMNs and MNLs were isolated using Mono-Poly Resolving Media (MP-RM; MP Biomedicals, LLC, USA). Briefly, a 15mL centrifuge tube containing 3.5 mL of whole blood layer atop a 3 mL MP-RM layer was centrifuged under 300g for 30 min with brakes off. The bands of cells containing MNLs and PMNs were collected to separate tubes, washed and resuspended in sample buffer (1x PBS with 0.5% BSA), respectively. The isolated MNLs and PMNs could also be mixed together, serving as the representative WBC sample isolated via differential centrifugation. WBCs isolated using selective RBC lysis method were obtained by treating whole blood with RBC lysis buffer (eBioscience Inc., USA) (1:10) for 10 mins, followed by washing and resuspension in sample buffer. Finally, for blood samples, whole blood was spun down at 400g for 10min with brake off to obtain the cell and plasma fractions. The cell fraction was then resuspended in sample buffer and adjusted to varying hematocrits (0.5~2% hematocrit) to constitute the various samples.

2.3.3 Device Characterization

The device was mounted on an inverted phase contrast/epifluorescence microscope (Olympus IX71, Olympus Inc., USA) equipped with a 12-bit CCD camera (C4742-80-12AG, Hamamatsu Photonics K.K., Japan). Samples were loaded within a syringe and pumped through the microchannel at varying flow rates using a syringe pump (Harvard Apparatus PHD 2000, Harvard Apparatus Inc., USA). To prevent the particle/cell sedimentation, a small magnetic stir bar placed inside the syringe was agitated during sample processing. Using ImageJ ® software, the position of fluorescent particles within channel cross-section were determined by taking the average fluorescence intensity of the image series. For cells, high speed videos captured using a high-speed camera, Phantom v9.1 (Vision Research Inc., USA) under phase contrast were analyzed to determine the cell positions. The standard deviation of light intensity of the high-speed video was calculated to visualize the positions of fast moving cells.

2.3.4 Flow Cytometry Analysis

All antibodies were purchased from BD Pharmingen™ (BD Biosciences, USA). To determine the separation efficiency, whole blood was stained with 0.1 mg/ml Hoechst 33342 (Invitrogen, USA) and FITC-conjugated mouse anti-human CD66b monoclonal antibody (1:25 v/v) for 30 min at 4°C in the dark. The stained blood cell fraction was then collected by centrifugation and resuspended in sample buffer to desired hematocrit as input sample. Both input sample and output samples from two outlets were collected and analyzed on BD™ LSR II flow cytometer (BD Biosciences, USA) to determine the WBCs (Hoechst-positive cells) and PMNs (CD66b-positive cells) in each sample. Given the fact that MNLs comprise various cell types and there are no convenient surface markers available to determine the total amount of MNLs, the MNL count was based on the number of Hoechst-positive but CD66b-negative cells. Additionally, the RBC concentration was further measured by Z2 coulter counter (Beckman Coulter Inc, USA). Similarly, to evaluate the device performance on buffy coat sample, WBCs isolated by centrifugation with MP-RM were stained for surface marker, CD66b, and nucleus. The stained WBCs were then resuspended in sample buffer with same volume of the initial whole blood volume and processed by the device. Next, the size distribution of cells in the sample was measured by Z2 coulter counter and flow cytometer was used to analyze the sample composition.

For comparison between different RBC removal techniques, whole blood (without staining) was diluted to 1% hematocrit in sample buffer and then processed by the microchannel device. Subsequently, input and output samples of device, as well as the WBCs isolated by differential centrifugation with MP-RM or by 10 min of hypotonic RBC lysis (methods described in the *sample preparation* section), were stained with FITC-conjugated mouse anti-human CD66b monoclonal antibody (1:25 v/v) and APC-conjugated mouse anti-human CD18 monoclonal antibody (1:25 v/v) for 30min at 4°C in the dark. After staining, the samples were washed with sample buffer and analyzed on flow cytometer. The gates for activated PMNs (i.e. CD18-positive PMNs), were drawn based on PMNs treated with 30 mins of 1 μM phorbol 12-myristate 13-acetate (PMA; Sigma-Aldrich, USA) under 37°C (complete activation achieved), followed with immunofluorescence staining and FACS analysis.

2.3.5 Nitro Blue Tetrazolium (NBT) Test

The WBCs isolated by differential centrifugation with MP-RM and the WBCs isolated by the spiral process with 1% hematocrit input sample were resuspended in sample buffer to a final concentration of ~1 million cells/mL. 40 uL of each cell sample was deposited onto Poly-L-lysine coated glass slide (Sigma-Aldrich, USA), respectively, where the region for sample has been circled using Hydrophobic Barrier Pen (ImmEdge™ Pen, Vector Laboratories, Inc., USA). Sample on the slide were then incubated at 37 °C for 10 min to allow the cell attachment. The assay buffer for NBT test was freshly prepared and consisted of 1x Ca^{2+}/Mg^{2+}-containing DPBS buffer (Dulbecco's Phosphatase Buffered Saline; Invitrogen, USA) and 0.25% (w/w) NBT (Sigma-Aldrich, USA). For the conditions with PMA stimulation, the assay buffer also contained 1 μM PMA. After incubation, 40 uL of assay buffer would be added onto the slide for 20-min incubation at 37 °C. Lastly, the cell sample was observed under phase contrast microscope (Olympus CKX41, Olympus Inc., USA) and color images would be taken by a DSLR camera (Canon EOS 500D, Canon, USA) with 60x objective under microscope using NDPL-1 (2x) connecting len (Vivitar® Sakar International, Inc., USA).

2.4 Design Principle of Dean-Coupled Inertial Microfluidic

When flowing through a microchannel, particles suspended in a fluid experienced inertial lift forces and viscous drag. Inertial lift forces include the shear-induced lift force resulting from the parabolic velocity profile of flows in a confined channel [25] and the wall-induced lift force arising from the disturbed rotational wake around the particles when close to the wall [33]. For particles satisfying $a_p/D_h \geq 0.07$ (where a_p represents particle diameter, and $D_h = \frac{4A}{P}$ is microchannel hydraulic diameter, A and P are the area and perimeter of channel cross-section respectively), the interplay between shear-induced and wall-induced lift forces leads to lateral migration of the initial randomly distributed particles to stable equilibrium positions around the microchannel periphery [25-27]. Many studies revealed that the net inertial lift force (F_L) acting on the particles is highly dependent on particle size ($F_L \propto a_p^4$) and fluid shear rate ($F_L \propto G^2$). Apart from these, the resulting equilibrium positions are also affected by the geometry of channel cross-section. Within a square cross-sectional straight microchannel, particles focus at 8 equilibrium positions in low Reynolds

number flows ($Re_c < 100$, where $Re_c = \frac{\rho U_f D_h}{\mu}$ and ρ, U_f, μ represents the density, velocity and viscosity of the fluid medium separately) but 4 equilibrium positions near channel corners when Reynolds number is high ($Re_c \geq 500$) [34]. Whereas, the asymmetric nature of shear rate in rectangular cross-sectional microchannel with high aspect ratio results in preferential focusing of particles along the longer channel dimension [35]. Incorporation of channel curvature could further modify the equilibrium positions by exerting viscous drag of secondary flow on particles. Fluid passing through a curved microchannel such as spiral channel is subjected to centrifugal acceleration generating a secondary flow composed of two counter-rotating vortices (Dean vortices) across the channel cross-section [36, 37]. The magnitude of the vortex flow can be expressed using the non-dimensional Dean number (De) and the viscous force, known as Dean drag force (F_D), experienced by the particles can be quantified by assuming Stokes drag.

$$De = \frac{\rho U_f D_h}{\mu}\sqrt{\frac{D_h}{2R}} = \mathrm{Re}_c\sqrt{\frac{D_h}{2R}} \tag{2.1}$$

$$F_D = 3\pi\mu U_D a_p = 5.4\times10^{-4}\pi\mu De^{1.63} a_p \tag{2.2}$$

where U_D represents the average velocity of Dean flow given by $U_D = 1.8 \times 10^{-4} De^{1.63}$ [37]. Notably, although it's not clearly indicated in the expression of Dean drag force, both its magnitude and direction varies within the channel cross-section since the secondary flow velocity differs at different location of Dean vortices and is almost zero at the vortex core [38]. While the inertial lift force primarily dictates the particle focusing, the combinatory effect of Dean drag force and inertial lift force within spiral channel reduces the multiple equilibrium positions of particles into two vertically overlapping positions with same lateral distance to the inner channel wall [39]. Furthermore, as a result of the size-dependence of both two forces ($F_L \propto a_p^4, F_D \propto a_p$), particles with varying diameters occupy distinct lateral positions near the inner channel wall and demonstrate different degree of focusing when flowing through same spiral channel under a given flow rate. Thus the spiral microchannel can be applied as a possible size-based particle/cell separation device.

One major challenge of utilizing spiral microchannel in blood cell separation lies in the limited separation resolution and capacity of holding vast number of RBCs without affecting the separation efficiency. One recent work showed that polystyrene particles with a diameter of 7.32 μm, 9.92 μm, 15.02 μm and 20.66 μm, respectively, could focus into four distinct bands in a spiral microchannel with 500 μm × 100 μm ($W \times H$) rectangular cross-section at $De = 16.3$, at a very low concentration (0.005% volume fraction particle solution) [40]. However, this design cannot be directly applied to blood sample where the vast number of RBCs significantly broaden the stream width of RBCs due to cell-cell interactions and affect the focusing of other cells. To accommodate the samples with higher hematocrit, we need to increase the spacing between equilibrium positions. Our approach is to modify the spiral microchannel cross-section into a trapezoid with higher channel depth on the outer channel wall (Figure 2.1). The asymmetry of trapezoid cross-section alters the shape of velocity field and results in formation of strong Dean vortex cores skewed towards the outer wall with larger channel depth even at relatively low flow rates.

Therefore, while in spiral with rectangular cross-section the interplay between inertial lift force and Dean drag force leads to the focusing of large particles close to the inner wall and the trapping of small particles at the core of Dean vortices located at the center of channel width, the modified velocity field of spiral with trapezoid cross-section leads to a greater shift for small particles towards the outer wall without affecting the focusing position of large particles, thus providing a greater difference in equilibrium positions between them, resulting in higher separation resolution (Figure 2.2).

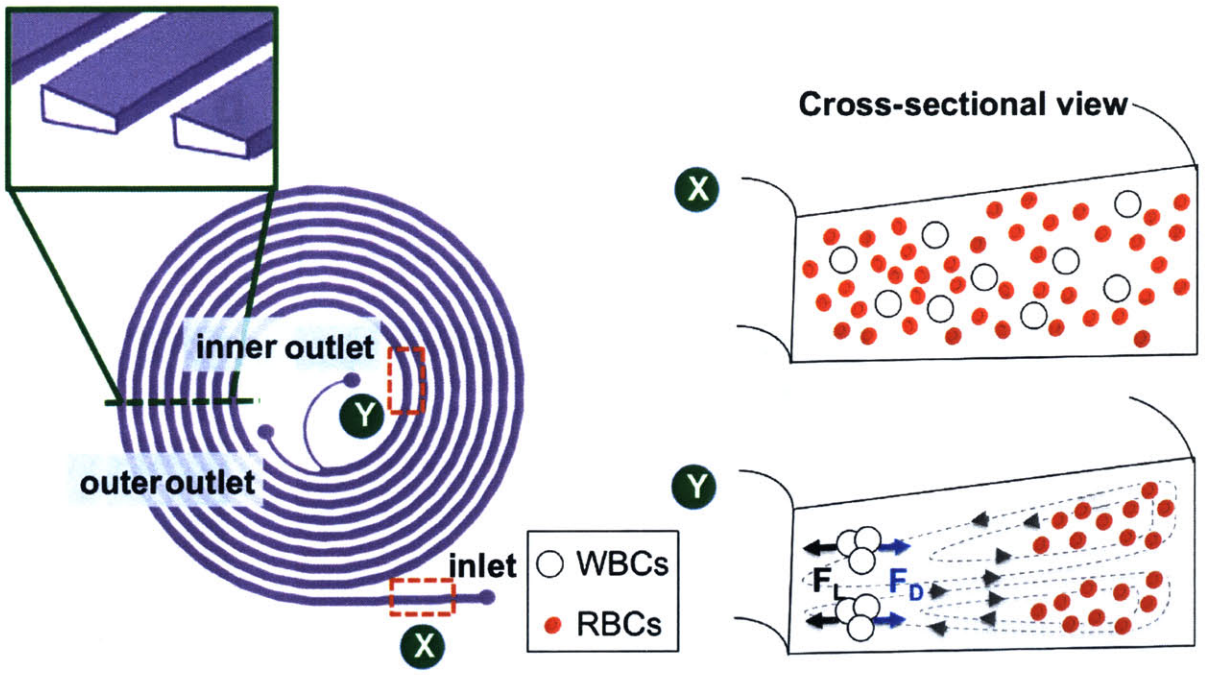

Figure 2.1 Schematic (not to scale) of spiral channel with trapezoid cross-section of 500 μm width, 70 μm (inner) and 100 μm (outer) depth illustrating the operation principle. At the outlet, the larger white blood cells (WBCs) focus near to the inner wall due to the combination of inertial lift force (F_L) and Dean drag force (F_D), while the smaller red blood cells (RBCs) are trapped at the core of dean vortex and form a broad band near the outer wall.

The trapezoid cross-section also has an impact on the size- and flow-rate-dependence of particle focusing. In a rectangular cross-sectional spiral, particles with $a_p/D_h \geq 0.07$ initially focus near the inner channel wall at low Re_c, and then move towards the outer wall as Re_c increases. When Re_c is sufficiently high, Dean drag force dominates the particle behavior leading to defocusing of particles. On the contrary, our results indicate that instead of D_h, the channel depth at inner wall (D_{inner}) serves as a better critical channel dimension to determine whether particles of certain diameter can form a focused stream near the inner wall. This was confirmed by using trapezoid channels satisfying $D_{outer}/D_{inner} \leq 1.5$ criterion (Figure 2.3). Interestingly, while the particle behavior of trapezoid cross-section spiral displays a similar focusing-defocusing dependence on Re_c, an additional regime featured by the trapping of particles within the outer half of channel cross-section was observed when Re_c increased further. Moreover, the flow rate required to trap particles increases with particle size, making the isolation of particles within a specific size range feasible. The exact mechanism of particle trapping under high Re_c

remains elusive. Previous research has revealed that the position of the focused particle stream is affected both by the direction and magnitude of F_D acting on particles significantly [41], while F_L was the primary force dictating particle focusing in low Re_c flow [39]. We therefore hypothesize that the altered velocity field within trapezoid cross-sectional spiral might lead to a skewed Dean vortex profile, acting as a particle trap at the core of the vortex. As a result, at low Re_c the large particles can escape the Dean vortex cores experiencing small F_D and be able to find their lateral equilibrium position primarily determined by spatial distribution of F_L. Further study on the inertial focusing of trapezoid cross-sectional spiral is necessary to validate this hypothesis.

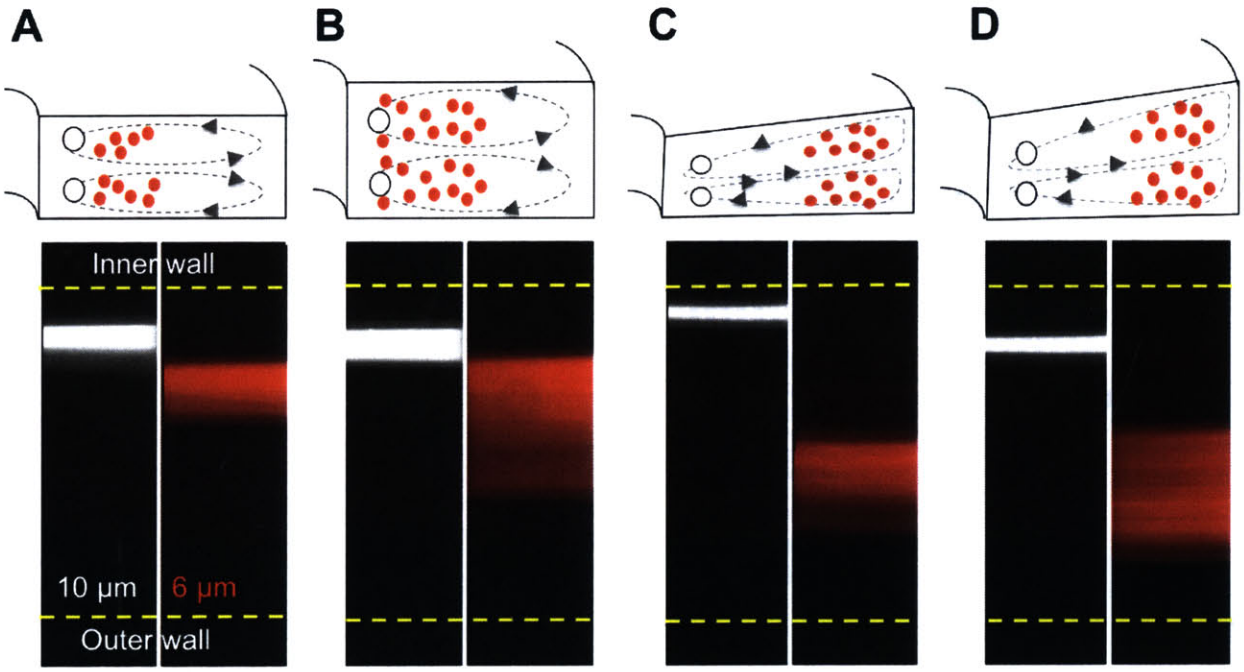

Figure 2.2 Schematic (not to scale) and average composite fluorescent images indicating the inertial focusing of 10 μm (white) and 6 μm (red) beads in (**A**) spiral channel with rectangular cross-section of 500 μm × 90 μm ($W \times H$) under optimal flow rate: 1 ml/min ($De = 4.31$); (**B**) spiral channel with rectangular cross-section of 500 μm × 120 μm under optimal flow rate: 2 ml/min ($De = 8.63$); (**C**) spiral channel with trapezoid cross-section of 500 μm width, 70 μm (inner) and 100 μm (outer) depth under optimal flow rate: 0.8 ml/min ($De = 4.22$); (**D**) spiral channel with trapezoid cross-section of 500 μm width, 90 μm (inner) and 120 μm (outer) depth under optimal flow rate: 0.8 ml/min ($De = 4.32$). Yellow lines indicate the positions of channel walls.

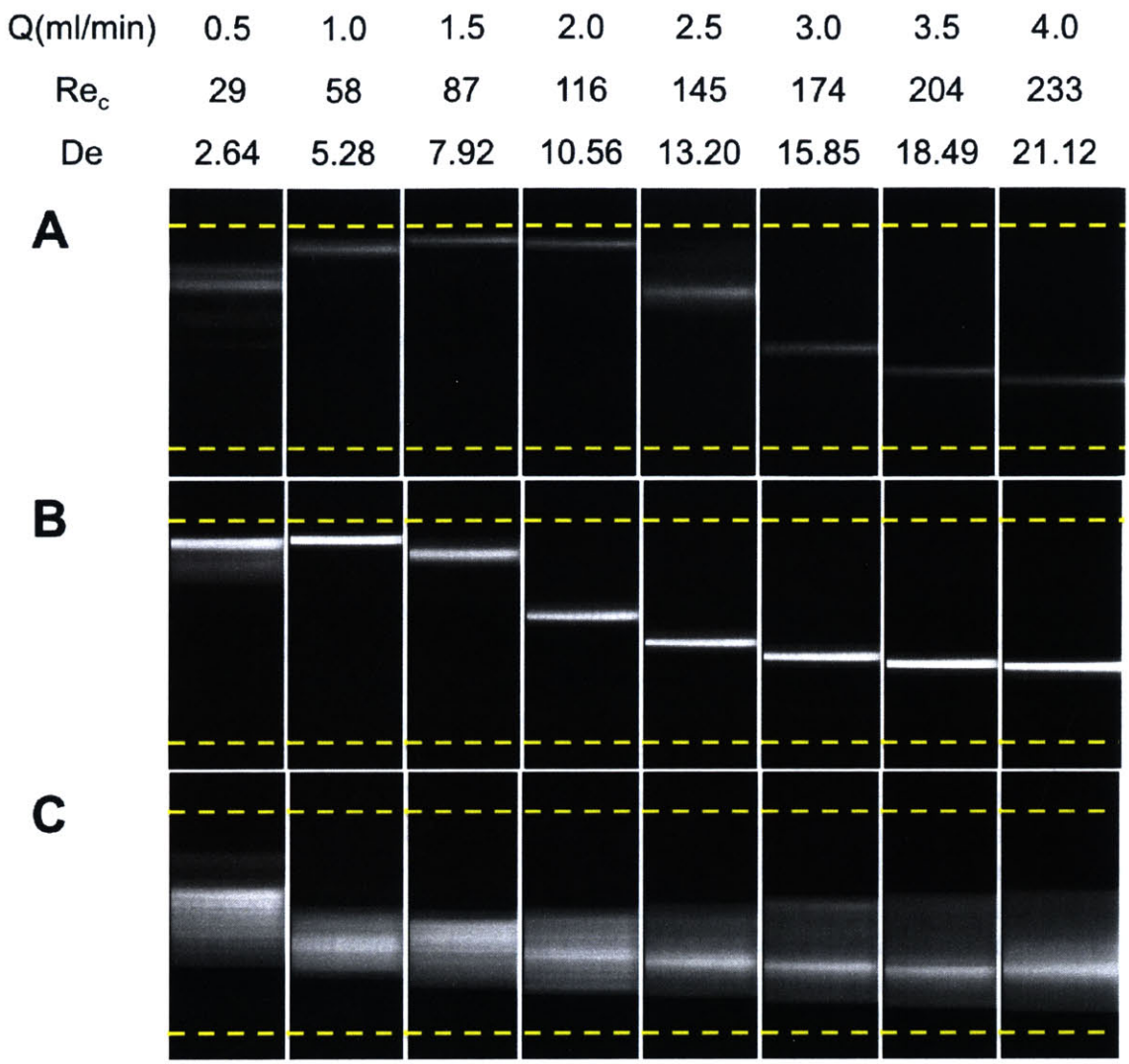

Figure 2.3 Top-down view images demonstrating the focusing behavior of fluorescent particles as a function of flow rate (Q) inside spiral channel with trapezoid cross-section of 500 μm width, 70 μm (inner) and 100 μm (outer) depth. (**A**) 15.5 μm particles, $a_p/D_h = 0.104$, $a_p/D_{inner} = 0.213$; (**B**) 10 μm particles, $a_p/D_h = 0.067$, $a_p/D_{inner} = 0.137$; (**C**) 6 μm particles, $a_p/D_h = 0.040$, $a_p/D_{inner} = 0.082$. Yellow lines indicate the position of channel walls, while the inner channel walls were shown on the top side of the images.

2.5 Separation of Leukocyte from Blood

2.5.1 Device Performance on Human Blood Sample

The optimized PDMS device for RBC removal developed consists of a 1-inlet, 2-outlet spiral microchannel with trapezoid cross-section of 500 μm width (485.00 μm ± 2.31 μm), 70 μm (inner wall, 72.84 μm ± 1.16 μm) and 100 μm (outer wall, 102.65 μm ± 3.55 μm) depth. Near the outlet region, the 485 μm wide channel was split into two outlet channels with a channel width ratio of 3 : 7 (inner : outer), while their channel lengths were adjusted to be equal with each other. We defined the inner outlet to be the WBC outlet with RBC-depleted sample (i.e. PMNs/MNLs) and the outer outlet to be the RBC waste outlet. The optimal flow

rate was experimentally determined to be 0.8 mL/min ($Re_c = 46.52; De = 4.22$). PMNs and MNLs isolated via centrifugation using MP-RM were injected through our device separately to determine their equilibrium positions inside the channel (Figure 2.5A). Under optimal flow rate, PMNs formed a focused stream at a distance of ~75 μm away from the inner channel wall in the top-down view, and MNLs occupied a similar lateral position but had a slightly wider stream width presumably due to the smaller cell size. On the contrary, RBCs with much smaller cell size displayed as a broad stream near the outer channel wall, enabling the isolation of PMNs/MNLs from RBCs at the device outlets. Compared to conventional rectangular cross-sectional spiral microchannel (Figure 2.4A), where the distribution of WBCs significantly overlaid with that of RBCs for input sample of ≥0.1% hematocrit, the developed trapezoid cross-sectional spiral achieved a larger spacing between WBCs and RBCs (Figure 2.4B), therefore allowing it to process input sample of higher hematocrit without compromising the purity and recovery of isolated WBCs. Figure 2.5B showed the recovery of blood components from WBC outlet of the developed device after a single pass and the optimal performance was achieved for 0.5% hematocrit blood sample with ~95% RBC removal and 98.4% of total WBC recovery (99.4% PMN recovery and 92.4% MNL recovery). Under this condition, the device's throughput translates to ~10 μL of whole blood (45% hematocrit) per min which is significantly higher than other microfluidic leukocyte isolation devices, such as "hydrodynamic filtration" with ~29 fold WBC enrichment at 20 μL/min for 10-fold diluted blood [42], dielectrophoretic (DEP) microseparator with 92% WBC recovery at 50 μL/hr [43], and magnetophoretic microsparator with 97% WBC recovery at 2.5~20 μL/hr [44]. Further increase in input sample hematocrit would broaden the distribution of RBCs across channel width, leading to a decrease in both RBC removal but the total WBC recovery and PMN recovery remained relatively constant. Up to 1.5% hematocrit, the device can still achieve 86.8% RBC removal and 96.2% of total WBC recovery. A 2-stage process, where the output sample from WBC outlet of the 1st run was used as the input of 2nd run without any dilution, can be fashioned to achieve high RBC removal while maintaining good WBC recovery for 1%~1.5% hematocrit sample (Figure 2.5C, D). Since WBCs collected from the 1st stage were concentrated by a factor of ~6, one can easily process 500 μL of whole blood with the 2-stage process for less than 25 min, which is comparable to the microfluidic RBC lysis device reported by Sethu *et al.* [45].

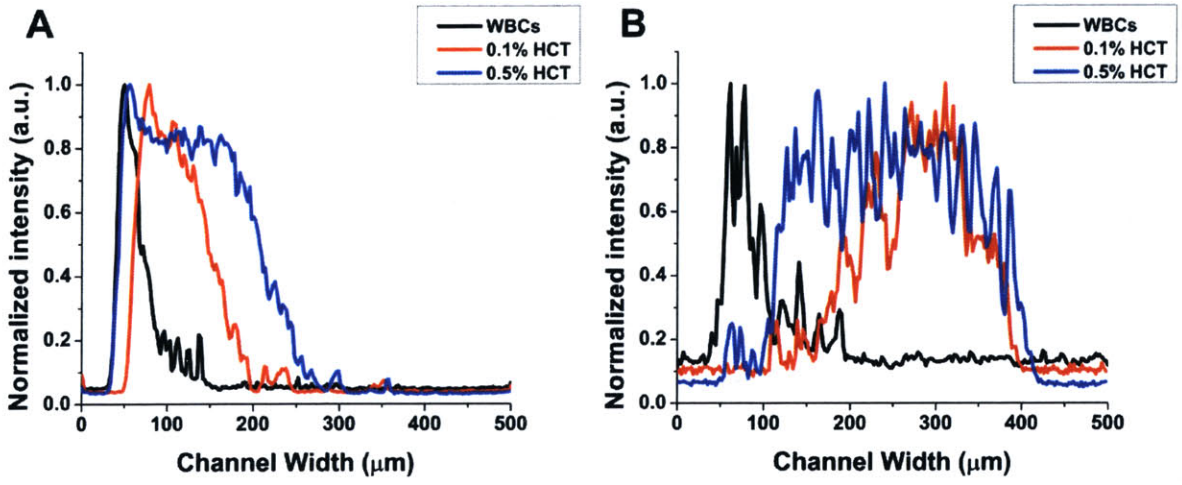

Figure 2.4 Normalized intensity line scans indicating the distribution of WBCs and RBCs at different hematocrit (0.1%, 0.5%) across channel width of (**A**) spiral channel with rectangular cross-section ($500\ \mu m \times 90\ \mu m$) under optimal flow rate (1 ml/min), or (**B**) spiral channel with trapezoid cross-section ($500\ \mu m \times 70/100\ \mu m$) under optimal flow rate (0.8 ml/min). The inner channel wall is represented by x = 0, and the outer channel wall is represented by x = 500. HCT: hematocrit.

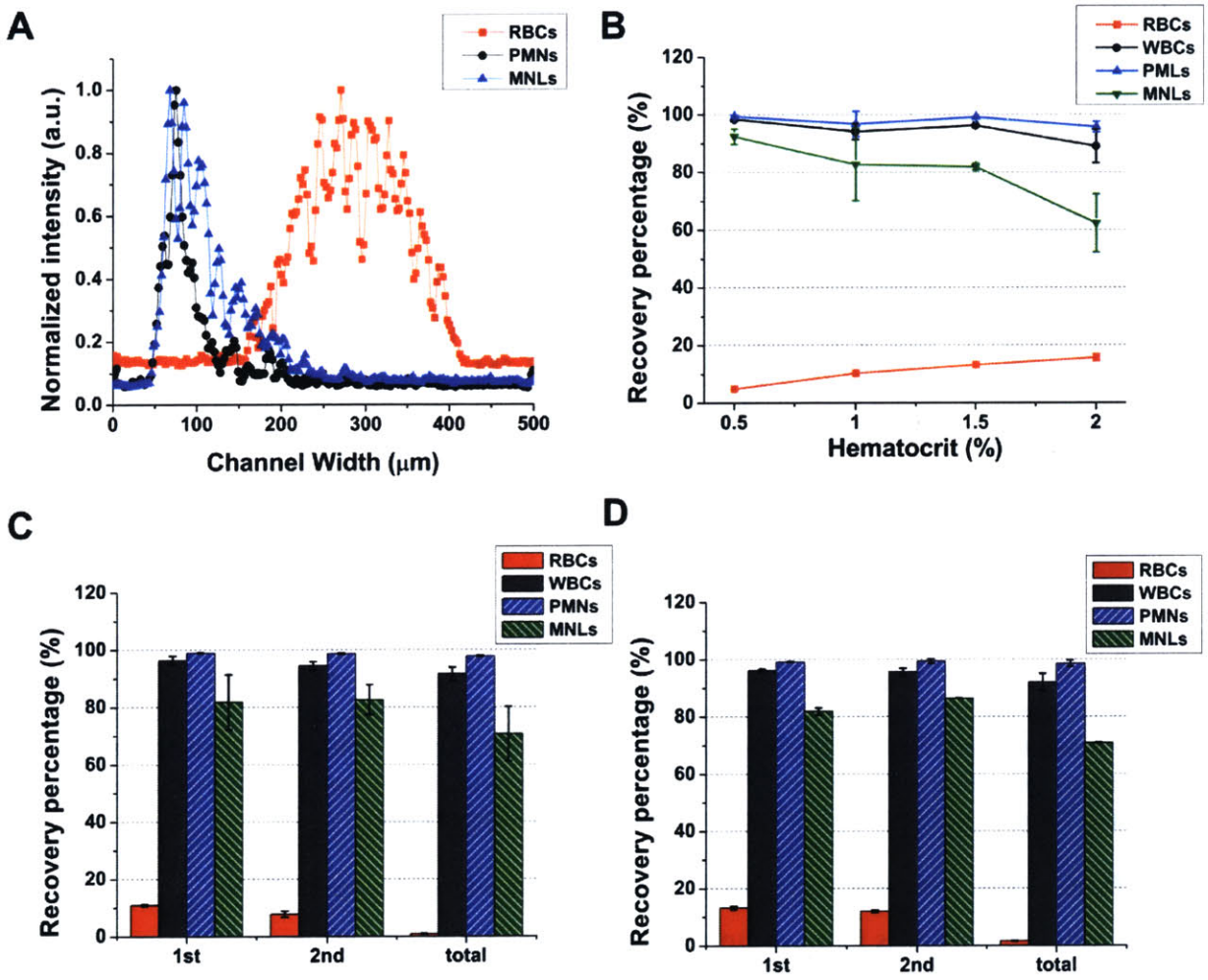

Figure 2.5 Characterization of blood cells in spiral channel with trapezoid cross-section. (**A**) Normalized intensity line scan indicating the distribution of polymorphonuclear leukocytes (PMLs), mononuclear leukocytes (MNLs) and RBCs (0.1% hematocrit) across channel width at 0.8 ml/min. The inner channel wall is represented by x = 0, and the outer channel wall is represented by x = 500. (**B**) Single-pass recovery percentage of total WBCs, PMNs, MNLs and RBCs at different hematocrit. Recovery percentage of 1% hematocrit (**C**) and 1.5% hematocrit (**D**) input sample after processed by trapezoid cross-sectional spiral in a 2-stage cascade manner. The amount of RBCs was measured by coulter counter, and the amounts of WBCs, PMNs and MNLs were based on FACS analysis of Hochest-positive, CD66b-positive cells, Hochest-positive but CD66b-negative cells, separately. Error bars indicate the standard deviation of results from three tests.

The device can also be used as a secondary step of differential centrifugation, whose performance was subjected to variation of blood source and manual transfer of different

cell layers to different tubes. It is often the case that some RBC residuals stay with the isolated WBCs after the first 30-min centrifugation and additional slow centrifugation washing steps or RBC lysis step are required to further RBC removal. Here we demonstrated the RBC removing ability of our device in processing buffy coat in a case where notable amount of RBCs were isolated along with WBCs by centrifugation (Figure 2.6). Based on the size distribution of cell sample, we observed that the WBC percentage (cell diameter: 6.6~15 μm) among the whole population increased from 30% to 91% after processing by our device.

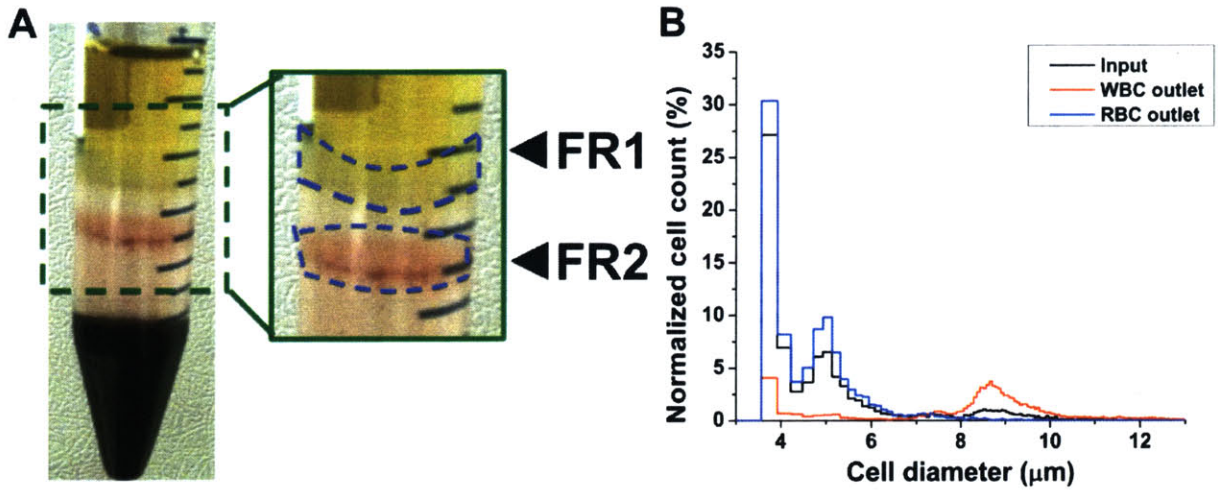

Figure 2.6 Spiral processing of buffy coat obtained via differential centrifugation. (**A**) A photo of healthy blood sample after centrifugation with Mono-Poly Resolving Medium. The first layer (FR1) consisted of MNLs, while the second layer (FR2) contained the majority of PMNs and some RBC residual. Cells from these two layers were re-suspended in same volume of the original whole blood sample and further processed by our spiral microchannel with trapezoid cross-section. (**B**) Size distribution of cells in input and output samples of the trapezoid cross-sectional spiral microchannel.

2.5.2 Effect of RBC Removal Techniques on the Immune-Phenotype of PMNs

Gentle depletion of RBCs from sample is crucial for the downstream analysis on remaining cells. In a recent study, the overall gene expression profile and cell viability was measured for cancer cells, MCF7, after inertial separation under $Re_c = 21$ and no significant affects caused by the separation process were observed compared to the unsorted control sample [24], indicating transient exposure of cells to shear condition in short time scale might not be enough to change the cell function. For the described spiral device here, the viability of isolated WBCs was found to be 98.22% ± 0.83% (trypan blue staining; input: 98.05% ± 1.08%) and their ability of producing reactive oxygen species in response to *in vitro* stimuli (PMA) has been measured by NBT test. As shown in Figure 2.7A, PMNs isolated by both spiral process and differential centrifugation remained passive but were able to reduce NBT at the presence of 1 μM PMA. Given the high sensitivity of white blood cells to external stimuli, we compared the effect of different RBC removal techniques on the expression level of cell surface marker (Figure 2.7B), CD18, which is a classical activation marker for PMNs. Both spiral process and centrifugation using MP-RM had negligible effect on PMN

activation, whereas the RBC lysis method increased the percentage of activated PMNs significantly and could potentially affect the phenotype and gene expression profile.

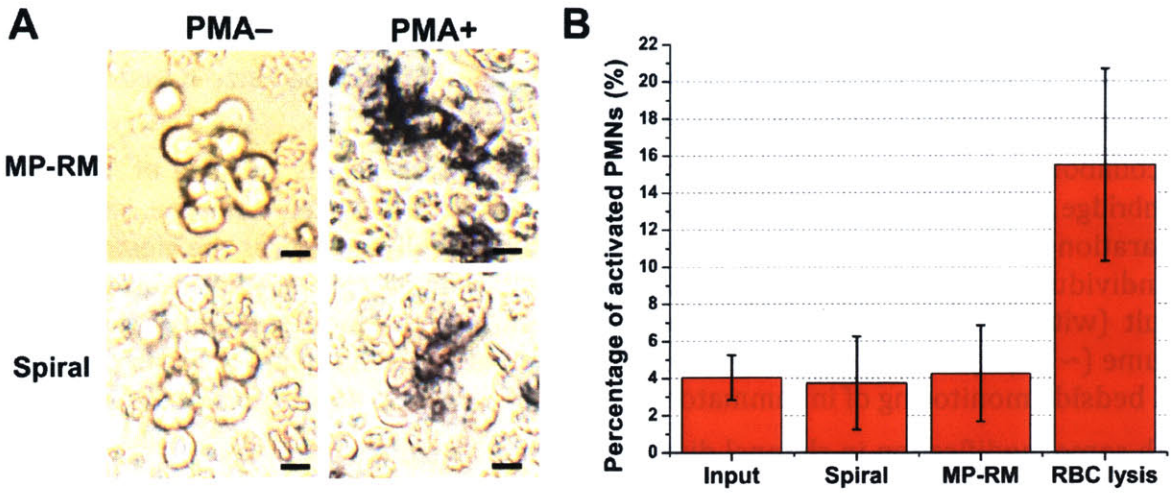

Figure 2.7 Comparison of PMN activation by spiral and other RBC removal techniques. (**A**) Nitroblue-tetrazolium (NBT) test on WBCs isolated by differential centrifugation method (MP-RM) or spiral process under condition with or without 1 μM PMA. Scale bar: 10 μm. (**B**) Comparison of activated PMNs in sample processed by different RBC removal methods based on FACS analysis of CD66b+ CD18 + cells. Error bars represent standard deviation of results from three tests.

2.6 Conclusions and Future Directions

2.6.1 Section Summary

In this work, we developed a novel, high-throughput RBC removal technique using trapezoid cross-sectional spiral, which provides higher resolution separation as compared to rectangular cross-section with similar dimensions. To our knowledge, this is the first experimental demonstration where the asymmetry velocity field within a trapezoid spiral channel affects the inertial focusing phenomenon, indicating the feasibility of using channel cross-sectional geometry (other than width and depth) as a parameter for optimization of curvilinear inertial microfluidic sorter. Our size-based separation technique eliminates the needs for long-term exposure of blood cells in nonphysiological condition and thus minimizes artificial alterations on cellular phenotypes during separation. While clogging and low throughput are major drawbacks for most microfluidic size-based separation methods which utilize membranes [46] or micron-sized pillars [47],the large dimensions of our device enables large volume sample processing with no clogging issues. As compared to other types of continuous cell separation methods, such as DLD and PFF techniques, our spiral microchannel functions at high operation flow rate (~mL/min) with large channel dimension accommodating the abundant RBCs (up to ~2% HCT), and thus possesses high throughput and is amenable to process blood samples. The highly repeatable performance and ability in enriching WBCs to >90% of total cell population also makes it a good choice to complete deplete RBCs from various biological fluids when used alone or in combination of differential centrifugation. Further optimization of channel cross-section and other

structural features is possible to apply this technique in many other primary cell separation problems.

2.6.2 On-Going Works and Future Directions

There are several on-going works in our lab utilizing the developed size-based cell sorting technique and two examples are shown as below.

In collaboration with Prof. Joel Voldman's group (Massachusetts Institute of Technology, Cambridge, MA, USA), we integrate the exact spiral cell sorter with the iso-dielectric separation (IDS) system. The integrated system successfully measures the electrical profile of individual leukocytes in a continuous manner at single cell level, and provides rapid result (within 15min) on leukocyte activation status for blood sample of fingerpicking volume (~20 μL). Thus, such integrated system might be useful in point of care application and bedside monitoring of inflammatory disease progression at fine temporal resolution.

With some modification in channel dimension, the trapezoidal cross-section spiral has also been employed by our group and collaborators in Singapore to isolate circulating tumor cells (CTCs). The optimized spiral CTC sorter is capable to isolate CTCs from clinically relevant blood volumes rapidly (7.5ml whole blood under 8min) with very high selectivity (99.99% removal of WBCs) and recovery (90% for CTCs) [48, 49]. Successful implementation of various downstream analysis has been performed on the retrieved CTCs, including genomic characterization using fluorescence *in situ* hybridization (FISH) and DNA sequencing, and proteomic characterization using immunofluorescence. Moreover, the retrieved CTCs were unlabeled and viable with a potential for propagation in downstream *in vitro* cell culture. Active efforts are carried out in optimizing the culture conditions for CTCs.

2.7 Section Acknowledgements

This research was supported by the National Research Foundation Singapore through the Singapore MIT Alliance for Research and Technology Centre's BioSyM IRG research programme. This work was also the financially supported by DARPA DLT (Dialysis-Like Therapeutics) program, under SSC Pacific grant N66001-11-1-4182.

2.8 References

[1] Jorgensen, P. and Tyers, M., *How Cells Coordinate Growth and Division.* Current Biology, 2004. **14**(23): p. R1014-R1027.

[2] DONG, X.-F., BERTHOIS, Y., COLOMB, E., and MARTIN, P.-M., *Cell Cycle Phase Dependence of Estrogen and Epidermal Growth Factor (EGF) Receptor Expression in MCF-7 Cells: Implications in Antiestrogen and EGF Cell Responsiveness.* Endocrinology, 1991. **129**(5): p. 2719-2728.

[3] Maruvada, P., Dmitrieva, N.I., East-Palmer, J., and Yen, P.M., *Cell Cycle-dependent Expression of Thyroid Hormone Receptor- β Is a Mechanism for Variable Hormone Sensitivity.* Molecular Biology of the Cell, 2004. **15**(4): p. 1895-1903.

[4] Taylor, I.W., Hodson, P.J., Green, M.D., and Sutherland, R.L., *Effects of Tamoxifen on Cell Cycle Progression of Synchronous MCF-7 Human Mammary Carcinoma Cells.* Cancer Research, 1983. **43**(9): p. 4007-4010.

[5] Majore, I., Moretti, P., Hass, R., and Kasper, C., *Identification of subpopulations in mesenchymal stem cell-like cultures from human umbilical cord.* Cell Commun. Signal, 2009. **7**(6).

[6] Guder, W.G., Narayanan, S., Wisser, H., and Zawra, B., *Samples: From the Patient to the Laboratory: The impact of preanalytical variables on the quality of laboratory results.* 1st ed. 1996, Darmstadt, Germany: GIT Verlag.

[7] Al-Soud, W.A. and Rådström, P., *Purification and Characterization of PCR-Inhibitory Components in Blood Cells.* Journal of Clinical Microbiology, 2001. **39**(2): p. 485-493.

[8] Fredriksson, K., Stridh, H., Lundahl, J., Rennard, S.I., and Skold, C.M., *Red Blood Cells Inhibit Proliferation and Stimulate Apoptosis in Human Lung Fibroblasts In Vitro.* Scandinavian Journal of Immunology, 2004. **59**(6): p. 559-565.

[9] Atkin, S.L., Hipkin, L., Radcliffe, J., and White, M.C., *Hypotonic lysis of red blood cell contamination from human anterior pituitary adenoma cell preparations.* In Vitro Cell Dev Biol Anim, 1995. **31**(9): p. 657-8.

[10] Needham, P.L., *The separation of human blood using 'Mono-Poly Resolving Medium'.* Journal of Immunological Methods, 1986. **99**: p. 283-284.

[11] Selzner, N., et al., *Water induces autocrine stimulation of tumor cell killing through ATP release and P2 receptor binding.* Cell Death and Differentiation 2004. **11**: p. S172–S180.

[12] Fukuda, S. and Schmid-Schönbein, G.W., *Centrifugation attenuates the fluid shear response of circulating leukocytes.* Journal of Leukocyte Biology, 2002. **72**(1): p. 133-139.

[13] Lundahl, J., Halldén, G., Hallgren, M., Sköld, C.M., and Hed, J., *Altered expression of CD11b/CD18 and CD62L on human monocytes after cell preparation procedures.* Journal of Immunological Methods, 1995. **180**(1): p. 93-100.

[14] Tait, J.F., Smith, C., and Wood, B.L., *Measurement of Phosphatidylserine Exposure in Leukocytes and Platelets by Whole-Blood Flow Cytometry with Annexin V.* Blood Cells, Molecules, and Diseases, 1999. **25**(5): p. 271-278.

[15] van Oss, C.J., Bronson, P.M., Dinolfo, E.A., and Chadha, K.C., *Two methods for the removal of erythrocytes from buffy coats for the production of human leukocyte interferon.* Immunological communications., 1981. **10**(6): p. 549-555.

[16] Consortium, M.o.t.T.R., *Standardizing global gene expression analysis between laboratories and across platforms.* Nature Methods, 2005. **2**(5): p. 351-356.

[17] Hou, H.W., et al., *Microfluidic Devices for Blood Fractionation.* Micromachines, 2011. **2**(3): p. 319-343.

[18] Toner, M. and Irimia, D., *Blood-on-a-chip*, in *Annual Review of Biomedical Engineering*. 2005, Annual Reviews: Palo Alto. p. 77-103.

[19] Huang, L.R., Cox, E.C., Austin, R.H., and Sturm, J.C., *Continuous Particle Separation Through Deterministic Lateral Displacement.* Science, 2004. **304**(5673): p. 987-990.

[20] Yamada, M., Nakashima, M., and Seki, M., *Pinched Flow Fractionation: Continuous Size Separation of Particles Utilizing a Laminar Flow Profile in a Pinched Microchannel.* Analytical Chemistry, 2004. **76**(18): p. 5465-5471.

[21] Downey, G.P., et al., *Retention of leukocytes in capillaries: role of cell size and deformability.* Journal of Applied Physiology, 1990. **69**(5): p. 1767-1778.

[22] Daniels, V.G., Wheater, P.R., and Burkitt, H.G., *Functional histology: A text and colour atlas.* 1979, Edinburgh: Churchill Livingstone.

[23] Mach, A.J. and Di Carlo, D., *Continuous scalable blood filtration device using inertial microfluidics.* Biotechnology and Bioengineering, 2010. **107**(2): p. 302-311.
[24] Hur, S.C., Henderson-MacLennan, N.K., McCabe, E.R.B., and Di Carlo, D., *Deformability-based cell classification and enrichment using inertial microfluidics.* Lab on a Chip, 2011. **11**(5): p. 912-920.
[25] Di Carlo, D., Irimia, D., Tompkins, R.G., and Toner, M., *Continuous inertial focusing, ordering, and separation of particles in microchannels.* Proceedings of the National Academy of Sciences, 2007. **104**(48): p. 18892-18897.
[26] Bhagat, A.A.S., Kuntaegowdanahalli, S.S., and Papautsky, I., *Continuous particle separation in spiral microchannels using dean flows and differential migration.* Lab on a Chip, 2008. **8**(11): p. 1906-1914.
[27] Di Carlo, D., Edd, J.F., Irimia, D., Tompkins, R.G., and Toner, M., *Equilibrium Separation and Filtration of Particles Using Differential Inertial Focusing.* Analytical Chemistry, 2008. **80**(6): p. 2204-2211.
[28] Kuntaegowdanahalli, S.S., Bhagat, A.A.S., Kumar, G., and Papautsky, I., *Inertial microfluidics for continuous particle separation in spiral microchannels.* Lab on a Chip, 2009. **9**(20): p. 2973-2980.
[29] Seo, J., Lean, M.H., and Kole, A., *Membrane-free microfiltration by asymmetric inertial migration.* Applied Physics Letters, 2007. **91**(3): p. 033901-3.
[30] Green, J.V. and Murthy, S.K., *Microfluidic enrichment of a target cell type from a heterogenous suspension by adhesion-based negative selection.* Lab on a Chip, 2009. **9**(15): p. 2245-2248.
[31] Bhagat, A.A.S., Hou, H.W., Li, L.D., Lim, C.T., and Han, J., *Pinched flow coupled shear-modulated inertial microfluidics for high-throughput rare blood cell separation.* Lab on a Chip, 2011. **11**(11): p. 1870-1878.
[32] Inglis, D.W., Riehn, R., Austin, R.H., and Sturm, J.C., *Continuous microfluidic immunomagnetic cell separation.* Applied Physics Letters, 2004. **85**(21): p. 5093-5095.
[33] ZENG, L., BALACHANDAR, S., and FISCHER, P., *Wall-induced forces on a rigid sphere at finite Reynolds number.* Journal of Fluid Mechanics, 2005. **536**: p. 1-25.
[34] Chun, B. and Ladd, A.J.C., *Inertial migration of neutrally buoyant particles in a square duct: An investigation of multiple equilibrium positions.* Physics of Fluids, 2006. **18**(3): p. 031704.
[35] Bhagat, A.A.S., Kuntaegowdanahalli, S.S., and Papautsky, I., *Inertial microfluidics for continuous particle filtration and extraction.* Microfluidics and Nanofluidics, 2009. **7**(2): p. 217-225.
[36] Dean, W.R., *XVI. Note on the motion of fluid in a curved pipe.* Philosophical Magazine Series 7, 1927. **4**(20): p. 208-223.
[37] Dean, W.R., *LXXII. The stream-line motion of fluid in a curved pipe (Second paper).* Philosophical Magazine Series 7, 1928. **5**(30): p. 673-695.
[38] Ookawara, S., Agrawal, M., Street, D., and Ogawa, K., *Quasi-direct numerical simulation of lift force-induced particle separation in a curved microchannel by use of a macroscopic particle model.* Chemical Engineering Science, 2007. **62**(9): p. 2454-2465.
[39] Russom, A., et al., *Differential inertial focusing of particles in curved low-aspect-ratio microchannels.* New Journal of Physics, 2009. **11**: p. 075025.

[40] Chatterjee, A., Kuntaegowdanahalli, S.S., and Papautsky, I., *Inertial microfluidics for continuous separation of cells and particles.* Proceedings of the SPIE, 2011. **7929**: p. 792907.
[41] Ookawara, S., Higashi, R., Street, D., and Ogawa, K., *Feasibility study on concentration of slurry and classification of contained particles by microchannel.* Chemical Engineering Journal, 2004. **101**(1–3): p. 171-178.
[42] Yamada, M. and Seki, M., *Hydrodynamic filtration for on-chip particle concentration and classification utilizing microfluidics.* Lab on a Chip, 2005. **5**(11): p. 1233-1239.
[43] Han, K.-H. and Frazier, A.B., *Lateral-driven continuous dielectrophoretic microseparators for blood cells suspended in a highly conductive medium.* Lab on a Chip, 2008. **8**(7): p. 1079-1086.
[44] Han, K.-H. and Frazier, A.B., *Paramagnetic capture mode magnetophoretic microseparator for high efficiency blood cell separations.* Lab on a Chip, 2006. **6**(2): p. 265-273.
[45] Sethu, P., et al., *Microfluidic Isolation of Leukocytes from Whole Blood for Phenotype and Gene Expression Analysis.* Analytical Chemistry, 2006. **78**(15): p. 5453-5461.
[46] Bruil, A., et al., *Asymmetric membrane filters for the removal of leukocytes from blood.* Journal of Biomedical Materials Research, 1991. **25**(12): p. 1459-1480.
[47] Panaro, N.J., Lou, X.J., Fortina, P., Kricka, L.J., and Wilding, P., *Micropillar array chip for integrated white blood cell isolation and PCR.* Biomolecular Engineering, 2005. **21**(6): p. 157-162.
[48] Warkiani, M.E., et al., *Slanted spiral microfluidics for the ultra-fast, label-free isolation of circulating tumor cells.* Lab on a Chip, 2014. **14**(1): p. 128-137.
[49] Khoo, B.L., et al., *Clinical Validation of an Ultra High-Throughput Spiral Microfluidics for the Detection and Enrichment of Viable Circulating Tumor Cells.* PLoS ONE, 2014. **9**(7): p. e99409.

Chapter 3 Microfluidic Platform for Single-cell Protease Activity Measurement

This section contains extracted text and results from previous publication by the thesis contributor:

- *"High-throughput protease activity cytometry reveals dose-dependent heterogeneity in PMA-mediated ADAM17 activation", Integrative Biology, 2015, 7(5): p. 513-524, authored by Lidan Wu, Allison M. Claas, Aniruddh Sarkar, Douglas A. Lauffenburger, Jongyoon Han. Lidan Wu (thesis author) was the first author of this publication, where she designed and carried out the experiments. Allison M. Claas helped out in bulk assays. Aniruddh Sarkar contributed in data analysis. Jongyoon Han supervised the research. All authors listed have contributed to the manuscript.*

As key components of autocrine signaling, pericellular proteases, A Disintegrin and Metalloproteinases (ADAMs) in particular, are known to impact the microenvironment of individual cells and have significant implications in various pathological situations including cancer, inflammatory and vascular diseases [1-3]. There is great incentive to develop a high-throughput platform for single-cell measurement of pericellular protease activity, as it is essential for studying the heterogeneity of protease response and the corresponding cell behavioral consequences. In this chapter, we develop a microfluidic platform to simultaneously monitor protease activity of many single cells in a time-dependent manner. This platform isolates individual microwells rapidly on demand and thus allows single-cell activity measurement of both cell-surface and secreted proteases by confining individual cells with diffusive FRET-based substrates. In case study I with this platform, we observe dose-dependent heterogeneous protease activation of HepG2 cells treated with phorbol 12-myristate 13-acetate (PMA). To study the temporal behavior of PMA-induced protease response, we monitor the pericellular protease activity of the same single cells during three different time periods and reveal the diversity in the dynamic patterns of single-cell protease activity profile upon PMA stimulation. The unique temporal information of single-cell protease response can help unveil the complicated functional role of pericellular proteases. In case study II (unpublished), we apply the developed platform to study the single-cell protease activity behavior of parental and gefitinib-resistant HCC827 cells. We observe discrepancy between the protease response derived from single-cell measurement and population-averaged assay, suggesting a potential role of cell-cell communication in the protease response of HCC827 cells.

3.1 Introduction

3.1.1 Pericellular Proteases: Key Players of Cellular Microenvironment

A Disintegrin and Metalloproteinases (ADAMs), a family of transmembrane proteins with peptide cleavage activities, have been shown to be the principal mediators of protein ectodomain shedding on the cell surface [4]. Together with the closely-related matrix metalloproteinases (MMPs), ADAMs process and cleave hundreds of proteins including

cytokines, receptors, growth factors and adhesion molecules and hence regulate many key cell signaling pathways via the modulation of the cellular microenvioronment [5-7]. There is increasing evidence to support the significant contributions of ADAMs in many physiological and pathological processes, ranging from multi-cellular organism development, wound healing to tumorigenesis, and thus ADAMs have been recognized as potential therapeutic targets in various diseases [1-3]. The most established role of ADAMs, especially ADAM17 and ADAM10, is in cancer formation and progression [8], where the ADAM-mediated shedding of EGF family members is associated with increased cell proliferation, migration and survival [4]. A recent study revealed that the autocrine signaling via protease-mediated EGF ligand shedding could stimulate the directed migration of individual human mammary epithelial cells (HMECs) without affecting their close neighborhood [9]. The studies suggested that variability in single-cell protease activity could lead to diverse intracellular kinase activation profiles or cell migration patterns in response to the same stimuli, which might contribute to the resistance development against cancer therapies. Indeed, on one hand, the active ADAMs on the cell surface are generally considered to promote malignancy since they activate the growth factor ligands via proteolysis, and selective inhibitors against ADAM17 in particular have been shown to restore the sensitivity of gefitinib resistant non-small cell lung cancer (NSCLC) [10]. On the other hand, ADAMs could also shed the growth factor receptors from the cell surface and researchers have found that the receptor accumulation resulting from ADAM inhibition could enhance the activation of compensatory signaling pathway involved in the drug resistance development of endometriosis [11]. Therefore, there is an emerging need in studying the heterogeneity of protease response of individual cancer cells and its cell behavioral consequences. The first step towards any relevant biological study is to develop an appropriate technique for single-cell measurement of pericellular protease functional characteristics.

3.1.2 Current Methodologies for Single-Cell Measurement of Pericellualr Protease Activity

Unlike MMPs, ADAMs are primarily located at the cell membrane and function in the pericellular space. Beside the multiple post-translational modifications and other intracellular regulatory mechanisms mediating the proteolytic activity of ADAMs, the local balance between active ADAMs and their physiological inhibitors in the extracellular environment also determines the actual function of those enzymes [12-14]. Moreover, one recent study on endometriosis discovered a counter-intuitive decrease in both MMP-2 and ADAM-9 protease activities in the presence of reduced concentration of TIMP-4 protease inhibitor [15], further suggesting the catalytic activity to be a better surrogate marker for the ADAM functionality than the protein expression. Pericellular activity measurement of proteases primarily relied on various fluorescent reporter systems that generated fluorescence upon reaction with proteases, and the key issue of single-cell measurement is to constrain the readout to individual cells. Many existing methodologies utilize the translocation of fluorescence generating systems into the cytoplasm to enable single cell detection [16-19] and significant throughput has been achieved when conjugated with flow cytometry. But caution must be taken as the translocation of extensive amount of exogenous molecules into the cytoplasm could potentially interfere with the intracellular singling events. Another big category of single-cell protease activity measurement in

pericellular space is based on dye quenched (DQ) extracellular matrix (ECM) proteins [20, 21]. Coupled with advanced live-cell imaging system, DQ-ECM substrates have been shown to be useful in monitoring the spatio-temporal proteolysis events associated with cell migration and cell-cell interaction [21, 22]. Despite the benefits of DQ-ECM systems, an important drawback is that the DQ-ECM approach for single-cell pericellular protease measurement not only requires prior nuclear labeling that is known to interfere with cellular processes [23], but also imposes high demands on the imaging setup in many aspects including cell tracking, data memory, and spatial and temporal resolution of measurements. Nevertheless, the signaling response associated with protease-mediated shedding could be very rapid and dynamic [24]. For example, as a typical downstream signaling process of cell surface receptors' binding to their ligands, early responses like calcium flux could happen within several seconds to minutes, while the subsequent intracellular kinase reaction cascade and transcriptional changes might take minutes to hours to occur. Therefore, to reveal the underlying regulation mechanisms associated with pericellular protease function, it is valuable to develop a novel methodology for single-cell protease activity measurement. An ideal measurement method would not only work in higher time resolution at considerable throughput, but also be compatible with conventional activity/concentration measurements and cell culture techniques, with minimal preparation and perturbation. This is especially important considering that the major goal of single-cell assays is to compare and contrast the signals at the bulk and single-cell levels, to elucidate both the role of critical subpopulations and any emergent population behaviors.

3.1.3 Our Approach for Protease Activity Study at Single-Cell Resolution

Microfluidics systems, which have been increasingly recognized as a useful tool in biological studies, offer the tremendous advantages in single-cell analysis [25, 26]. Until now, many different kinds of microfluidic chips have been developed to allow the manipulation and analysis of cells within the miniaturized devices in a controlled and reproducible way. Diverse single-cell assays against various molecular properties such as cellular transcriptome and secretory profile, or biophysical properties such as deformability and density, have also been realized in microfluidic platforms [27, 28]. Particularly, isolating individual cells with microwell arrays or discrete microchambers has emerged as a popular and robust approach for microfluidic single-cell platform. With appropriate engineering, microwell-based systems hold generic applicability to versatile biological problems. Both mammalian cell culture [29, 30] and ELISA-like measurement of secretary molecules [31, 32] have been successfully demonstrated with microwell-based systems for high-throughput single-cell study.

In this work, we develop a flexible yet robust microfluidic approach of multiwell confinement for single-cell measurement of pericellular protease activity. We take advantage of a microfluidic platform with valving function [33] to control the molecular transport of individual microwells and also to confine the fluorescence readout signal from each cells for higher detection sensitivity. Since our platform has very little requirement on sensing substrates, various commercially available FRET-based substrates with high specificity against certain protease(s) could be used in the same manner as corresponding bulk assays. Potential multiplexed protease activity profiling is possible when assayed

with panels of moderately specific FRET-based protease substrates with different fluorescence spectra [34]. As a proof-of-concept, in case study I, we demonstrate the capability of single-cell protease activity measurement using adherent human hepatocellular carcinoma cell line, HepG2, and study its ADAM17 protease response mediated by PMA, a potent inducer of inflammation. Furthermore, since the microfluidic platform allows us to replace the medium within microwells easily and rapidly, we are able to monitor the temporal evolution of pericellular protease response of the same single cell. Results derived from our temporal protease activity profiling reveal that the extracellular protease activity profile could have diverse temporal dynamic patterns at the single-cell level. Moreover, the data indicates that the typical analogue dose-response relationship observed at the bulk level might have root in the dose-dependent effect of stimulant on single cells' signaling dynamics. Although the physiological significance of the asynchronous single-cell protease response is unclear, our results open up the possibility that heterogeneous protease response may have an impact on the dynamic interaction of the protease-mediated autocrine-signaling network, which may result in diverse cell fate decisions.

3.3 Materials and Methods

3.3.1 Device Fabrication

For the bottom piece of the microfluidic platform, arrays of microwells were made of polydimethysiloxane polymer (PDMS, Sylard 184 Silicone Elastomer Kit, Dow Corning, USA) using standard soft lithography techniques from a SU8-patterned silicon master. Individual microwell was cuboid in shape with a volume of 1.89 nL (area of 100 x 100 μm^2 with a depth of 189 μm), arranging into 5 x 6 blocks with well-to-well interval of 190 μm. The microwell dimensions described were empirically established for easy monitoring of cellular morphology and locomotion of adherent mammalian cells with 15~20 μm in diameter. The access channels between each block had the same depth and width as that of microwells, and were designed to facilitate the liquid convection across the microwell array during operation. Each microwell array containing 4 x 8 blocks of microwells (960 microwells per array) was patterned on the center area of a 1 mm-thick PDMS slab laying facing up on top of a 1.5" x 1.5" glass slide (VWR® Plan Micro Slides, VWR International LLC, USA), and used for cell culture.

The top piece of the microfluidic platform was also made of PDMS polymer and comprised of a flow chamber layer and a valve control layer. The flow chamber layer contained an 8 mm x 15 mm x 100 μm (width x length x depth) straight channel, both ends of which were connected to the inlet and outlet reservoirs via branching channels. The valve control layer is positioned directly on top of the flow chamber layer and formed a 15 mm x 8 mm x 200 μm straight channel via irreversible plasma bonding. This is where the pressure would be applied to control the closing and opening of the underneath flow chamber (Figure 3.1).

3.3.2 Preparation of Microwell Arrays and Cell Culture

The PDMS microwell array on a glass slide was placed within a 35 mm x 10 mm tissue culture dish and treated with oxygen plasma (Harrick Plasma Cleaner/Sterilizer, Harrick Plasma, Inc., USA) for 1 min to sterilize the surface. To promote cell adhesion, plasma-

treated microwell array was first incubated with 0.02 N sterile acetic acid containing 40 μg/mL rat collagen I (A1048301, Invitrogen, USA) at room temperature for 1h, followed by washing with 1x PBS three times to remove unbound collagen molecules and residual acid. Then, in HepG2 study (case study I), suspensions of HepG2 cells (HB-8065, ATCC, USA) were deposited onto the surface of the microwell array at 1.2 x 10^5 cells/mL concentration in complete medium, which consists of Eagle's minimum essential medium (EMEM; 30-2003, ATCC, USA), 10% fetal bovine serum (16000, Invitrogen, USA), 50 U/mL of Penicillin and 50 U/mL of Streptomycin (15070-063, Invitrogen, USA). Cells were allowed to settle down for 5~6 min before the surface of microwell array was gently washed with medium from the side to remove the cells in the access channels or outside microwells. The microwell array seeded with cells would then be submerged in complete medium and incubated at 37 °C with 5% CO_2 for 8~10 h before being subjected to overnight serum starvation and assayed on the second day. Visual inspection of the cell-loaded microwell array by microscopy suggested that the sedimentation of cells into microwells followed a Poisson distribution and thus on average ~25% of total microwells contained single cells.

The similar procedure was performed in HCC827 study (case study II) with modification in the cells and culture medium used. Parental HCC827 cells (CRL-2868, ATCC, USA) are kind gift from Prof. Douglas A. Lauffenburger (Massachusetts Institute of Technology, Cambridge, MA, USA). The gefitinib-resistant HCC827 cells are generated *in vitro* from the parental cells using a selection process adapted from [35]. Briefly, HCC827 cells were maintained in complete medium, which consists of RPMI 1640 (21870-076, Invitrogen, USA), 10% fetal bovine serum (S11150, Atlanta Biologicals, Inc, USA), 2 mM glutamine (35050-061, Invitrogen, USA), 100 U/mL of Penicillin and 100 U/mL of Streptomycin (15140-148, Invitrogen, USA). To generate a resistant cell line, parental HCC827 cells were exposed to 1 μM gefitinitib (G-4408, LC Laboratories, USA) and 50 ng/ml recombinant human HGF (hepatocyte growth factor; 294-HG, R&D Systems, USA) for 14 days, followed by another 14-day exposure of 1 μM gefitinib alone. After the 28-day selection process, the resulting cells exhibited resistance to gefitinib-induced cell death and were maintain in gefitinib-free complete medium for further expansion and assay.

3.3.3 Device Assembly and Operation

Prior to protease measurement, the top control piece of device would first be exposed to a 30 sec plasma treatment for sterilization and then be aligned manually onto the bottom cell-loaded piece that is covered by serum-free medium. Then the two pieces would be clamped together under light compression between plates of a homemade assembly chamber and the entire assembly would then be mounted within a stage top incubator (Tokai Hit Co., Ltd, Japan) onto an inverted epifluorescence microscope (Olympus IX71, Olympus Inc., USA) equipped with a motorized stage (H117 ProScan™ motorized stage, Prior Scientific Inc., USA) and a 12-bit CCD camera (SensiCam QE, PCO, Germany). The whole assembly process takes 5 minutes and the humidified incubator was kept at 37°C with 5% CO_2 supply for live-cell imaging. Sterile assay buffer or washing buffer was loaded within a syringe and pumped through the flow chamber formed between the top and bottom piece at varying flow rates using a syringe pump (Harvard Apparatus PHD 2000, Harvard Apparatus Inc., USA). The valve control chamber of the top piece was filled with deionized water and its inlet reservoir was connected to a gas controller. With no external

pressure applied to valve control chamber, the flow chamber was connected to reservoirs for buffer introduction and all microwells in the same array were exposed to the same fluidic environment. The flow chamber can be closed by applying 16 kPa to the valve control layer, and thus the valve membrane of control layer isolates the microwells underneath from each other to form discrete and closed compartments for protease activity measurement of individual microwells.

3.3.4 Device Characterization with Recombinant Protease

Different concentrations of recombinant human ADAM17 protease (930-ADB-010, R&D Systems, Inc., USA) were mixed with serum-free medium (EMEM) containing 10 μM ADAM17-specific FRET-based substrate (PEPDAB010, BioZyme, Inc., USA). Immediately after the mixing, sample mixture was injected to the flow chamber of the assembled device at 200 μL/min for 1 min followed by 40 μL/min for 10 min. Subsequently, 16 kPa pressure was applied to valve control chamber to isolate the microwells underneath. Fluorescence intensity of each closed microwell was recorded at 2.5-min intervals for 15 frames using a 10x objective lens with the help of a motorized stage. The starting time for time-lapse fluorescence intensity recording was $t = 14 \pm 1$ min after the mixing of substrates and recombinant enzyme.

3.3.5 Bulk Live-Cell Protease Activity Assays

Parental or gefitinib-resistant HCC827 cells were first seeded with complete medium into 96-well plate (3300, Corning® CellBIND®, Corning Incoporated, USA) at density of 15000 cells per well (i.e. ~469000 cells/cm^2) for 10 h, followed by overnight serum starvation. Subsequently, we changed the media to be serum-free medium (RPMI 1640 with glutamine) containing 10uM ADAM17-specific FRET-based substrate (PEPDAB010) along with either 1uM gefitinib or DMSO control. In all cases, media contained less than 0.5% DMSO. Upon the addition of substrate, cells were imaged at 15 min intervals for 2 h at 37 °C using plate reader (Varioskan™ flash multimode reader, Thermo Scientific Inc., USA) at excitation and emission wavelengths of 485nm and 530nm, respectively. We performed experiments in biological triplicate and included negative control with no cells seeded but otherwise treated with DMSO control. The Activity Index of bulk assay was calculated as the increasing rate of substrate fluorescence over time.

3.3.6 Single Live-Cell Protease Activity Assays

HepG2 cells or HCC827 cells seeded in collagen I-coated microwell arrays were cultured in the corresponding serum-free medium overnight before assayed for protease activity. For some assays, cells were pre-treated with various inhibitors, including Gö6983 (G1918, Sigma-Aldrich, USA), ERK inhibitor II FR180204 (328010, EMD Milipore, Germany) and TAPI2 (SML0420, Sigma-Aldrich, USA). For all assays, cells were pre-loaded with viability dye, 2 μM CellTrace™ calcein violet AM (C34858, Invitrogen, USA), for 30 min prior the device assembly. Following the device assembly and mounting onto a stage top incubator (37 °C, 5% CO2, humidified), cells were imaged briefly for the localization and viability under microscope at multiply positions along z direction. Then, assay buffer consisting of 10 μM ADAM17-specific FRET-based substrate, PEPDAB010, along with either different concentrations of phorbol 12-myristate 13-acetate (PMA; P1585, Sigma-Aldrich, USA) or

DMSO control in serum-free medium would be injected into the flow chamber at 200 μL/min for 1 min followed by 40 μL/min for 10 min. Then, cells in each microwells would be isolated by pressurizing the valve control chamber. In HepG2 study (case study I), the fluorescence intensity would be recorded at 2.5-min intervals for 36 min. In HCC827 study, the fluorescence intensity would be recorded at 8-min intervals for 15 frames (totally 114 min) instead. At the end of the 1st assay, the cells in microwells were rinsed at 40 μL/min for 15 min using fresh washing buffer, which had the same composition as the assay buffer used in the 1st run of measurement but contained no FRET-based protease substrates. The rinsed cell-loaded array can then be used in subsequent run of protease measurement if applicable. Once all the runs of protease measurement were done and the residual substrates were washed away, serum-free medium containing 3 μM propidium iodide (P3566, Invitrogen, USA) and 0.8 μM Hoechst 33342 (H1399, Invitrogen, USA) were injected into the flow chamber at 40 μL/min for 10 min to stain the cells post-measurement. Fluorescent images under different wavelength channels were taken for cells within microwells at multiple depth positions and would be used for subsequent data analysis of cell number and post-assay survival. Then, the device would be disassembled and the bottom piece loaded with stained cells in microwells were rinsed with fresh medium and kept within tissue culture dish with complete medium in cell culture incubator for further culture. On the day following single-cell protease measurements, cells would be stained with 2 μM calcein AM (354216, BD Biosciences, USA) for 20 min before imaging with microscope for the day 2 survival.

3.3.7 Data Analysis

Fluorescent images taken post-assay for cells stained with Hoechst 33342 and propidium iodide were scrutinized manually to count the cell number within individual microwells and to identify the location of each cells in the depth direction of microwell array. Images taken prior to the assay and on day 2 were also analyzed for cell survival across the entire assay. We excluded data from microwells with non-cell objects (dirt, impurity in coating solution, etc) or cells dead by day 2 from further analysis. For each microwell array, we could get valid data from more than 180 1-cell wells and 100 2-cell wells. Moreover, to avoid confounding factors relevant to the varying depth locations of individual cells, we only considered the single cells remaining at the bottom of each microwells during the entire assay period into the final protease activity analysis, unless otherwise stated. Usually, we got 60~70% of single cells located at the bottom of microwells by the time of protease measurement.

We have developed a procedure for signal processing and normalization of the protease measurement. As illustrated in Appendix Figure A.2, (i) the time-lapse raw images for the substrate cleavage were captured by fluorescence inverted microscope and then stabilized using Image Stabilizer plugin of Image J® software. Given the non-uniform illumination within observation window and the well-to-well interference due to light scattering, a normalization method was applied. (ii) Briefly, two templates were generated based on the raw images with the aid of MATLAB and defined the regions within each microwells and the background regions around the wells, respectively. (iii) The pixel intensity within each region was further sorted in ascending order and the extreme values at both ends would be discarded. The average value of the central ± 20% pixel intensity was then considered as

the intensity indicator for that region. In this manner, one can reduce the variation introduced by inaccurate microwell border identification and the presence of bright objects within microwell. (iv) For background regions, the average value became the normalized intensity. For microwell regions, the average value of each well region was further subtracted by the normalized intensity of its surrounding background region. Then, one can obtain time-lapse profile of normalized intensity for individual microwells. (v) We modeled the protease-mediated substrate cleavage as the classical Michaelis-Menten model, where the initial rate of cleavage is proportional to the concentration of active enzyme in the system with excessive substrate of nearly constant concentration. Therefore, we defined the protease activity index (AI) as the increasing rate (i.e. slope) of normalized fluorescence intensity and extracted the AI value for each region via robust linear least-squares fitting of the time-lapse normalized intensity profile. (vi) When dealing with different cell-loaded microwell arrays, we used the median AI value of empty microwells from each array as the reference value, to account for the spontaneous substrate cleavage occurred in the absent of cells within that particular array. We further calculated the normalized AI value by subtracting each microwell AI value with the reference value of the same array and used the resultant normalized AI value to evaluate the protease response of cells within different microwell arrays. Notice that all the histograms shown in this manuscript have been smoothened using MATLAB function *ksdensity().m* where the density estimation was based on a normal kernel function and the locations of kernel smoothing windows were robustly estimated via function *histogram().m*. Based on the normalized AI values of 0-cell wells, we also defined a threshold for high activity microwells to be beyond 2 standard deviations away from the average value of 0-cell wells' normalized AI values. Therefore, the threshold for HepG2 study (case study I) is normalized AI = 2, while the threshold for HCC827 study (case study II) is normalized AI =1 given the lower value and tighter distribution of 0-cell well's normalized AI values. Percentage of high activity microwells derived from a given protease assay then provides an indicator to quantify the overall protease response of all the single cells measured during that particular assay. Any p-values shown were calculated based on Welch's t-test.

3.4 Device Design and Characterizations

3.4.1 Device Design

Many conventional bulk cell measurements and some *in vivo* protease activity image techniques utilized synthetic FRET-based substrates that have high specificity against certain protease or protease class. Inspired by the popular microwell-based approach in microfluidic single-cell study, we established a multiwell platform to confine individual cells in discrete compartments during protease activity measurement with small molecule substrates with high diffusivity. Due to the enhanced signal readout via the confinement of the excessive diffusible substrates within microwells, the signal generated by pericellular protease-mediated reaction dominates the signal resulting from intracellular substrate cleavage events.

Compared to the existing methods, our approach has little requirement on substrate design and could be used for study of single-cell pericellular protease response in a time-dependent manner, as replenishing fresh substrate into the system allows for interrogation

of same cells for multiple times. The additional temporal information of protease response might have an impact on cellular outcomes since the dynamics of downstream kinase signaling network has been shown to be an important component of the cell fate decision process [36, 37]. Moreover, our platform is compatible with other single-cell study technologies, including various live-cell reporter systems for intracellular signaling events, micro-engraving for molecular secretory profile [31] and FISH assay for single-cell chromosome analysis.

Cell culture is performed with the bottom PDMS piece patterned with microwell array structure at the central region (Figure 3.1A). We observed healthy HepG2 morphology and cell proliferation on the microwell array over a 1-week tissue culture (Appendix, Figure A.1). Compared to a closed system, cells grown in those microwells would experience similar oxygen gradient and nutrient condition as conventional tissue culture, which is important for comparison between single-cell assay results with those from conventional bulk assays performed on cells grown on standard tissue culture plate. While the flow chamber used in this work is a simple straight channel with branched microfluidic connection to reservoirs for synchronized delivery of fluid across channel width (Figure 3.1B), the flow chamber could be modified to compose of a microfluidic generator [38] when on-chip stimulation with a spatial gradient of drug is desired.

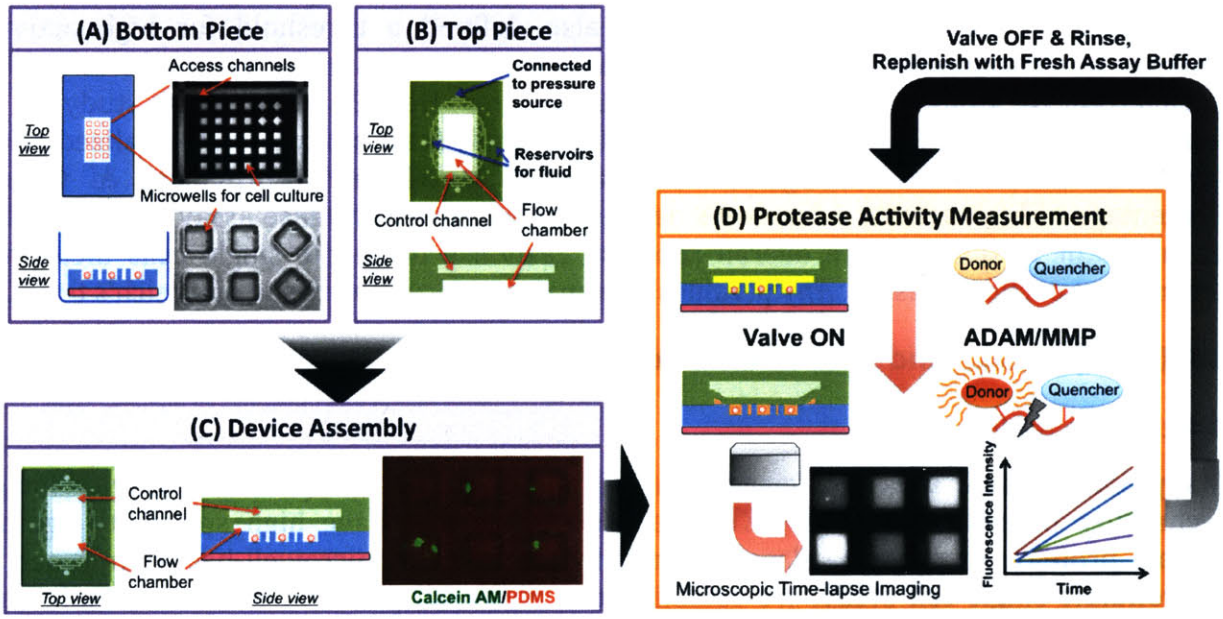

Figure 3.1 Schematics of microfluidic platform for single-cell protease activity measurement and the assay procedure. The platform is composed of two PDMS pieces, a bottom piece with microwell array pattern for cell culture (**A**) and a top piece with a 2-layer structure (**B**). Upon device assembly (**C**), the flow chamber is formed between the two pieces and is designed for injection of drug-containing buffer or reaction mixture with FRET-based protease substrate to the microwells. The top chamber of valve control layer allows the pneumatically actuation of flow channel ceiling to control the closing and opening of microwells. (**D**) After the introduction of assay buffer and the closing of microwells, the protease activity measurements were conducted via microscopic time-lapse imaging of fluorescence generating from the protease-specific substrate cleavage. For repeated measurements on the same cells, the microwell array was rinsed by introducing of fresh assay buffer without substrate at the end of each run. The rinsed cell-loaded array would then be used in the subsequent run of protease measurement after replenishing with fresh substrate-containing assay buffer.

3.4.2 Device Characterizations with Recombinant ADAM17

We first characterized the device performance with different amounts of ADAM17 recombinant protease mixed with FRET-based protease substrate. While current available substrates usually have cross-reactivity against closely related proteases, it is possible to distinguish between the proteases when the cleavage of multiple substrates by the same sample has been monitored [34]. In this work, we only used one kind of substrate in all the measurements and the substrate chosen has been demonstrated to have very high catalytic efficiency against ADAM17 over others [34]. As shown in Figure 3.2, we observed a positive correlation between the concentration of recombinant ADAM17 in the system and the measured microwell activity index (AI), defined as the increasing rate of fluorescence intensity resulting from the substrate cleavage. Meanwhile, the background AI values derived from the fluorescence of plateau regions around microwells remained low for all the conditions tested. Furthermore, we also noticed that as a consequence of light scattering and non-uniform illumination within the observation window of microscope, the distributed range of microwell AI values increased with the average AI value under same condition, resulting in a coefficient of variation (CV) of 15~20%. Thus, we considered more than 30% deviation from the original AI value to be the real change in protease activity measured by our platform.

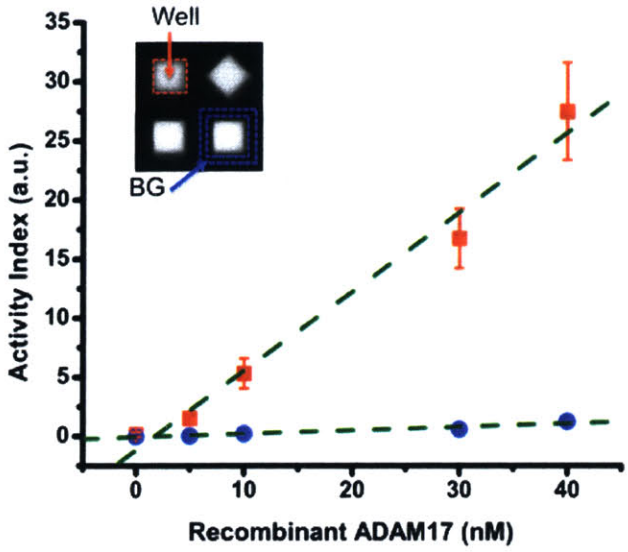

Figure 3.2 Device characterization with recombinant ADAM17. Sample mixture containing different concentrations of recombinant human ADAM17 protease and 10 μM FRET-based substrate was injected to the flow chamber of the assembled device. Fluorescence intensity was monitored for 36 min after the flow chamber was closed to isolated individual microwells. The activity index (AI), defined as the increasing rate of normalized fluorescence intensity was calculated (see Appendix Figure A.2) and is shown here for an individual microwell area (marked by red dash line in the inset) or plateau region around the microwell (marked by blue dash line in the inset). One can observe a positive correlation between recombinant protease concentrations in the system and the AI values for microwells. Red squares: microwell area (Well); Blue circles: plateau region around the microwell (BG); Green dash lines: linear fit of AI vs. ADAM17 concentration. Error bars indicate standard deviations of individual microwell AI values from duplicate assays using 2 different devices (n > 1800 per condition).

3.5 Case Study I: Dose-dependent Heterogeneity in PMA-mediated ADAM17 Activation of HepG2 Cells

3.5.1 PMA-Induced Protease Activity of Single HepG2 Cells

As one of the most common causes of cancer death, liver cancer results in the death of around 598,000 people yearly due to the poor prognosis [39]. Mounting evidence supports the association of poor prognosis with upregulation of many pro-inflammatory signals that can be cleaved and activated by ADAM17 protease, such as EGFR ligands and tumor necrosis factor alpha (TNF-α) [40]. Besides, the increased expression level of ADAM17 has also been observed in liver injury and liver cancer development [41]. Given the importance of protease study in liver cancer, we tested the functionality of our platform with human hepatoma HepG2 cells challenged with PMA, a potent inducer of inflammation that has been shown to activate the ADAM17-dependent shedding of multiple substrates [4]. As shown in Figure 3.3, cell-containing microwells in DMSO control case displayed low normalized AI values similar to those of empty wells, suggesting few active ADAM17 present at the cell surface under basal condition. Meanwhile, PMA challenge resulted in a long tailed distribution of single cells' normalized AI values with a large fraction of single cells exhibiting high protease activity level (5~28% at [PMA] ≥ 0.2 μM). Notice that the

threshold for high activity microwells defined in this work was chosen based on the normalized AI values of 0-cell wells and has been set to be normalized AI = 2, which was beyond 2 standard deviations away from the average value of 0-cell wells' normalized AI values. Moreover, we observed a dose-dependent relationship between the percentage of single cells with high protease activity and the PMA concentration (Figure 3.3B). These results indicate that PMA treatment could increase the cell surface ADAM17 activity of HepG2 cells and this is consistent with previous findings where PMA is known to massively stimulate the shedding of several ADAM17 protease substrates, such as TNF-α and c-Met, in HepG2 cells [42]. Interestingly, even under PMA concentration as high as 1 μM, there was still ~72% of single cells displaying a very low, baseline protease activity, at least during the assay time (i.e. PMA treatment tine, t_{PMA} = 15~51 min). The presence of those 'non—responding' cells reveals the inherent heterogeneity in protease response at the single-cell level and suggests that the escalating protease activity of a minority of fast-responding cells is the primary contributor of PMA-induced ADAM17 protease activation observed during short-term assay at the bulk scale.

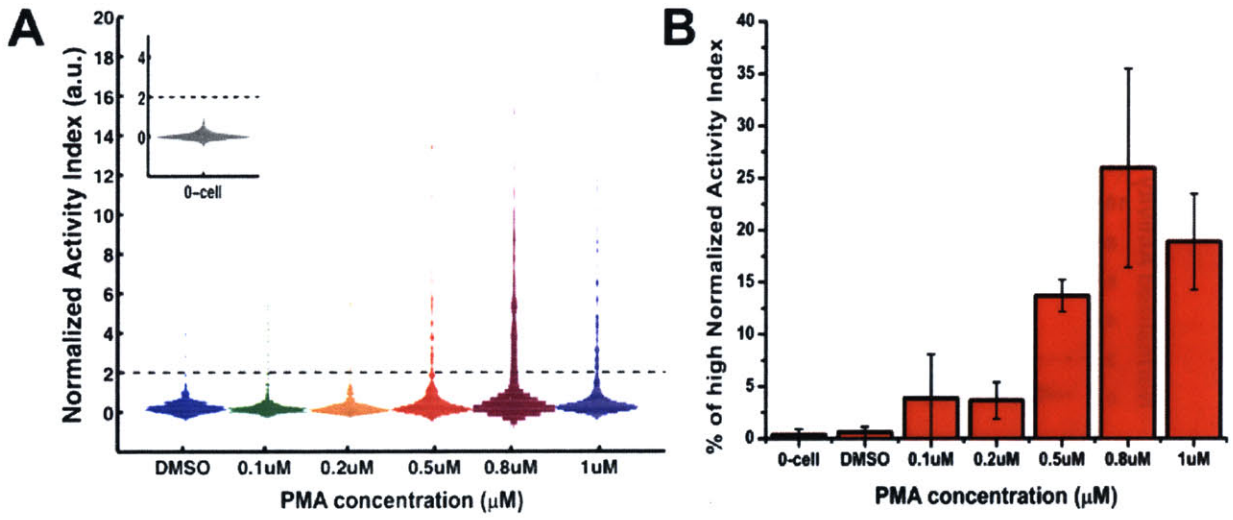

Figure 3.3 Heterogeneous protease response for HepG2 cells treated with DMSO or different concentrations of PMA (0.1, 0.2, 0.5, 0.8, 1 μM). The normalized activity index (AI) is shown for microwells containing single HepG2 cells. (**A**) Histogram of the normalized AI values for 1-cell wells (n >300 per condition). The inset shows the histogram of the normalized AI values for 0-cell wells. Dark dash lines mark the place where normalized AI value = 2. (**B**) Percentage of 1-cell wells with high normalized AI values (>2). Error bars represent standard deviation of a triplicate using three different arrays.

3.5.2 Signaling Components Involved in PMA-Mediated ADAM17 Protease Response

There are several distinct, potential mechanisms that could modulate the ADAM protease-mediated substrate cleavage. Cells' protease activity can be affected via the regulations on enzyme proteins' expression, maturation, trafficking to the cell surface and post-translational modifications that could prime the protease activity via the induction of protein conformational changes. Alternatively, modifications on the substrate proteins (i.e. cell surface receptors that are targets of ADAM-induced shedding) could also modulate the

cleavage event without affecting the catalytic activity of the responsible protease. Currently, the exact mechanism of PMA-induced ADAM-dependent shedding in HepG2 cell system is still not fully clarified. PMA is a strong and pleiotropic stimulus [43-45]. It is known to regulate the accessibility of the catalytic site of ADAM17 on the cell surface of mouse embryonic fibroblasts [46]. PMA is also a potent activator of PKC kinases[47] and Jurkat cells with PKC knockdown have been shown to be incapable of altering some substrate shedding in response to PMA challenge [48]. Moreover, the activation of PKC could lead to the activation of ERK cascade [49]. In HeLa cells, ERK activation is known to induce phosphorylation of the cytoplasmic domain of ADAM17 protein and accelerate its transportation to cell surface [50], where the active ADAM protease plays an important role in autocrine signaling. However, contradictory evidence also exists regarding the role of ERK kinases in PMA-mediated ADAM17 activation. In mouse monocytic cells [51] and fibroblast cells [52], researchers observed no altered transport of ADAM17 to cell surface upon PMA challenge and found that the cytoplasmic domain of ADAM17 was not even required for PMA-induced ADAM17-dependent EGFR ligand shedding.

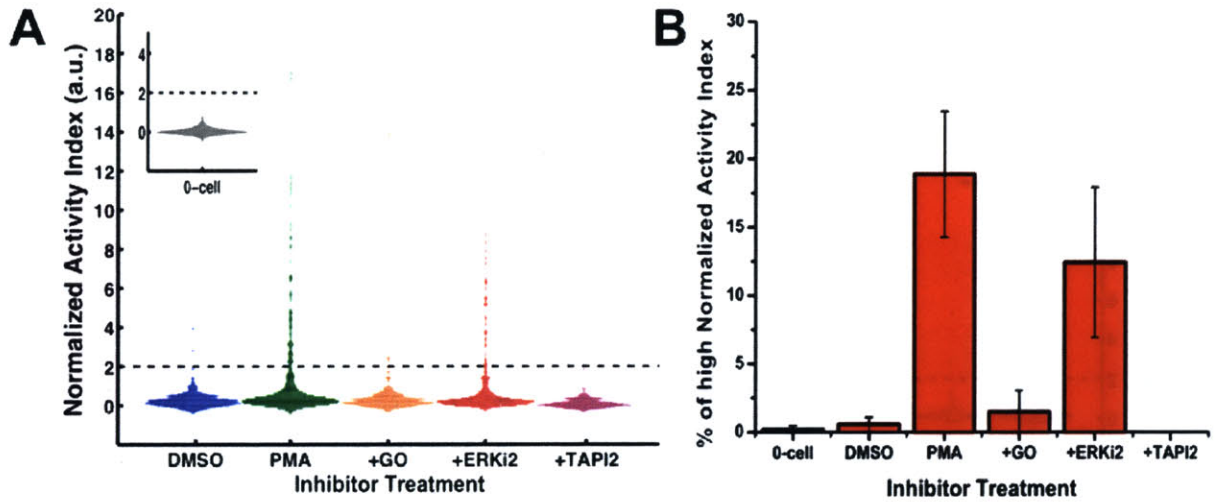

Figure 3.4 Inhibitors against different components of signaling pathway suppressed the PMA-induced protease activity increase in HepG2 cells. Serum-starved HepG2 cells were first incubated with different inhibitors and then subjected to protease activity measurement in the presence of both 1 μM PMA and inhibitors. For PKC kinase inhibition, HepG2 cells were pre-treated with 1 μM Gö6983 for 1.5h. For ERK 1/2 kinase inhibition, HepG2 cells were exposed to 10 μM Erk inhibitor II FR108204 (ERKi2) for 4h before protease assay. For protease inhibition, HepG2 cells were incubated with 20 μM TAPI2, a broad-spectrum inhibitor against several MMPs and ADAM17, for 4h before measurement. (**A**) Histogram of the normalized AI values for 1-cell wells (n >300 per condition). The inset shows the histogram of the normalized AI values for 0-cell wells. Dark dash lines mark the place where normalized AI value = 2. (**B**) Percentage of 1-cell wells with high normalized AI values (>2). Data for 0-cell wells with high normalized AI values is also shown. DMSO: control vehicle; PMA: stimulation with 1 μM PMA alone; +GO: PKC kinase inhibition along with 1 μM PMA challenge; +ERKi2: Erk kinase inhibition along with 1 μM PMA challenge; +TAPI2: broad-spectrum protease inhibition along with 1 μM PMA stimulation. Error bars represent standard deviation of a triplicate using three different arrays.

To investigate the mechanism of PMA-induced protease activation in HepG2 cells and also to show that the increase in protease activity observed by our assay was indeed a result of authentic biological event rather than artifacts, we pre-treated the cells with inhibitors against different components of signaling pathway and observed the corresponding changes in cell surface protease activity. As shown in Figure 3.4, TAPI2, a broad-spectrum inhibitor against MMP proteases along with ADAM17, reduced the PMA-induced protease activation to the level of empty wells, confirming that the responsible protease in this case belonged to MMP/ADAM family. Additionally, PKC inhibition (Gö6983) clearly suppressed the single-cell protease activity to the level of the DMSO control case, suggesting a causal role of PKC kinases in the signaling network of PMA-mediated ADAM17 protease response. On the contrary, ERK inhibitor only slightly dampened the protease activation (p-value = 0.19, insignificant) and thus ERK kinases were unlikely to be essential for ADAM17 activation in PMA-treated HepG2 cells. Therefore, we confirmed that our system was capable of detecting changes in the extracellular protease activity of single cells upon drug challenge and there were inside-out signaling events through PKC kinases involved in the PMA-induced protease response for HepG2 cells.

3.5.3 Snapshots for Temporal Response of PMA-Mediated Protease Activation

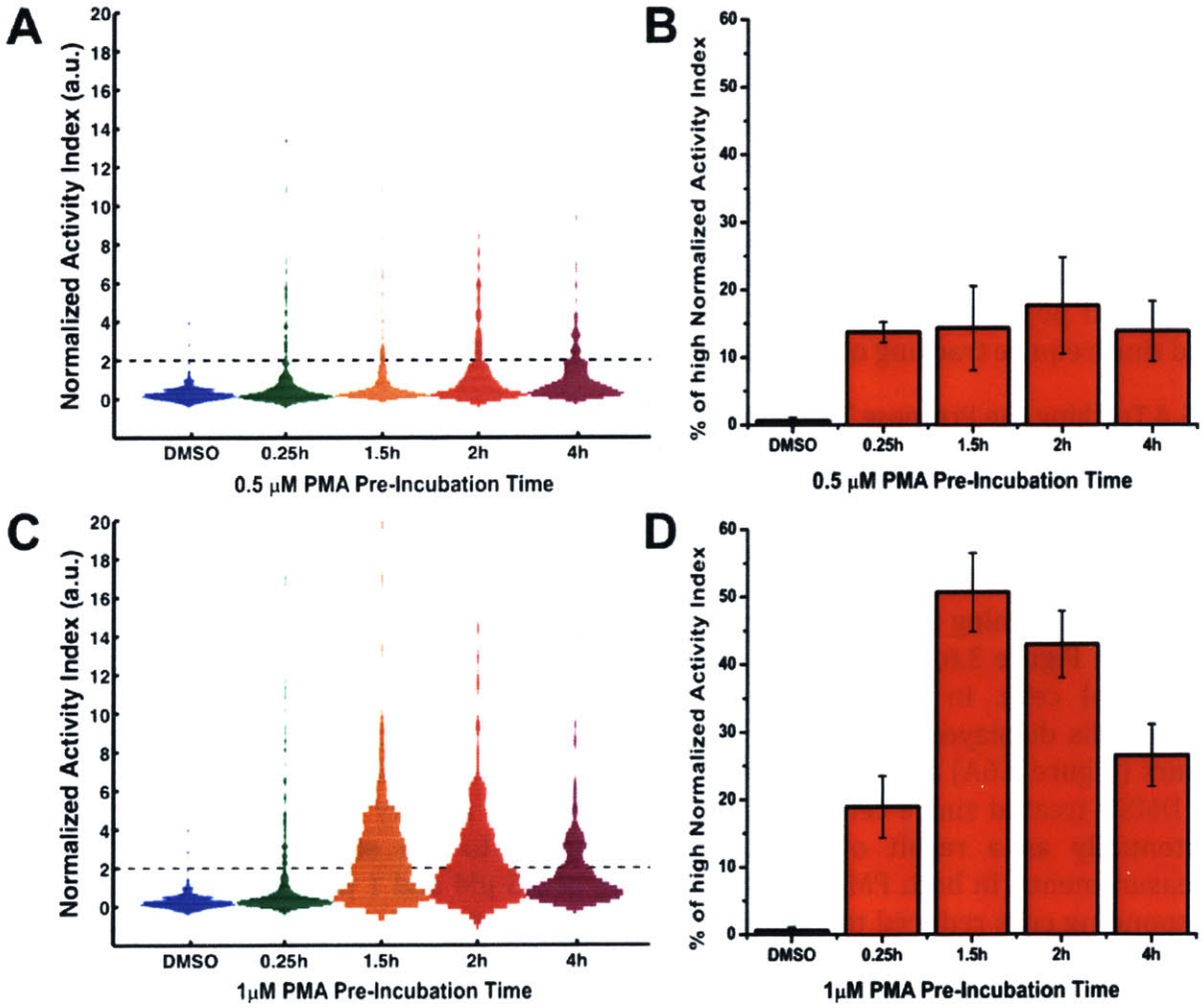

Figure 3.5 Temporal response of the PMA-mediated single-cell protease activity measured in 1-run assay. HepG2 cells were treated with either 0.5 μM (**A, B**) or 1 μM PMA (**C, D**) for various durations (0.25h, 1.5h, 2h, 4h) before subjected to protease activity measurement. Each cell-load arrays were assayed only once. (**A, C**) Histogram of the normalized AI values for 1-cell wells (n >300 per condition). Dark dash lines mark the place where normalized AI value = 2. (**B, D**) Percentage of 1-cell wells with high normalized AI values (>2). Error bars represent standard deviation of a triplicate using three different arrays.

Since it has been long recognized that cells make their decision based on not only the magnitude but also the dynamics of signaling events, we studied the temporal behavior of HepG2 protease response upon PMA challenge. To get the snapshots of protease response, we first performed a single run of protease activity measurement for cells in different microwell arrays with various PMA exposure time. On one hand, for treatment of 0.5 μM PMA (Figure 3.5A, B), we observed a small upward shift in the distribution of 1-cell wells' normalized AI values over time. But the percentage of single cells with very high protease activity (i.e. normalized AI >2) remained relative constant at ~14% for PMA exposure time ranging from 0.25h to 4h. On the other hand, in the case of 1 μM PMA treatment (Figure 3.5C, D), protease activation has extended to the majority of single cells as the PMA exposure time increased. We observed that the percentage of 1-cell wells with high AI values varied with the pre-treatment duration. The percentage of responding cells peaked around ~50% when the pre-treatment time was 1.5h, and decreased to ~26% at pre-treatment time of 4h. Comparing the results under these two different PMA concentrations, we found that stimulant dosage exerted an impact on the response properties of the single-cell population in terms of protease activation dynamics. That is, the lower stimulant dosage ([PMA] = 0.5 μM) generated a low but relatively constant level of protease activity over time, whereas the higher dosage ([PMA] = 1 μM) produced a varying but high protease activity signal among the single-cell population. Reasons for this dose-dependent impact on single-cell population might lie in the time-dependent behavior of individual single cells and thus require tracking of protease response for individual cells over time.

3.5.4 Tracking the Protease Temporal Response of Single Cells

Many cell-signaling and transcriptional process show pulsatile, or even oscillatory, behaviors [24]. Although the physiological significance of such oscillations in these systems is not fully understood, it could be another regulatory layer in which biological information can be encoded. Therefore, we further investigated the temporal behavior of individual cells by performing 3 sequential runs of measurements on the same cell-seeded array. As shown in Figure 3.6, we observed various temporal patterns of the protease response for individual cells. In DMSO control case, the majority (~95%) of the cell-containing microwells displayed low level of protease activity during the entire assay period of 3.2 hours (Figure 3.6A) and there were little changes between runs (Figure 3.6C, E). About 4% of DMSO-treated single cells displayed high protease activity in the 3rd run (Figure 3.6B), potentially as a result of the cellular response to the stress induced by repeated measurements. In both PMA stimulation case of 0.5 μM and 1 μM, the fraction of the non-responding cells reduced to ~60 ± 2% (No. 8 in Figure 3.6E), while 15~20% of single cells exhibited a pulsatile activity profile (initial increase followed by decrease, No. 3 in Figure 3.6E). There were also 8~10% of PMA-treated single cells with a delayed protease

response (No.7 in Figure 3.6E), as they started to show high protease activity signal in the 3rd run of measurement, which corresponded to PMA treatment time: t_{PMA} = 2.5 ~3.2h. The impact of PMA dosage was most evident in the early protease response of single cells. As shown in Figure 3.6B, higher dosage of PMA treatment resulted in more single cells with high activity in the 1st run of measurement. Meanwhile, Figure 3.6E shows that most of these fast-responding cells experienced a decrease in protease activity at 2nd run of measurement and thus fell into the category of dynamic pattern No.5 (3.8% for [PMA]= 0.5 μM vs. 10.2% for [PMA] = 1 μM; p-value = 0.21, insignificant).

Although our assay provided limited time points for each single cell, we could gain a glimpse of how individual cells' protease response might change over time. Firstly, results from both 1-run and 3-run assays support asynchronous yet transient protease response at the single-cell level --- that is, each single cell follows an increase-then-decrease protease activity profile upon PMA challenge. Secondly, higher stimulant concentration seems to favor more cells with earlier onset of protease activation, instead of modulating the maximum level of individual cells' protease activity. A similar behavior has been observed in the well-studied case of single cells' gene expression [53, 54], where DNA enhancers had been demonstrated to augment the activation probability of single cell without affecting the strength of cellular activation at the individual cell level. Lastly, inspired by the insight that analogue dose-response at the population level could be a result of digital behavior of many individual players, we hypothesized that PMA could increase the probability of single cell being turned ON to go through the transient protease activation profile in a dose-dependent manner. Under this assumption, we came up with an explanation for the distinct dynamic properties of single-cell population observed in the 1-run assays. In the case of lower PMA concentration, the probability of single cells being turned ON might be low and thus there would always be enough cells for turning ON as most of the cells haven't gone through the protease activation process. As a result, one could observe a low but relative constant level of protease activity at the population level of single cells, since at any given time point of PMA treatment, there might be a small but relatively constant number of cells being initiated for protease activation. However, in the case of higher PMA concentration, most of the cells could be turned ON at the early stage due to the increased activation probability endowed by the high PMA concentration. This would result in a more synchronous, higher-strength but pulsatile protease activity at the population level. Obviously, higher time resolution measurements are needed to validate our hypothesis. Nevertheless, our microfluidic platform is able to provide unique temporal information of a large number of single cells utilizing the same biosensing modalities and without involving complex intracellular sensor engineering [16]. Thus, the platform could serve as a generic drug-screening step for primary cells from individual patients.

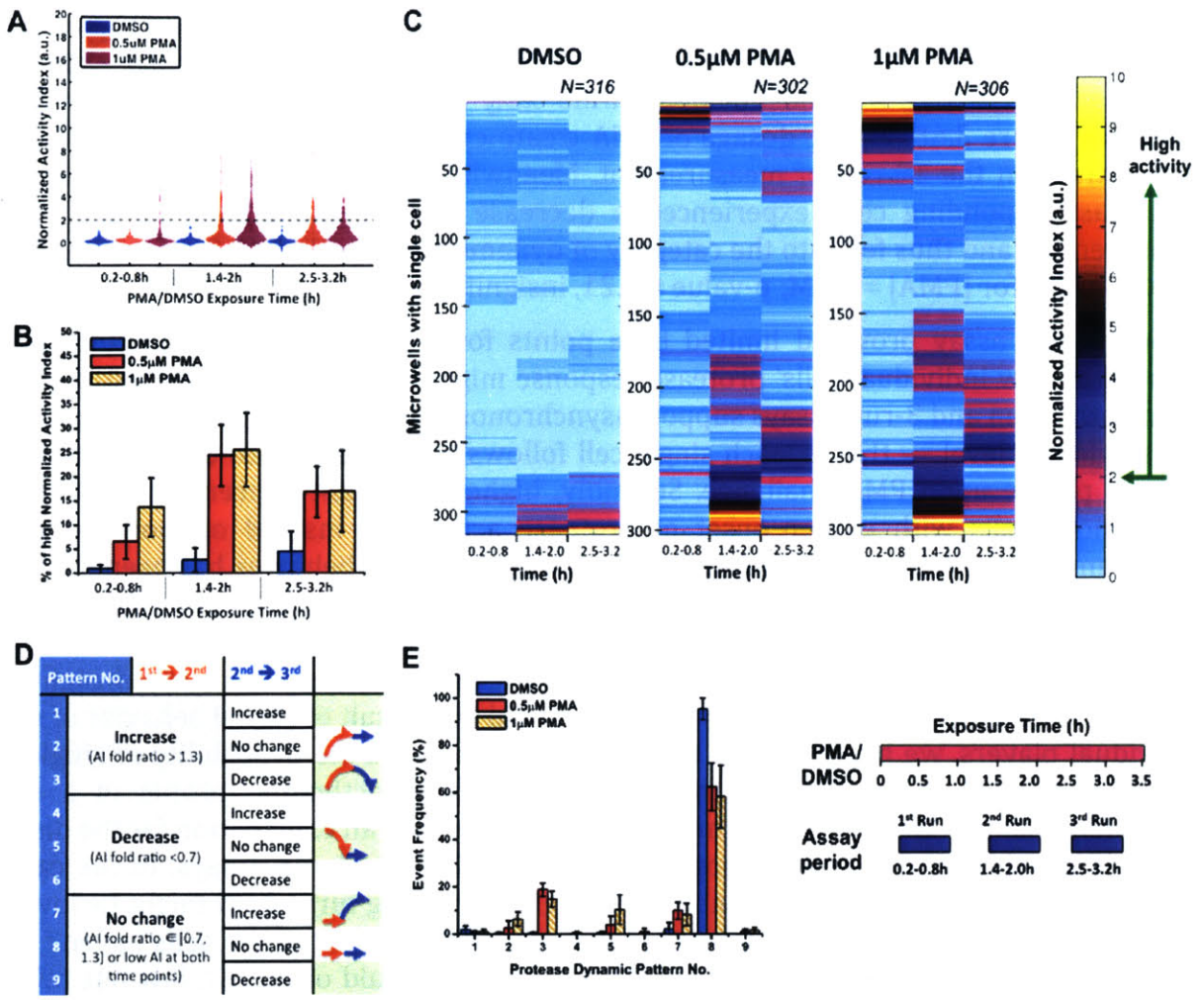

Figure 3.6 Heterogeneous temporal behavior of single-cell protease activity upon PMA challenge. Three sequential runs of protease activity measurement were performed with the same cell-loaded arrays for DMSO control case and PMA stimulation case (0.5 μM or 1 μM PMA), respectively. As illustrated in the experiment schedule shown on the lower right, the DMSO or PMA drug (magenta bar) was applied to cells at constant concentration for the entire experiment. The protease measurements (blue blocks) were conducted in sequential manners and thus corresponded to different drug exposure times. (**A**) Histogram of the normalized AI values for 1-cell wells (n >300 per condition). Dark dash lines mark the place where normalized AI value = 2. (**B**) Percentage of 1-cell wells with high normalized AI values (>2). (**C**) Clustered heat maps for 1-cell wells' normalized AI under different conditions. In each heat map, there are three columns corresponding to the three different time periods of protease measurement and each row represents the protease activity of individual single cells (n >300 per condition). (**E**) Distribution of the single-cell protease activity profile over different dynamic patterns. (**D**) Table for description of each dynamic pattern. Schematic arrowed profiles were also shown for the patterns with more than 5% single cells in at least one of the drug conditions. If the normalized AI values of single cells are less than 2 at both time points or changes in their AI values are less than 30% of the original AI values, we define them as "no change" in protease activity over time. Meanwhile, an "increase" or "decrease" in protease activity is defined for the rest of single cells depending on whether their AI values at the latter time point are 30% larger or smaller than the corresponding AI values at the earlier time point. Error bars represent standard deviation of a triplicate using three different arrays.

3.6 Case Study II: Single-Cell Protease Response of Parental and Gefitinib-Resistant HCC827 Cells

Despite decades of investigation and significant progress in cancer biology, resistance to cancer therapy remains a major challenge in current cancer research. Even in the case of targeted cancer therapies, resistance to anticancer drugs frequently emerges in patients with impressive good initial responses [55]. This resistance issue is particularly evident in the case of non-small cell lung cancer (NSCLC), where specific tyrosine kinase inhibitors (TKIs) are employed in targeted therapies to treat patients harboring relevant genomic abnormalities – often in the gene encoding EGFR. Large-scale clinical studies reported a median progression-free time of about 12 months for lung caner patients with good initial response to TKIs [56, 57]. With a systematic comparison on tumor biopsies of same drug-resistant patients before and after TKI treatment, a recent study discovered newly found secondary mutation in 22 out of 37 patients (59%) and histological transformation in 5 out of 37 patients (14%) [58], which provides some insights for the potential mechanism of the acquired drug resistance. However, 7 out of 37 drug-resistance patients (30%) displayed neither genotypic nor phenotypic alterations, emphasizing the needs in fully characterizing cellular states to elucidate currently unknown mechanisms of drug resistance. As mentioned in section 3.1.1, pericelluar proteases, ADAMs in particular, could have dual role in resistance development against cancer therapies. Depending on the context, including the shedding of growth factor ligands or receptors and the responsiveness of compensatory kinase signaling pathway, the activities of ADAMs could either exaggerate or mitigate the disease progression [10, 11, 59]. Single-cell study on protease activity will help to elucidate the role of protease and microenvironment in resistance development.

In this case study II, we use HCC827, a NSCLC cell line, as model experimental system. Parental HCC827 cells harbor mutation in EGFR and are sensitive to TKI treatment using gefitinib. It has been reported that rare cells with MET amplification could be found in the parental cell population prior to TKI treatment and got enriched through a 2-stage selection process at the presence of gefitinib [35]. The resulting cell line, termed gefitinib-resistant HCC827 cells, maintain the MET amplification and exhibit lack of sensitivity to gefitinib-induced cell death at bulk level. In this section, we seek to exanimate the single-cell protease activity profile for parental and resistant HCC827 cells. Further single-cell measurements along the time course of resistance development process might help to elucidate the evolution of protease profile and its role in mechanism of drug resistance.

3.6.1 Discrepancy Between Bulk Profile and Single-Cell Profile

We first measured the protease activity of parental (P) and gefitinib-resistant (GR) HCC827 cells at bulk level using plate reader. As shown in Figure 3.7A, both parental and resistant cells displayed a very weak increase in bulk ADAM17 protease activity upon 1 μM gefitinib treatment (insignificant). The gefitinib-treated parental cells exhibited much higher protease activity than DMSO- and gefitinib-treated resistant cells (p-value <0.001, significant). We then performed 1-run protease assay using our microwell platform on parental and resistant HCC827 cells at both basal (DMSO) and drug-treated (Gef) conditions. As shown in Figure 3.7B-E, we observed an upward shift in the distribution of microwell protease activity as cell number per well increased, indicating a relationship

between cell number and protease activity. In the case of 3-cell and 4-cell microwells, majority of microwells displayed normalized protease activity index higher than detection threshold (>1, Figure 3.7F). However, no statistically significant difference was found between each condition, suggesting similar protease activity level for parental and resistant HCC827 cells. Moreover, to examine the gefitinib-induced protease response, we further performed 2-run protease assay on the same cell-loaded array using the microfluidic platform (Figure 3.8). The basal ADAM17 activities of cells were measured in the 1st run at the presence of DMSO control, while the drug-treated protease activities of same cells were measured in the 2nd run along with gefitinib. As shown in Figure 3.8, majority of cell-loaded microwells displayed no apparent change in their protease activity upon 1 μM-gefitinib challenge. Treatment with increased gefitinib dosage (10 μM) induced no statistical significant changes in the ADAM17 activities of parental cells, either. Taken together, the results from microwell assay suggest no obvious protease activity difference between parental and resistant HCC827 cells, in terms of both basal activity and the gefitinib-induced protease response. This is contradictory to the bulk assay's results where the gefitinib-treated parental cells displayed higher activity than resistant cells.

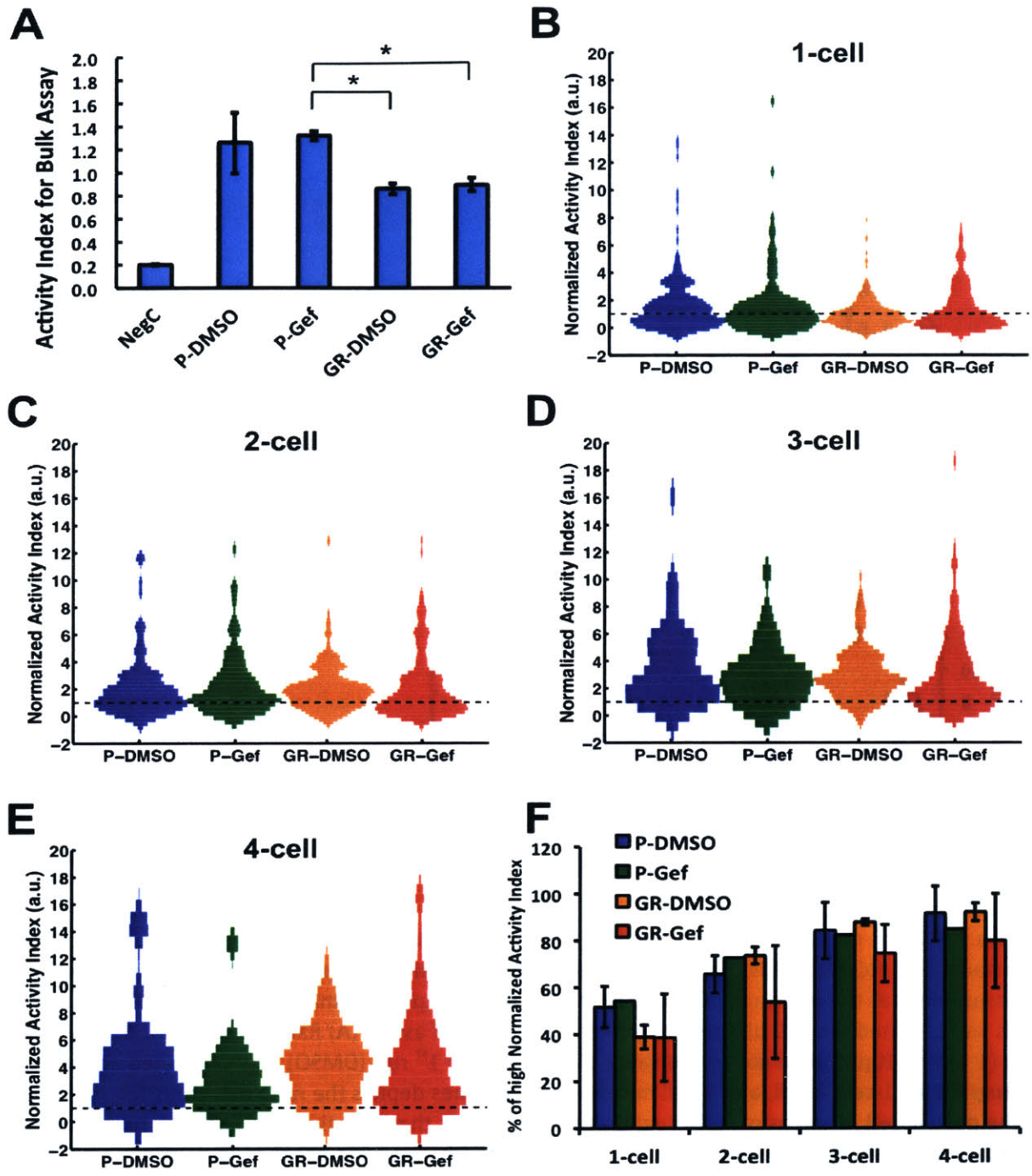

Figure 3.7 1-run measurements on ADAM17 protease activity of parental (P) and resistant (GR) HCC827 cells at basal (DMSO) or 1 μM gefitinib-treated (Gef) condition. (**A**) Protease activity measured at bulk level using plate reader. NegC: negative control for wells seeded without cells but treated with DMSO. Error bars represent standard deviation of a triplicate bulk assay. (**B-F**) Protease activity measured using microwell platform. Histograms of normalized activity index (NAI) are shown for microwells of 1-cell (**B**, n >200 per condition), 2-cell (**C**, n >150 per condition), 3-cell (**D**, n >100 per condition), 4-cell (**E**, n >50 per condition). Based on 0-cell's NAI distribution, the threshold for high activity microwells is defined as NAI = 1 and marked as dash line in each plot. (**F**) Percentage of high activity microwells (>1) for microwells with 1~4 cells. Error bars depict standard deviation of a duplicate using two different arrays.

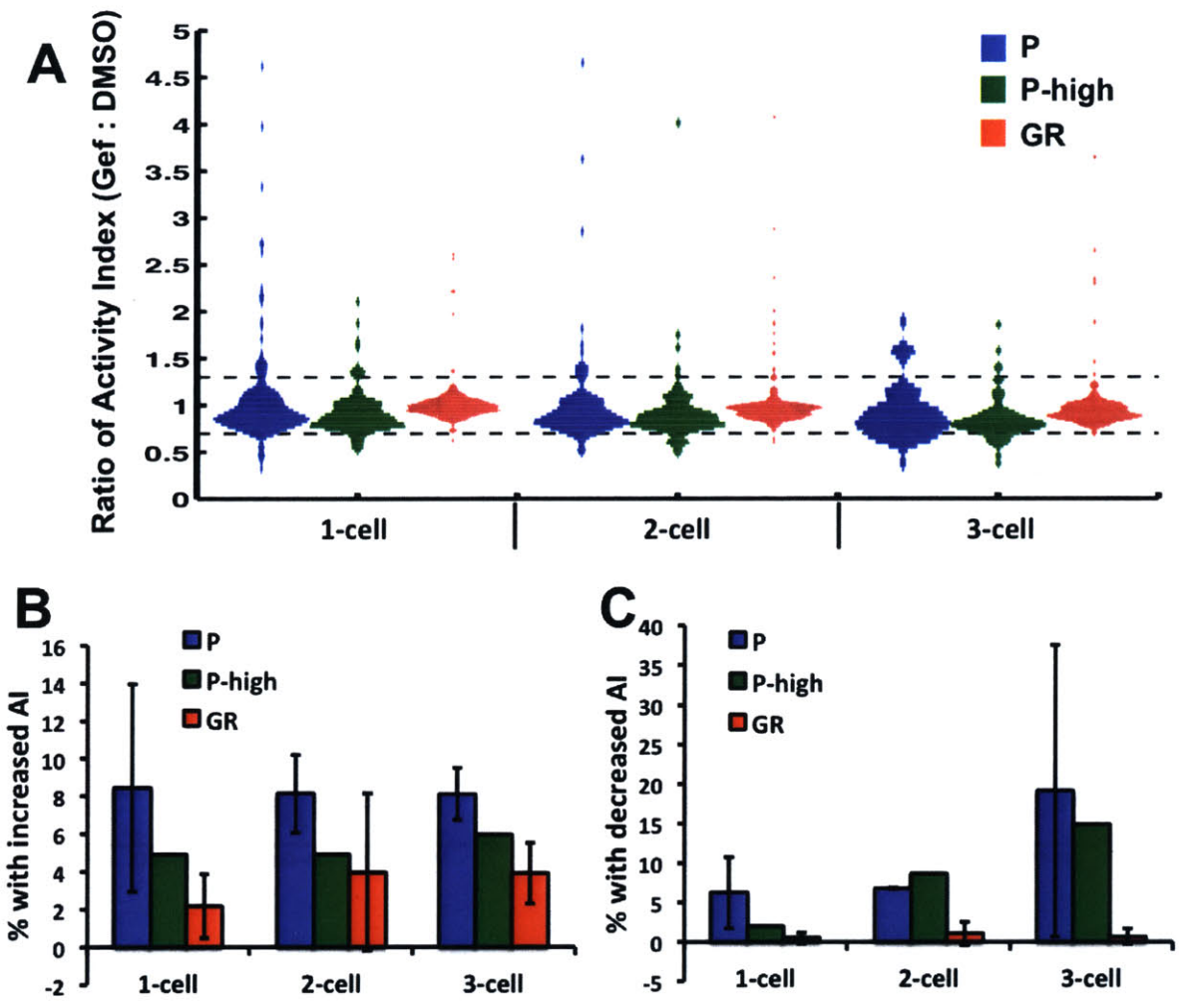

Figure 3.8 2-run measurements on gefitinib-mediated ADAM17 protease response of parental (P) and resistant (GR) HCC827 cells. Same cell-loaded microwell arrays were subjected to protease activity measurement at the presence of DMSO in the 1st run and 1μM gefitinib in the 2nd run. P-high: Parental cells were treated with 10 μM gefitinib instead in 2nd run of assay. (**A**) Ratio of activity index value in 2nd run (1 μM or 10μM gefitinib) to the value of same cell in 1st run (DMSO) was calculated and shown as histogram for 1-cell, 2-cell, and 3-cell microwells. Dash lines depicts the ratio = 0.7 and 1.3, respectively. If the normalized AI values of individual microwells are less than threshold (=1) at both runs of assays or ratios in their AI values are within [0.7, 1.3], we define them as "no change" in protease activity upon drug treatment. Meanwhile, an "increase" (**B**) or "decrease" (**C**) in protease activity is defined for the rest of cell-loaded microwells depending on whether their AI values upon gefitinib challenge (2nd run) are 30% larger or smaller than the corresponding AI values at basal line (1st run). Error bars represent standard deviation of a duplicate using two different arrays.

It's unclear why protease response at few-cell level is different from that at bulk level. One potential explanation involves the uncontrolled cell death present in bulk assay. In general, cells undergoing cell death exhibit very high protease activity level during the assay. In microwell assay, only cells remaining alive on the 2nd day of assay were considered for data analysis. Whereas, in bulk assay, live cells were mixed with dead and dying cells, resulting

in an overestimation on the protease activity level. Moreover, parental HCC827 cells display lower viability than resistant cells at both basal and gefitinib-treated conditions during culture. Thus, the higher protease activity observed in bulk gefitinib-treated parental cells might directly arise from the more dead and dying cells present in sample. Besides, the cell-cell communication might also play a role in the discrepancy between bulk assay result and microwell assay result. Dying cells in culture shed away vesicles containing various molecules inside or on the membrane surfaces. Those vesicles could interact with live cells and modulate their cellular response. While dying cells could communicate with neighboring live cells freely in bulk assay, those communications are excluded from microwell assay due to the compartmentalization.

3.7 Conclusions and Future directions

3.7.1 Section Summary

In this chapter, we develop a microfluidic platform for single-cell study of pericellular protease activity. In contrast to existing methodologies for single-cell pericellular protease measurement, we constrain the fluorescence readout of protease activity to individual cells by physical isolation of cells within each microwells using a pneumatically actuated lid. Due to the simplicity of our design, our platform works with various small molecule FRET-based protease substrates and is able to measure single-cell protease activity with meaningful time resolution (~1.2h).

In case study I, we apply the developed platform to study the PMA-induced single-cell protease response of HepG2 cells and show, for the first time, that the extracellular protease activity of individual cells displays diverse dynamic patterns despite the overall trend of population cell response during the same period. Moreover, our platform is compatible with many existing single-cell analysis methods probing other molecular events of single cells. A typical example would be to combine our platform for protease activity measurement with the micro-engraving method for molecular shedding from the cell surface. This combination of techniques is particularly valued in the study of protease-mediated cancer resistance development. Our platform therefore has the potential for studying the context-dependent role of pericellular protease activities in governing cell behaviors.

In case study II, we present the preliminary exploration of single-cell protease activity behavior in anti-cancer drug resistance development. While the bulk assay result suggests higher gefitinib-induced protease activity for parental HCC827 cells, the microwell assay result indicates no significant difference among the protease behavior of parental and resistant HCC827 at few-cell level. The discrepancy between bulk assay's and microwell assay's results might arise from the uncontrolled cell death present in bulk assay as well as the molecular communication between live cells and dying cells. Thus, further study on protease response of parental and resistant HCC827 cells should consider the effect of cell death on cellular behavior.

3.7.2 Future Directions

There are some on-going works in our lab utilizing the single-cell protease activity

measurement platform.

One work is to investigate the neutrophil protease behavior under different conditions. Although people have long recognized the heterogeneity among the circulating neutrophils, it remains to be seen whether the heterogeneity also exists in the aspect of cellular protease activity and if yes, what causes and consequences might be. In this project, size-based cell sorter developed in Chapter 2 are first used to isolate neutrophils gently from blood sample and then the microfluidic platform developed in Chapter 3 is used to measure the single-cell protease profile. Using healthy human blood sample, the microfluidic platform revealed subtle increase of ADAM17 protease activity in ~30% neutrophils upon 0.1 μM PMA treatment, which in in agreement with the corresponding bulk assay's results. Further investigation on single-cell protease profile of neutrophils from different patient samples might help to study the role of neutrophil protease in disease progression.

Another work involves the investigation on the role of protease in distant metastasis. Circulating tumor cells (CTCs), which have been shed into blood stream by a primary tumor, have been believed to be the seed for the generation of secondary tumors (metastasis) in distant organs. Due to the rarity of CTCs in blood (2~5 CTCs per 7.5 mL blood), single-cell analysis becomes an invaluable approach to get rich information from the limited amount of CTCs isolated from patient sample. With the help of size-based cell sorter developed in Chapter 2, we would harvest CTCs at high recovery from patient sample and then expand the viable retrieved CTCs during *in vitro* culture. Downstream analysis, including the single-cell protease activity measurement using our platform, would then be performed on the retrieved CTCs during the time course of *in vitro* colonization. It's hypothesized that during this time course, viable CTCs would have to change their functional state from a relative unresponsive mode – suitable for their peripheral blood circulation – to an active mode enabling their functionalities during late stages of metastasis process, including the abilities to attach extracellular matrix, to infiltrate the stromal cells and to form colonies. The evolution of single-cell protease activity profile during this time course would shed light on the different roles of those proteases at different stages of distant metastasis.

3.8 Section Acknowledgements

This work was supported by the Singapore-MIT Alliance for Research and Technology (SMART) Centre (BioSym IRG). This work was also supported by NIH Grant R01-CA096504. The author would like to thank Ms. Wei Qiu, who designed the cover art for the publication on case study I in this chapter.

3.9 References

[1] Arribas, J. and Esselens, C., *ADAM17 as a Therapeutic Target in Multiple Diseases.* Current Pharmaceutical Design, 2009. **15**(20): p. 2319-2335.

[2] Duffy, M.J., McKiernan, E., O'Donovan, N., and McGowan, P.M., *The role of ADAMs in disease pathophysiology.* Clinica Chimica Acta, 2009. **403**(1–2): p. 31-36.

[3] Michael, J.D., et al., *The ADAMs family of proteases: new biomarkers and therapeutic targets for cancer?* Clinical Proteomics, 2011. **8**(1): p. 9-9.

[4] Blobel, C.P., *ADAMs: key components in EGFR signalling and development.* Nat Rev Mol Cell Biol, 2005. **6**(1): p. 32-43.
[5] Kessenbrock, K., Plaks, V., and Werb, Z., *Matrix Metalloproteinases: Regulators of the Tumor Microenvironment.* Cell, 2010. **141**(1): p. 52-67.
[6] Gooz, M., *ADAM-17: the enzyme that does it all.* Critical Reviews in Biochemistry and Molecular Biology, 2010. **45**(2): p. 146-169.
[7] Murphy, G., *The ADAMs: signalling scissors in the tumour microenvironment.* Nat Rev Cancer, 2008. **8**(12): p. 932-941.
[8] McGowan, P.M., et al., *ADAM-17 Expression in Breast Cancer Correlates with Variables of Tumor Progression.* Clinical Cancer Research, 2007. **13**(8): p. 2335-2343.
[9] Gargi, M., Wiley, H.S., and Douglas, A.L., *Autocrine epidermal growth factor signaling stimulates directionally persistent mammary epithelial cell migration.* The Journal of Cell Biology, 2001. **155**(7).
[10] Zhou, B.-B.S., et al., *Targeting ADAM-mediated ligand cleavage to inhibit HER3 and EGFR pathways in non-small cell lung cancer.* Cancer Cell, 2006. **10**(1): p. 39-50.
[11] Miller, M.A., et al., *ADAM-10 and -17 regulate endometriotic cell migration via concerted ligand and receptor shedding feedback on kinase signaling.* Proceedings of the National Academy of Sciences, 2013. **110**(22): p. E2074-E2083.
[12] Horiuchi, K., et al., *Substrate Selectivity of Epidermal Growth Factor-Receptor Ligand Sheddases and their Regulation by Phorbol Esters and Calcium Influx.* Molecular Biology of the Cell, 2007. **18**(1): p. 176-188.
[13] Pillinger, M.H., et al., *Matrix Metalloproteinase Secretion by Gastric Epithelial Cells Is Regulated by E Prostaglandins and MAPKs.* Journal of Biological Chemistry, 2005. **280**(11): p. 9973-9979.
[14] Xu, P. and Derynck, R., *Direct Activation of TACE-Mediated Ectodomain Shedding by p38 MAP Kinase Regulates EGF Receptor-Dependent Cell Proliferation.* Molecular Cell, 2010. **37**(4): p. 551-566.
[15] Chen, C.-H., et al., *Multiplexed Protease Activity Assay for Low-Volume Clinical Samples Using Droplet-Based Microfluidics and Its Application to Endometriosis.* Journal of the American Chemical Society, 2012. **135**(5): p. 1645-1648.
[16] Hobson, J.P., Liu, S., Leppla, S., and Bugge, T., *Imaging Specific Cell Surface Protease Activity in Living Cells Using Reengineered Bacterial Cytotoxins*, in *Proteases and Cancer*, T.H. Bugge and T.M. Antalis, Editors. 2009, Humana Press. p. 115-129.
[17] McIntyre, J.O. and Matrisian, L., *Optical Proteolytic Beacons for In Vivo Detection of Matrix Metalloproteinase Activity*, in *Proteases and Cancer*, T.H. Bugge and T.M. Antalis, Editors. 2009, Humana Press. p. 155-174.
[18] McIntyre, J.O., et al., *Development of a novel fluorogenic proteolytic beacon for in vivo detection and imaging of tumour-associated matrix metalloproteinase-7 activity.* Biochem. J., 2004. **377**(3): p. 617-628.
[19] Jiang, T., et al., *Tumor imaging by means of proteolytic activation of cell-penetrating peptides.* Proceedings of the National Academy of Sciences of the United States of America, 2004. **101**(51): p. 17867-17872.
[20] Sloane, B.F., Sameni, M., Podgorski, I., Cavallo-Medved, D., and Moin, K., *Functional Imaging of Tumor Proteolysis.* Annual Review of Pharmacology and Toxicology, 2006. **46**(1): p. 301-315.

[21] Moin, K., et al., *Chapter ten - 3D/4D Functional Imaging of Tumor-Associated Proteolysis: Impact of Microenvironment*, in *Methods in Enzymology*, P.M. Conn, Editor. 2012, Academic Press. p. 175-194.
[22] Wolf, K. and Friedl, P., *Functional imaging of pericellular proteolysis in cancer cell invasion.* Biochimie, 2005. **87**(3–4): p. 315-320.
[23] Martin, R.M., Leonhardt, H., and Cardoso, M.C., *DNA labeling in living cells.* Cytometry Part A, 2005. **67A**(1): p. 45-52.
[24] Spiller, D.G., Wood, C.D., Rand, D.A., and White, M.R.H., *Measurement of single-cell dynamics.* Nature, 2010. **465**(7299): p. 736-745.
[25] Primiceri, E., Chiriaco, M.S., Rinaldi, R., and Maruccio, G., *Cell chips as new tools for cell biology - results, perspectives and opportunities.* Lab on a Chip, 2013. **13**(19): p. 3789-3802.
[26] Meyvantsson, I. and Beebe, D.J., *Cell Culture Models in Microfluidic Systems.* Annual Review of Analytical Chemistry, 2008. **1**(1): p. 423-449.
[27] Yin, H. and Marshall, D., *Microfluidics for single cell analysis.* Current Opinion in Biotechnology, 2012. **23**(1): p. 110-119.
[28] Zheng, Y., Nguyen, J., Wei, Y., and Sun, Y., *Recent advances in microfluidic techniques for single-cell biophysical characterization.* Lab on a Chip, 2013. **13**(13): p. 2464-2483.
[29] Ochsner, M., et al., *Micro-well arrays for 3D shape control and high resolution analysis of single cells.* Lab on a Chip, 2007. **7**(8): p. 1074-1077.
[30] Charnley, M., Textor, M., Khademhosseini, A., and Lutolf, M.P., *Integration column: microwell arrays for mammalian cell culture.* Integrative Biology, 2009. **1**(11-12): p. 625-634.
[31] Love, J.C., Ronan, J.L., Grotenbreg, G.M., van der Veen, A.G., and Ploegh, H.L., *A microengraving method for rapid selection of single cells producing antigen-specific antibodies.* Nat Biotech, 2006. **24**(6): p. 703-707.
[32] Ma, C., et al., *A clinical microchip for evaluation of single immune cells reveals high functional heterogeneity in phenotypically similar T cells.* Nat Med, 2011. **17**(6): p. 738-743.
[33] Unger, M.A., Chou, H.-P., Thorsen, T., Scherer, A., and Quake, S.R., *Monolithic Microfabricated Valves and Pumps by Multilayer Soft Lithography.* Science, 2000. **288**(5463): p. 113-116.
[34] Miller, M.A., et al., *Proteolytic Activity Matrix Analysis (PrAMA) for simultaneous determination of multiple protease activities.* Integrative Biology, 2011. **3**(4): p. 422-438.
[35] Turke, A.B., et al., *Pre-existence and clonal selection of MET amplification in EGFR mutant NSCLC.* Cancer cell, 2010. **17**(1): p. 77-88.
[36] Marshall, C.J., *Specificity of receptor tyrosine kinase signaling: Transient versus sustained extracellular signal-regulated kinase activation.* Cell, 1995. **80**(2): p. 179-185.
[37] Shymko, R.M., De Meyts, P., and Thomas, R., *Logical analysis of timing-dependent receptor signalling specificity: application to the insulin receptor metabolic and mitogenic signalling pathways.* Biochem. J., 1997. **326**(2): p. 463-469.

[38] Dertinger, S.K.W., Chiu, D.T., Jeon, N.L., and Whitesides, G.M., *Generation of Gradients Having Complex Shapes Using Microfluidic Networks.* Analytical Chemistry, 2001. **73**(6): p. 1240-1246.

[39] Parkin, D.M., Bray, F., Ferlay, J., and Pisani, P., *Global Cancer Statistics, 2002.* CA: A Cancer Journal for Clinicians, 2005. **55**(2): p. 74-108.

[40] Hoshida, Y., et al., *Gene Expression in Fixed Tissues and Outcome in Hepatocellular Carcinoma.* New England Journal of Medicine, 2008. **359**(19): p. 1995-2004.

[41] Berasain, C., et al., *Epidermal growth factor receptor signaling in hepatocellular carcinoma: inflammatory activation and a new intracellular regulatory mechanism.* Digestive diseases (Basel, Switzerland), 2012. **30**(5): p. 524-531.

[42] Chalupsky, K., et al., *ADAM10/17-Dependent Release of Soluble C-Met Correlates with Hepatocellular Damage.* Folia Biologica, 2013. **59**(2): p. 76-86.

[43] Gentry, L.E., Chaffin, K.E., Shoyab, M., and Purchio, A.F., *Novel serine phosphorylation of pp60c-src in intact cells after tumor promoter treatment.* Molecular and cellular biology, 1986. **6**(2): p. 735-738.

[44] Jacobs, S., Sahyoun, N.E., Saltiel, A.R., and Cuatrecasas, P., *Phorbol esters stimulate the phosphorylation of receptors for insulin and somatomedin C.* Proceedings of the National Academy of Sciences of the United States of America, 1983. **80**(20): p. 6211-6213.

[45] Driedger, P.E. and Blumberg, P.M., *Specific binding of phorbol ester tumor promoters.* Proceedings of the National Academy of Sciences of the United States of America, 1980. **77**(1): p. 567-571.

[46] Le Gall, S.M., et al., *ADAM17 is regulated by a rapid and reversible mechanism that controls access to its catalytic site.* Journal of Cell Science, 2010. **123**(22): p. 3913-3922.

[47] Blumberg, P.M., *Protein Kinase C as the Receptor for the Phorbol Ester Tumor Promoters: Sixth Rhoads Memorial Award Lecture.* Cancer Research, 1988. **48**(1): p. 1-8.

[48] Dang, M., et al., *Regulated ADAM17-dependent EGF family ligand release by substrate-selecting signaling pathways.* Proceedings of the National Academy of Sciences, 2013.

[49] Puente, L.G., He, J.-S., and Ostergaard, H.L., *A novel PKC regulates ERK activation and degranulation of cytotoxic T lymphocytes: Plasticity in PKC regulation of ERK.* European Journal of Immunology, 2006. **36**(4): p. 1009-1018.

[50] Soond, S.M., Everson, B., Riches, D.W.H., and Murphy, G., *ERK-mediated phosphorylation of Thr735 in TNF α-converting enzyme and its potential role in TACE protein trafficking.* Journal of Cell Science, 2005. **118**(11): p. 2371-2380.

[51] Doedens, J.R., Mahimkar, R.M., and Black, R.A., *TACE/ADAM-17 enzymatic activity is increased in response to cellular stimulation.* Biochemical and Biophysical Research Communications, 2003. **308**(2): p. 331-338.

[52] Reddy, P., et al., *Functional Analysis of the Domain Structure of Tumor Necrosis Factor- α Converting Enzyme.* Journal of Biological Chemistry, 2000. **275**(19): p. 14608-14614.

[53] Larson, D.R., et al., *Direct observation of frequency modulated transcription in single cells using light activation.* eLife, 2013. **2**: p. e00750.

[54] Walters, M.C., et al., *Enhancers increase the probability but not the level of gene expression.* Proceedings of the National Academy of Sciences, 1995. **92**(15): p. 7125-7129.
[55] Holohan, C., Van Schaeybroeck, S., Longley, D.B., and Johnston, P.G., *Cancer drug resistance: an evolving paradigm.* Nat Rev Cancer, 2013. **13**(10): p. 714-726.
[56] Mok, T.S., et al., *Gefitinib or Carboplatin–Paclitaxel in Pulmonary Adenocarcinoma.* New England Journal of Medicine, 2009. **361**(10): p. 947-957.
[57] Rosell, R., et al., *Screening for Epidermal Growth Factor Receptor Mutations in Lung Cancer.* New England Journal of Medicine, 2009. **361**(10): p. 958-967.
[58] Sequist, L.V., et al., *Genotypic and Histological Evolution of Lung Cancers Acquiring Resistance to EGFR Inhibitors.* Science Translational Medicine, 2011. **3**(75): p. 75ra26-75ra26.
[59] Van Schaeybroeck, S., et al., *ADAM17-Dependent c-MET-STAT3 Signaling Mediates Resistance to MEK Inhibitors in KRAS Mutant Colorectal Cancer.* Cell Reports, 2014. **7**(6): p. 1940-1955.

Chapter 4 Theoretical Limits in Single-Cell Shedding Detection

4.1 Introduction

Besides the activity to degrade extracellular matrices, another critical aspect of protease's role in regulating cellular microenvironment is via molecular shedding. As mentioned in section 3.1.1, depending on the identity of protease substrates and the extent to which the proteases shed away cell-surface molecules, pericellular proteases could impact cellular behavior through either positive or negative feedback. Thus, measuring molecular shedding at single-cell level is crucial for studying the mechanistic role of proteases in cell fate decision. Moreover, the protease-mediated shedding rate of cell surface molecules, c-Met in particular, has been shown to correlate with the malignant potential for a variety of human cancers [1], further suggesting the need in analyzing molecular shedding for single-cell study of cancer research. Therefore, this chapter of the thesis is devoted to the experimental and numerical study of the detection of shed molecules from a single cell, confined in microwells. In this work, we chose the strategy of confining antibody-coated beads from standard Luminex assay with single cells under study in same microwells. Compared with antibody immobilization method on the wall of the device (i.e. the microengraving technique) [2, 3], this provides better control over surface immobilization of antibodies and easier validation using Luminex system or flow cytometer.

Similar to cytokine secretion and antibody production, protease-mediated molecular shedding results in soluble molecules released from cell surface. Immunosandwich assays against these secreted or shed molecules from single cells are challenging due to the low abundance of targets, and therefore are frequently coupled with small microfluidics chambers, microwells or even droplets that are loaded with cells, to enhance the quantitative measurement of single-cell secretion or shedding, as the idea of microfluidic confinement to enhance detection sensitivity has been widely known previously [4, 5]. Those single-cell immunosandwich assays are usually performed in two formats. One is the open array format with cells in open environment and capture agent in close proximity [6, 7]. The other is the closed array format with both cells and capture agent confined in closed space [2, 3]. Using numerical simulations of a deterministic continuum model, a recent paper [8] compared the assay performance of these two formats in the regime of single-cell antibody production (generation rate, k_g = 500~2000 molecules/cell/sec [9, 10]) and cytokine secretion (k_g = 5~50 molecules/cell/sec [2]). Based on the simulations, open array format would bias the detection towards cells with high secretion rate, whereas the closed array format provides a greater dynamic range that is more suitable for quantitative analysis on a wide range of single-cell secretion rates. Therefore, it is tempting to directly apply the closed array format of single-cell immunosandwich assay to measure the molecular shedding of individual cells. However, molecular shedding of interest in cancer research usually occurs at a generation rate that is 1~2 orders of magnitude lower than the cytokine secretion rate of immune cells. For example, the c-Met shedding rate of cultured breast tumor cells has been established to be 0.02~1.04 molecules/cell/sec [1], which would result in only a few thousands of target molecules available for detection after hours of incubation. Molecular binding of such low-abundance target molecules, in a confined,

microfluidic reaction chamber, raises important question about how far one can push the confinement-based detection idea, until it hits the limit posed by the low abundance. In addition, the stochastic nature of molecular diffusion and reaction process in such low abundance limits could result in significant variation in the final output of immunosandwich assay for the exact same target molecule concentration, compromising the accuracy of detection and challenging the conventional way of data interpretation. A careful characterization on the affinity-based molecular capture in relevant concentration ranges would be helpful to properly guide the upstream design and downstream analysis of single-cell shedding measurement that based on immunosandwich assays.

In this chapter, we couple our microwell array platform developed in Chapter 3 with Luminex assay using antibody-coated microbeads to detect the c-Met shedding of single parental HCC827 cells. Using it as an experimental system, we perform critical analysis on the theoretic limits in detection uncertainty for the closed-array immunosandwich assay. Then, we establish both deterministic continuum model and stochastic discrete model to numerically simulate the molecular capture in this type of assay and characterize the impact of stochastic events in assay performance as a function of capture agent affinity, amount and spatial distribution, microwell size, and the abundance of target molecules. Lastly, we present the experimental data for the closed-array immunosandwich assay using our platform and discuss the practical factors impacting the detection sensitivity and uncertainty.

4.2 Materials and Methods

Methods for device fabrication, cell culture, and device assembly and operation are the same as described in section 3.3.1, 3.3.2, 3.3.3, respectively.

4.2.1 Numerical Modeling of Antibody-based Molecular Capture in Confined Space

For simplicity, symbols for molecules listed in this chapter are written in upper-case letters, such as R (Receptors) for the unoccupied antibodies immobilized on bead surface, L (free Ligands) for the freely diffusing target analytes in solution, and C (Complexes) for the analyte-antibody complexes formed on bead surface. We use lower-case letters for the total number of molecules present in the entire system. Thus, l, r and c refer to the total molecular number of target analytes, unoccupied binding sites and bound complexes within the closed microwell, respectively. The concentrations of individual molecule specie, in terms of molecule number per unit volume or area, are written in upper-case letters inside square brackets, such as $[L]$ for the volume concentration of free target analytes in solution, $[R]$ and $[C]$ for the surface concentrations of unoccupied binding site and bound complexes, respectively. We also use k for rate constants of reactions, t for the time after closing microwell, $\mathbf{n}$ for the normal vector of a surface (pointing inside the bead/cell surface).

We built models for microwells with two different dimensions. The large microwells have the same dimension ($100\ \mu m \times 100\ \mu m \times 189\ \mu m$ a) used in protease activity study in Chapter 3, and are better suited for adherent mammalian cells with large spreading area and active locomotion. The small microwells are cuboids with dimension of $50\ \mu m \times 50\ \mu m \times 50\ \mu m$ and are suitable for analysis on non-adherent cells or cells with limited

spreading. Notice that there were ~5% variation in the depth of actual microwells due to fabrication artifacts.

We modeled the walls of microwell as impermeable to molecules in the system. As the actual material made of microwells in experiments, PDMS is permeable to small hydrophobic molecules (e.g. steroid hormones) [11] and certain gases (e.g. oxygen and carbon dioxide) [12], but is impermeable to most of peptides, proteins and small hydrophilic molecules [13]. Our target molecules are the shed protein fragments and thus have negligible permeability into PDMS walls.

Besides, we neglected the non-specific binding of target analytes to microwell surfaces. The non-specific binding usually occurs with equilibrium dissociation constant, K_d, in milimolar range, which is much larger than the K_d of antibody-mediated specific analyte capture in our system ($K_d = 0.1\sim10\,nM$). Moreover, in the actual experiments, the microwell surfaces are typically blocked with BSA before the addition of target analytes. Also, both the complete medium for cell culture and the serum-free medium used for assay contains bovine serum (1~10%). As a result, highly abundant serum albumin proteins greatly outnumber the specific target analytes and one could expect prevalent absorption of serum albumin proteins onto the microwell surface, which would minimize the non-specific binding of our target analytes by blocking the surfaces of microwell.

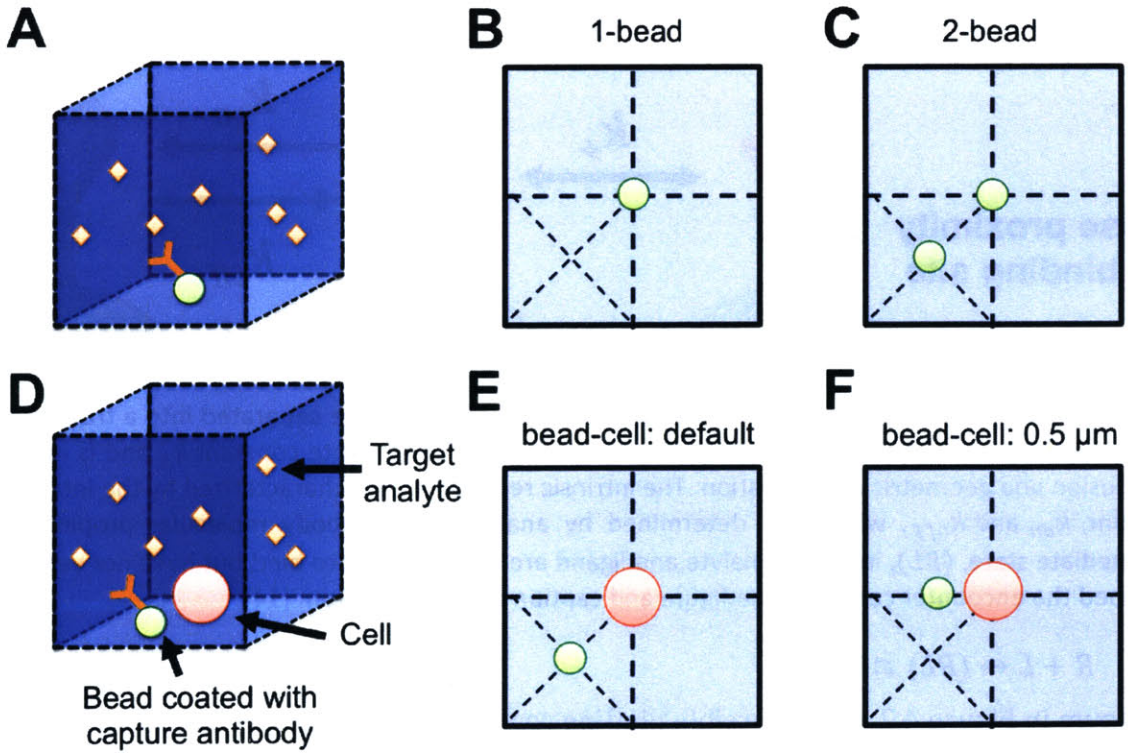

Figure 4.1 Schematic (not to scale) of the closed-array antibody-based analyte capture for (**A, B, C**) external source of target analytes and (**D, E, F**) cellular source of target analytes. (**B, C, E, F**) Top-down views of bottom surface of microwell are shown to depict the positions of antibody-coated bead and analyte-releasing cell under different simulation conditions. Dash lines within each top-down schematic represent the centerlines and diagonals of bottom microwell surface and its quadrant, respectively.

The kinetic models of the antibody-based molecular capture in confined space were established for target molecules generated from two sources: external source and cellular source. In the case of external source (Figure 4.1A, B, C), known amount of target molecules (l_0) are loaded into the closed microwell at $t = 0$, mimicking the scenario of assaying on standard concentration of target molecules. In the case of cellular source (Figure 4.1D, E, F), a 15 μm-diameter sphere located at the bottom center of the closed microwell is modeled as a cell constantly releasing target molecule at a given rate (k_g: molecules/cell/sec), mimicking the scenario of assays on single cell. The cell diameter is chosen to match the size of human cancer cells. Despite the fact that the shedding rate of a live cell likely changes over time as a result of both external environment factors and internal cellular events, we assume a constant shedding rate over time to evaluate the overall molecular capture during the time course of an experiment. Besides, for both cases, we assumed the initial concentration of analyte-antibody complex to be negligible ($[C]_0 = 0$).

In both deterministic continuum model and stochastic discrete model, a 6.8 μm-diameter sphere is modeled as the Luminex microbead carrying antibodies against the target molecules. The antibodies are assumed to be uniformly coated on bead surface and have reversible binding reaction with the target analytes (Figure 4.2, Equation 4.1).

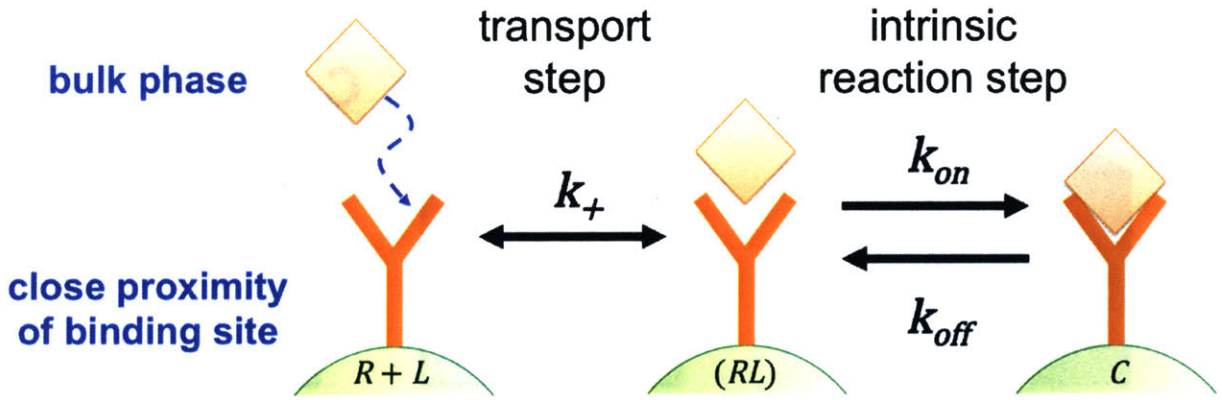

Figure 4.2 Schematic for reversible binding between target analyte (diamond) and the immobilized antibody (Y-shape) as a two-step process. The overall reaction could be separated into a transport step and an intrinsic reaction step. The transport step is characterized by rate constant k_+ and is influenced by diffusion and geometric consideration. The intrinsic reaction step is characterized by the intrinsic rate constant, k_{on} and k_{off}, which are determined by analyte and antibody molecular properties. The intermediate state, (RL), in which analyte and ligand are close enough to bind but have not yet done so is termed the encounter complex. The figure and caption are adapted from [14].

$$R + L \leftrightarrow (RL) \rightleftarrows C \tag{4.1}$$

As shown in Figure 4.2, the reversible binding reaction (Equation 4.1) can be considered as a two-step process, where a molecular transport step, with transport rate constant k_+ is required to bring the reactant molecules in close proximity physically before the intrinsic chemical reaction of binding can occur. The intrinsic associate and dissociate rate constants are termed as k_{on} and k_{off}, respectively, while the overall observed rate constants for onwards and reverse binding reactions are termed as k_f and k_r, respectively. For all simulations, we assumed that target analytes bind to antibodies at a 1:1 stoichiometry and

thus the dissociation constant for antibody specific capture has $K_d = k_{off}/k_{on}$. Notably, many kinetic experiments treated the overall reversible binding reaction as a one-step process and thus measured the observed rate constants, k_f and k_r, rather than the intrinsic rate constants. But, when the intrinsic chemical reaction step is the rate-limiting process rather than the molecular transport step, the observed rate constants would have similar values as the intrinsic rate constants. And this is often true in conventional bulk-scale kinetic experiments where both binding partners, R and L, are in large abundance. Therefore, we took values from reports on conventional bulk-scale kinetic experiments and assigned the same values to the intrinsic rate constants used in our models.

For simulations on external source of target analytes, the antibody-coated bead is assumed to be located at the bottom center of microwell surface for 1-bead case (Figure 4.1B). In 2-bead case (Figure 4.1C), we divided the bottom surface of microwell into four quadrants and positioned the second antibody-coated bead at the center of one quadrant. For simulations on cellular source of target analytes, we assumed an ideal position at the bottom center of microwell surface for the analyte-releasing cell in all cases. The position for bead with capture surface is assumed to be at the center of one quadrant of bottom microwell surface under default settings (Figure 4.1E). To study the impact of bead-cell distance on analyte capture, we also performed simulations for the situations with 11.4 μm center-to-center distance between the 6.8 μm-diameter bead and the 15 μm-diameter cell. In this case, the antibody-coated bead is assumed to be on the centerline of bottom microwell surface and the shortest distance between bead surface and cell surface is only 0.5 μm (Figure 4.1F).

4.2.1.1 Deterministic Continuum Model

The deterministic continuum model of molecular capture in confined volume is based on the experiments performed in this chapter. And all the simulations on deterministic continuum model were performed using COMSOL Multiphysics 4.3. Given the lack of active flow and fluid exchange within the closed microwell during incubation, we modeled the transport of analytes in assay buffer using simple diffusion model:

$$\frac{\partial[L]}{\partial t} = D_L \nabla^2 [L] \tag{4.2}$$

where D_L is the diffusion coefficient.

As mentioned above, we modeled the cases for both external and cellular sources of target analytes, to mimic the situations for assays on standard sample and assays on single cells, respectively. In the case of external source, different values are used for the initial concentration of free target analytes, $[L]_0$. In the case of cellular source, we assumed $[L]_0$ = 0 in the system and constant releasing of target analytes from cell:

$$L_{total} = k_g t \tag{4.3}$$

where L_{total} is the total amount of target analytes in the system. Therefore, at the cell surface, the diffusion flux is balanced against the reaction flux from analyte releasing.

$$-\mathbf{n} \cdot (-D_L \nabla[\mathrm{L}]) = k_g / A_{cell} \tag{4.4}$$

where A_{cell} is the surface area of the cell.

For both kinds of target sources, we have reversible binding reaction between analyte and antibody (Equation 4.1) on bead surface, where the diffusion flux of free analyte is balanced against the reaction flux from antibody-mediated binding.

$$-\mathbf{n}\cdot(-D_L\nabla[L]) = -\frac{\partial[C]}{\partial t} = -k_{on}([R]_0 - [C])[L] + k_{off}[C] \tag{4.5}$$

where $[R]_0$ is the initial concentration of all binding sites on bead surface and $([R]_0 - [C])$ describes the surface density of unoccupied binding sites at a given time point. The diffusion terms for the immobilized antibody R and analyte-antibody complex C are set to zero at bead surface.

We determined the values for all simulation parameters based on literature and our experimental setup. Notice that the standard samples we used in experiments contain recombinant c-Met/Fc chimera protein (358-MT-100/CF, R&D Systems, Inc., USA) as target analyte. The recombinant c-Met protein has a molecular weight of ~129.2 kDa, while the shed fragments of cellular c-Met have a molecular weight in the range of 50~100 kDa [1]. Thus, we estimated their diffusion coefficients to be close to that of antibodies and cytokines, whose molecular weights are ~150 kDa and 15~45 kDa, respectively [15]. Using bio-layer interferometry (Octet® RED96 system, Pall Corporation, USA), we experimentally determined the rate constants for the binding of recombinant c-Met protein to immobilized capture antibody (MAB3581, R&D Systems, Inc., USA), as $k_{on} = 6.85 \times 10^5\ (M \cdot s)^{-1}$ and $k_{off} < 10^{-4}\ s^{-1}$. Moreover, we estimated the density of total binding sites on the antibody-coated microbeads (46-650MAG, EMD Millipore Corporation, USA) based on experimental results of standard Luminex assay with the recombinant c-Met proteins (data not shown, protocol follows the manufacturer's instructions on the Luminex kit containing the antibody-coated microbeads). The resulting estimation is $[R]_0 \sim 10^{-8}\ mol/m^2$. In Table 4.1, we summarized the parameter values used in simulations for the deterministic continuum model and stochastic discrete model.

Table 4.1 Values of parameters used in simulations

Cell diameter	$15\ \mu m$
Bead diameter	$6.8\ \mu m$
Well size	Large well: $100\ \mu m \times 100\ \mu m \times 189\ \mu m$ ($1.89\ nL$ in volume) Small well: $50\ \mu m \times 50\ \mu m \times 50\ \mu m$ ($0.125\ nL$ in volume)
Density of total binding sites [16]	$[R]_0 = 600, 6000, 60000\ molecules/\mu m^2$ i.e. $[R]_0 \approx 10^{-9}, 10^{-8}, 10^{-7}\ mol/m^2$
Dissociation constant for binding [17]	$K_d = 0.1, 1, 10\ nM$ i.e. $k_{on} = 10^6, 10^5, 10^4\ (M \cdot s)^{-1}$; $k_{off} = 10^{-4}\ s^{-1}$
Analyte diffusion coefficient [15]	$D_L = 10^{-10}\ m^2/s$
Initial analyte concentration	External source: $l_0 = 10^2, 10^3, 10^4\ \#/well$ i.e. large well: $[L]_0 = 0.088, 0.879, 8.786\ pM$

Analyte releasing rate [1]	small well: $[L]_0 = 1.328, 13.284, 132.843\ pM$ Cellular source: $[L]_0 = 0$ External source: $k_g = 0$ Cellular source: $k_g = 0.1, 1, 10\ molecules/cell/s$

4.2.1.2 Stochastic Discrete Model

The stochastic discrete model we built shares the same model setup with the deterministic continuum model described above, in terms of macroscopic governing equations, boundary conditions and parameter settings. However, the diffusion process of analytes in the stochastic discrete model is simulated as random walk of individual molecules, while the reactions for both analyte releasing and antibody-analyte binding are treated as discrete events and simulated by computing the event's probabilities with random numbers. Therefore, in our stochastic discrete model, the binding reaction (Equation 4.1) is treated as a two-step process characterized by explicit molecular diffusion process and the intrinsic rate constants, k_{on} and k_{off}. And the initial transport step of the two-step reaction is modeled at molecular level by considering the physical contact of two binding partners. This formulation allows more realistic modeling of binding reaction and the analysis on fluctuations in binding outcomes of the entire system.

The numerical simulations on stochastic discrete model are performed using MCell (http://mcell.org) [18, 19], a general Monte Carlo reaction-diffusion simulator. A full description on the simulation design and programming of MCell could be found elsewhere [19]. Briefly, we created realistic 3D structures for the sealed microwell, antibody-coated bead and analyte-releasing cell. The concentration of molecular species in stochastic simulation is treated as the collection of molecule particles at precise locations. The diffusion of target analytes in the fluid phase of microwell is treated as random thermal motion of individual molecules in 3D. For a given molecule at time t, the distribution of its final positions at $(t + \Delta t)$ is calculated based on the governing diffusion equation (Equation 4.2) and then the MCell software would sample randomly from the calculated distribution to pick a specific position and update it as the new position of the given molecule at $(t + \Delta t)$. The impermeable walls of microwell are modeled as reflective boundary conditions, where the collision of analyte molecule with the wall would result in molecule trajectory following specular reflection. Same as in the deterministic continuum model, we do not consider the diffusion on bead surface for the immobilized antibodies and antibody-analyte complexes.

For external source of target analytes, the initialization step of MCell positions user-defined number of target moelcules (l_0) at random but precise locations within the fluid phase of the system. The exact positions of individual molecules are calculated based on random number stream and constrained to have pseudo-uniform concentration in fluid phase at $t = 0$. For cellular source of target analytes, we incorporated explicit reaction for analyte releasing from cell into the stochastic discrete model, in order to account for the randomness in the direction of analyte releasing.

$$RS \rightarrow L + RS \tag{4.6}$$

where RS is the analyte releasing site on the cell surface. We assumed a big surface diffusion coefficient for RS, $D_{RS} = 10^{-7}\ m^2/s$, which is chosen to give an average diffusion distance so large that the releasing site could appear at any location on cell surface over the simulation time step ($\Delta t = 0.1\ s$). Thus, the analyte releasing could occur anywhere on the cell surface. The analyte releasing reaction (Equation 4.6) has macroscopic rate constant, k_{RS}.

$$rs \cdot k_{RS} = k_g \tag{4.7}$$

where rs represents the number of releasing sites per cell. In this manner, Equation 4.3 still holds in the stochastic discrete model. We therefore implemented the simulations for $k_g = 0.1, 1, 10\ molecules/cell/s$ by setting values of (rs, k_{RS}) as $(1, 0.1), (1, 1), (10, 1)$, respectively.

In our stochastic discrete model, the bimolecular reactions between a volume molecule and a surface molecule (e.g. the forward reaction of Equation 4.1) occur only when the following two criteria are satisfied simultaneously. Firstly, there must be a collision between a volume molecule (or its movement ray) and the grid element containing the surface molecule. The grid element can be interpreted as the macroscopic reaction cross-section of the surface molecule. Secondly, the random number assigned for the collision has to be larger than the reaction threshold, which is the Monte Carlo probability p_{MC} that a collision would leads to a reaction event. Detailed derivation of the reaction threshold has been described previously [18]. Simply speaking, a diffusing volume molecule can hit the grid element occupied by the surface molecule multiple times before it diffuse infinitely far away from the grid element. Thus, the probability p_{MC} of reaction per collision should be equal to the quotient of the expected bulk reaction rate divided by the total number of collisions within one time step.

For the unimolecular, first-order reactions, such as Equation 4.6 and the reverse reaction of Equation 4.1, the distribution of expected lifetime for each reactant molecule is assumed to follow exponential decay. The software, MCell, then determines the exact lifetime of each molecule based on the lifetime distribution and schedules the unimoleular reaction accordingly at the appropriate time point. Moreover, given the spatial reversibility of a reversible binding reaction between a volume molecule and a surface molecule (e.g. Equation 4.1), the distribution of expected positions for a newly unbound volume molecule (e.g. the fluid-phase reaction product of unimolecular reaction) should match the distribution of positions for a free volume molecule that can potentially bump against the grid element occupied by the surface molecule (i.e. the same surface tile occupied by the reactant molecule undergoing unbinding reaction). In other words, by symmetry, the probability density distribution of volume molecules leaving the surface should be the same as the distribution of volume molecules that hit the surface. The simulator software hence calculates the spatial distribution of a newly unbound volume molecule (e.g. the fluid-phase reaction product of unimolecular reaction) and sample randomly from the calculated distribution to determine the exact position of a fluid-phase product molecule upon the unbinding reaction.

To evaluate the detection uncertainty resulting from stochastic reaction-diffusion events, we implemented numerical simulations for same set of parameters (listed in Table 4.1)

using multiple random number seeds of different values. Based on the seed value, the MCell software generates a series of random numbers that are used to determine the outcomes of individual decisions made during the simulation. Thus, the intrinsic noises derived from stochastic events could be estimated from the outcomes of individual simulations that are executed using different values in random number seed. The outputs of our numerical simulations are the molecule numbers for each species present in the system as a function of time. With the aid of MATLAB, we computed the mean and the coefficient of variation (CV, the ratio of the standard deviation to the mean) for different molecule species.

4.2.2 Flow Cytometry Characterization of Bulk Immunosandwich Assay

For all the immunosandwich experiments in this chapter, we used the magnetic microbeads coated with capture antibody and the biotinlyated detection antibody from a Luminex kit (46-650MAG, EMD Millipore Corporation, USA). The equivalent pair of capture antibody and detection antibody could also be purchased from R&D Systems, Inc. (USA) in solution form (capture antibody: MAB3581; biotinlyatd detection antibody: BAF358). This pair of antibodies could bind to the extracellular domain of human c-Met protein simultaneously and thus were used to measure the c-Met shedding of cells. The antibody-coated capture beads are 6.8 μm-diameter magnetic micro-particles with bright fluorescence in the allophycocyanin (APC) channel and thus can be manipulated in space using magnet. We used streptavidin-conjugated phycoerythrin (SAPE) as the fluorescent reporter for the immunosandwich assay. The standard samples used in this work are composed of different concentrations of recombinant c-Met/Fc chimera protein (358-MT-100/CF, R&D systems, Inc., USA), 1% BSA and serum-free medium for HCC827 cell culture (i.e. RPMI 1640 with 2mM glutamine, 100 U/L penicillin and 100 U/ml streptomycin).

For bulk immuosandwich assay, antibody-coated capture beads were washed once with 1%BSA/PBS and then incubated with 80 μL of standard samples in different recombinant c-Met concentrations in 1.7 mL microtubes at room temperature for 2 h on tube rotator (10136-084, VWR International, USA). The bead concentration was around 7500 #/mL of sample during the incubation step. After the 2-h incubation, the capture beads were washed 5× with washing buffer (0.1%BSA/PBS). Subsequently, the washed beads are incubated at room temperature for 1 h on tube rotator, with 1 μg/ml of biotinlyated detection antibody in 1%BSA/PBS. Then, the beads were washed 5× with washing buffer, followed by a 1-h incubation with 5 μg/ml SAPE in 1%BSA/PBS at room temperature on tube rotator. After incubation with SAPE, we washed the beads for 5× and then re-suspended them in 0.1%BSA/PBS before analyzed on flow cytometer (BD Accuri™ C6, BD Biosciences, USA). The magnetic beads were gated from the flow cytometry data based on their bright APC signals. The fluorescence signals of those beads in the PE (phycoerythrin) channel were used as indicator for the amount of target analytes (e.g. recombinant c-Met proteins) captured by individual beads. To minimize the impact of outliers, we trimmed off 5% data points with extremely high or low PE signals from the data for each condition. Those outliers might result from beads with abnormalities in bead size, reference dye (APC) concentration or antibody coating efficiency. Furthermore, to mimic the situation with low background signal, we used the median PE intensity of negative control sample as the baseline intensity and subtracted it from the original PE signal of each bead. The resulting bead signal is termed as the normalized PE signal. Coefficient of variation was

then calculated based on the normalized PE signal for each condition. Notice that for each washing step, we harvested the magnetic beads from solution by placing the sample on magnet (12321D, Thermal Fisher Scientific Inc, USA) for 5min before discarding the fluid.

4.2.3 Closed-Array Immunosandwich Assay with Recombinant c-Met

To prepare our microfluidic platform for immunosandwich assay with recombinant c-Met protein, we exposed both the bottom and top piece of the device to plasma treatment for 30 sec before coating their surfaces (i.e. the microwell surfaces and the flow chamber surfaces) with 1%BSA/PBS for 30 min at room temperature. After a brief washing step with 0.1%BSA/PBS, we dispensed 120 μL of magnetic antibody-coated beads (~400 beads/μL for large microwells, ~1000 beads/μL for small microwells) in assay buffer (1%BSA-containing serum-free medium) onto the BSA-coated microwell array and then allowed the beads to settle down for ~3 min while placing a neodymium block magnet (BCC2-N52, K&J Magnetics, Inc., USA) beneath the microwell array. The presence of magnetic field during bead loading greatly enhanced the loading efficiency of small magnetic beads into microwells. Subsequently, we carefully removed the block magnet and gently washed the microwell array from the side with assay buffer to remove the beads outside the microwells. After that, we assembled the bead-loaded microwell array with the top control piece of the device through mechanical clamping and connected the assembled device with fluid input and gas controlled as described in section 3.3.3. The entire assembly was then mounted within a stage top incubator (Tokai Hit Co., Ltd, Japan) that was secured onto the motorized stage (H117 ProScan™, Prior Scientific Inc., USA) of an inverted epifluorescence microscope (Olympus IX71, Olympus Inc., USA) equipped with a 12-bit CCD camera (SensiCam QE, PCO, Germany). In agreement with the conditions used for live-cell assay in section 4.2.4, 5% CO_2 was supplied to the humidified incubator during the entire assay.

Following the device assembly and mounting, the beads were imaged briefly for their locations under microscope at multiple positions along z directions. More than 99% of the magnetic beads were located at the bottom of each microwells. Then, the standard sample containing known concentration of recombinant c-Met protein in assay buffer would be injected into the flow chamber for 10 min before closing the valve for a 2-h incubation at 37 °C. The flow rate for buffer injection has been set differently for microwell arrays with different depths to achieve similar shear stress at the well bottom. In the case of large microwells, the total distance between microwell bottom to the ceiling of flow chamber is ~300 μm and the buffer injection was carried out at 40 μL/min. In the case of small microwells, the total distance reduces to ~150 μm and thus the buffer injection was performed at 20 μL/min. The same flow rate settings were used for all the buffer washing steps and the sample/dye incubation steps in both recombinant assays and live-cell assays. At the end of the closed-well incubation, the beads were rinsed with washing buffer (0.1%BSA/PBS) for 15 min to remove the unbound target analytes from the system. During the washing, the temperature of the humidified incubator was cooled down to room temperature (22 °C) and maintained for the rest of the assay. Subsequently, 1 μg/ml of biotinlyated detection antibody in 1%BSA/PBS was injected into flow chamber at 15 μL/min for 1 h, followed by a 15-min washing step with washing buffer to remove unbound detection antibody. Next, the beads were exposed to 5 μg/ml SAPE in 1%BSA/PBS under

continuous flow condition (15 μL/min) for 1 h. Notice that fluorescent images in the PE channel were recorded during SAPE incubation and would be processed to create mask that defines the regions within microwells in the array. Then, the beads were rinsed with washing buffer for 15 min to remove the unbound SAPE in the system. Finally, fluorescent images at different wavelength channels were taken for beads within microwells and would be used for subsequent data analysis of bead numeration and analyte capture status.

4.2.4 Single-Cell Measurement of c-Met Shedding

The immunosandwich assays with live cells were performed in a similar manner as the closed-array assays with recombinant protein (section 4.2.3). Detailed methods for cell culture and the device preparation step has also been described in section 3.3.2. Briefly, parental HCC827 cells were loaded onto microwell array coated with 40 μg/ml rat collagen I (A1048301, Invitrogen, USA) and then cultured in complete medium containing 10% FBS for 8~10 h at 37 °C with 5% CO_2. The seeded cells were then subjected to serum starvation for 6~8 h before assayed for molecular shedding. For all live-cell assays, cells were pre-loaded with viability dye, 2 μM calcein violet AM (C34858, Invitrogen, USA), for 30 min prior to the magnetic bead loading and device assembly with BSA-coated top control piece. After mounting the assembled device into the humidified incubator (37 °C, 5% CO_2), fluorescent images were recorded for the locations of antibody-coated beads and HCC827 cells as well as the cellular viability under microscope of multiple positions along z direction. Next, DMSO-containing assay buffer (1%BSA in serum-free medium) would be injected to flow chamber for 10 min, followed by pressurizing the valve control chamber to seal individual microwells. After 2-h incubation within sealed microwells, the cells and beads were rinsed with serum-free medium for 10min. The rinsed array was then exposed to 3 μM propidium iodide (P3566, Invitrogen, USA) and 0.8 μM Hoechst 33342 (H1399, Invitrogen, USA) in serum-free medium for 10min to stain the cells post-incubation. After the dye staining, the array was washed with washing buffer (0.1%BSA/PBS) for 15min before imaged under different wavelength channels at multiple depth positions. The post-staining fluorescent images would be used for downstream analysis on bead number, cell number and post-assay survival. Subsequently, the washed array was subjected to incubation with biotinlyated detection antibody and SAPE in sequence, with 15-min washing step in between, as described for recombinant assay in section 4.2.3. Images were also taken for microwell array during SAPE infusion and would be used downstream for well template generation. Lastly, the cells and beads were subjected to a final round of washing (15 min) and then recorded for fluorescence signals under different wavelength channels. The final-step images would be used for data analysis on analyte capture status.

4.2.5 Data Analysis for Microwell-Coupled Immunosandwich Assays

Manual numeration of cell number within each microwells was performed on fluorescent images taken post-incubation for cells stained with Hoechst 33342 and propidium iodide. We excluded data from microwells with non-cell objects (e.g. dirt and impurity in coating slolution) or cells died after the closed-array incubation from further analysis. Meanwhile, fluorescent images taken after SAPE staining were scrutinized manually to count the bead number within individual microwells and were used as "readout images" for further analysis on the readouts of immunosandwich assay. Each microwell array has either 960

large microwells or 1440 small microwells in total. Generally, we could get ~32%, 18%, 9% and 4% of microwells loaded with 1, 2, 3 and 4 beads, respectively, in a bead-loaded array. With the aid of Image J® software, template defining the regions within microwells was generated based on the raw images taken during SAPE infusion and aligned with "readout images" taken after SAPE staining. This aligned well template was then used in downstream data processing to group bead signals into individual microwells. Based on the "readout images", we further created two masks to define the regions of interests (ROI) for cell nuclei (based on Hoechst signal) and beads (based on APC signal), respectively. Furthermore, we dilated the ROIs of cell nuclei template by 3 pixels (i.e. ~7μm) to get a mask for the entire cell and then overlaid it with the bead mask to identify the antibody-coated beads lying in close proximity of the cells. A corrected bead mask was then generated by excluding those near-cell beads from the ROIs of raw bead mask.

We have developed a procedure for image processing and signal analysis. Firstly, we generated one aligned microwell template, one mask for entire cells, and one corrected bead mask, as mentioned above. Secondly, to fix the uneven background arising from non-uniform illumination within the observation window, we performed rolling-ball background subtraction on the "readout images" using Image J® software under the settings of sliding paraboloid and rolling ball radius = 50 pixels. Thirdly, taking advantage of the particle analysis function of Image J®, we extracted the coordinates and corrected fluorescence signals of individual beads from the background-subtracted "readout images" using the corrected bead mask. To avoid the variation introduced by inaccurate border identification, we used the median value of fluorescence intensity of each ROI as the signal indicator for the corresponding bead. Lastly, we mapped the bead signals to each microwell based on bead coordinates and the aligned microwell template using MATLAB. Thus, we have information about individual microwells for the following parameters: cell number, bead number and fluorescence signals of each bead in both PE and APC channel. The PE signals of beads were the readouts of immunosandwich assay and should correlate with the amount of target analyte captured on each bead. To minimize the impact of outliers, we trimmed off 5% data points with extremely high or low PE signals from the data for each microwell array. Those outliers might result from beads with abnormalities in bead size, reference dye (APC) concentration or antibody coating efficiency. The average per bead fluorescence signal was also calculated for microwells with more than one antibody-coated bead. For simplicity, we only considered 1-bead well for the data analysis of live-cell assay.

4.3 Analytical Theories of Fluctuations in Low-Abundance Molecular Capture

The readout signals of any single-cell measurement are usually in a form of distribution rather than a signal value. There are mainly three distinctly different sources of variation in the readout signals: biological variability, detection uncertainty and experimental artifacts. Biological variability refers to the real difference in the single-cell properties under study. Detection uncertainty results from the physical constraints underlying the mechanisms of a detection method and is dominated by fluctuation in low-abundance molecular capture in this study. Experimental artifacts are the ensemble outcomes of operational errors in real world. While active efforts in the field have been devoted to address the issue of experimental artifacts, we would like to focus on the detection uncertainty, which can mask the key biology under study (biological variability) by putting the ultimate limits even for a

perfect readout system.

Antibody-mediated analyte capture is the first step of analyte quantification using immunosandwich assay. Fluctuations in the analyte capture translate directly into the variance of final readout. The physics of antibody-mediated analyte capture, especially in the case of low-abundance analytes, presents analogy to that of the receptor/ligand binding in many aspects. Both processes involve reversible binding between volume molecules and surface molecules to produce molecular complexes on the surface (Equation 4.1) and suffer from the stochastic nature of molecular events due to limited number of molecules. In 1977, Berg and Purcell [20] published a paper on how the statistical fluctuations in the cellular microenvironment could limits the precision of binding-based biochemical sensing. While they used a simplified physical model of receptor/ligand binding, Berg and Purcell's analysis provides the upper bound for the accuracy of cellular sensing through receptor/ligand binding. Analysis on more complex physical models can also be found elsewhere [21-23]. Inspired by those studies, we construct a probabilistic formulation of the antibody-mediated analyte capture in this section and only consider the simple case of antibody-analyte binding in the absence of significant antibody depletion and nonspecific binding. For simplicity, we treated the reversible binding reaction as a one-step process characterized by the observed rate constants, k_f and k_r, in section 4.3.

4.3.1 Fluctuations in Source Concentrations

For the binding between immobilized antibody and analyte (Equation 4.1), we have the following reaction flux for antibody-analyte complex on the immobilization surface (i.e. bead surface).

$$\frac{d[C]}{dt} = k_f([R]_0 - [C])\left([L]_0 - \frac{N_b A_b}{V_{well}}[C]\right) - k_r[C] \tag{4.8}$$

where N_b, A_b and V_{well} are the bead number per unit volume, the surface area of an antibody-coated bead, and the volume of closed microwell, respectively. We define a scaling factor, $sf = N_b A_b / V_{well}$, to transform the surface concentration of binding sites on bead to the volume concentration in the system. Thus, $\left([L]_0 - \frac{N_b A_b}{V_{well}}[C]\right) = ([L]_0 - sf[C])$ represents the volume concentration of freely diffused target analyte in the fluid phase of the system at given surface concentration of complex, $[C]$. Since we only consider the case with extremely low concentration of target analyte, we assume no significant depletion in the available binding sites occur in the system. Therefore, we have nearly constant amount of available binding sites on the bead surface (i.e. $[R] = [R]_0 - [C] \approx [R]_0$). We then can solve Equation 4.8 under the equilibrium condition (i.e. $d[C]/dt = 0$) and get the transient solution under the initial condition of $[C]_0 = 0$.

$$[C]_{eq} = \frac{[R]_0[L]_0}{sf[R]_0 + K_D} \tag{4.9}$$

$$[C](t) = [C]_{eq}\left(1 - e^{-k_{obs}t}\right) \tag{4.10}$$

where $[C]_{eq}$ represents the equilibrium concentration of analyte-antibody complex,

$K_D = k_r/k_f$, is the observed antibody dissociation constant, and $k_{obs} = k_f(sf[R]_0 + K_D)$ is the characteristic rate constant of approach to equilibrium. Therefore, both the capture efficiency at equilibrium, $[C]_{eq}/[L]_0 = [R]_0/(sf[R]_0 + K_D)$, and the speed of approaching equilibrium, k_{obs}, are functions of $[R]_0$ and K_D.

By taking partial derivatives of Equation 4.9 and rearranging the outcome, we noticed that fluctuations in concentrations of source molecules, $[L]_0$ or $[R]_0$, would result in corresponding fluctuations in the concentration of binding products, $[C]_{eq}$. The relative magnitude of these fluctuations can be expressed in terms of coefficient of variation (CV) as below [24].

$$\frac{\partial[C]_{eq}}{[C]_{eq}} = \frac{\partial[L]_0}{[L]_0} \tag{4.11}$$

$$\frac{\partial[C]_{eq}}{[C]_{eq}} = \left[1+\frac{sf[R]_0}{K_D}\right]^{-1}\frac{\partial[R]_0}{[R]_0} \tag{4.12}$$

where $\partial[C]_{eq}$, $\partial[L]_0$ and $\partial[R]_0$ represent the standard deviation in $[C]_{eq}$, $[L]_0$ and $[R]_0$, respectively. We then can use Equation 4.11 and 4.12 to estimate the impact of fluctuations in source molecule concentration on the binding outcome at equilibrium.

The actual concentration of freely diffused target analytes sampled by the antibody-coated bead is fluctuating due to the thermal fluctuations of solvent molecules (i.e. Brownian motion). And the thermal fluctuations in volume molecule concentration, $\partial[L]_0$, can be estimated based on the sampling volume V, which is the volume of fluid phase accessible to binding [25]:

$$\partial[L]_0/[L]_0 = ([L]_0V)^{-1/2} \tag{4.13}$$

Notice that $[L]_0$ in Equation 4.13 has unit in terms of molecule number per unit volume, and thus one would need to use Avogadro's number to translate molar concentration into the form of molecule number per unit volume when using Equation 4.13 to estimate the effect of thermal fluctuations.

For immunosandwich assay in bulk, the characteristic length l_V of the sampling volume is given by the average diffusion length of target anlayte within sampling time t_{sample}.

$$l_V \sim \sqrt{D_L t_{sample}} \tag{4.14}$$

Considering the analyte-antibody binding reaction, a reasonable estimation for t_{sample} is $1/k_r$, which is the average gap time between two binding events at steady state for the case of $[L]_0 = K_D$. Thus, $V \sim l_V^3 \sim (D_L/k_r)^{3/2}$ and in our experimental system with $D_L = 10^{-10}\ m^2/s$ and $k_r = 10^{-4}\ s^{-1}$, the sampling volume is 1 μL (i.e. $l_V \sim 1\ mm$), which is several orders of magnitude larger than the volume of our microwell. Therefore, for the closed-array immunosandwich assay, the sampling volume should be the volume of the sealed microwell. On one hand, the bulk assay ($V \sim 1\ \mu L$) has negligible variability in the $[L]$ being sampled, given that $\partial[L]_0/[L]_0 \sim 0.407\%$ at $[L]_0 = 0.1\ pM$. On the other hand, the actual close-array immunosandwich assay could have very large fluctuations in the exact amount of target analytes being encapsulated within individual microwells. In the case of small

microwell ($V = 0.125\,nL$), we find $\partial[L]_0/[L]_0 \sim 36.44\%, 11.53\%, 3.64\%$ for $[L]_0 = 0.1, 1, 10\,pM$, respectively. In the case of large microwell ($V = 1.89\,nL$), we find $\partial[L]_0/[L]_0 \sim 9.37\%, 2.96\%, 0.94\%$ for $[L]_0 = 0.1, 1, 10\,pM$, respectively. Moreover, based on Equation 4.11, those fluctuations in $[L]_0$ would lead to corresponding fluctuations of similar magnitude in the binding outcome $[C]_{eq}$. And thus, caution has to be taken when interpreting outcomes from the closed-array immunoassay with standard sample of very low analyte concentration.

In the case of live-cell assay, deviations in $[L]$ from the mean behavior predicted by the deterministic continuum model could directly arise from the discrete events of analyte releasing from cell. Besides, for cells with same analyte production rate, the major source of $\partial[L]$ at a given time point is variability in the exact timing of molecule releasing, which has been taken into account in our stochastic discrete model.

In reality, the fluctuations in binding site density, $\partial[R]_0$, could arise from the operational variation during bead fabrication and antibody coating, and thus is considered as parameter for bead quality control. Equation 4.12 dictates, for example, that in the case of small microwell containing only 1 bead with average $[R]_0 = 6000\ \#/\mu m^2 \approx 10^{-8}\ mol/m^2$, 10% CV in $[R]_0$ translates to 0.086% CV and 0.864% CV in $[C]_{eq}$ at $K_D = 0.1, 1\,nM$, respectively. Hence, in our system of closed-array immunosandwich assay, variability in $[R]_0$ has negligibly low impact on the amount of analyte-antibody complexes at equilibrium.

Notice that our stochastic discrete model doesn't consider variability in initial conditions so that each simulation was executed with exact values of $[L]_0$ and $[R]_0$ in the system at $t = 0$.

4.3.2 Fluctuations in Binding Kinetics

The probabilistic nature of binding reaction is another major source of fluctuations in final binding outcome. The reaction rate constant of a chemical reaction could be interpreted as the reaction probability per unit time [26]. In other words, when we consider a time interval Δt that is small enough to have no more than one reaction occurring, $k_f[L]$ and $k_r\Delta t$ can represent the probability per unit time of an association and dissociation event to occur (on a given reactant molecule during Δt), respectively. Consequently, we could analyze the impact of fluctuating binding kinetics using a population balance model of analyte-antibody complexes [27]. In the rest of this section, we use $P_i(t)$ to represent the probability of i analyte-antibody complexes present on the bead surface at time point t. The scaling factor, $sf = N_b A_b / V_{well}$, is defined as the same in section 4.3.1, and thus $([L]_0 - sf[C])$ represents the volume concentration of freely diffused target analyte in the fluid phase of the system at given surface concentration of complex, $[C]$. We also use $[C \pm 1]$ to represent the corresponding surface concentration for $(c \pm 1)$ number of complexes present on a bead and $[R]_{[C]}$ to represent the surface concentration, in terms of molecule number per area, for r number of unoccupied binding sites at a given $[C]$. Thus, we could write the following kinetic equation to describe the changes in $P_c(t)$ [14]:

$$
\begin{aligned}
P_c(t+\Delta t)-P_c(t) = {} & k_f\left([L]_0 - sf[C-1]\right)[R]_{[C-1]}P_{c-1}(t)\Delta t \\
& -k_f\left([L]_0 - sf[C]\right)[R]_{[C]}P_c(t)\Delta t \\
& -k_r[C]P_c(t)\Delta t + k_r[C+1]P_{c+1}(t)\Delta t
\end{aligned} \tag{4.15}
$$

Given that target analyte is in extremely low abundance, we assume nearly constant amount of available binding sites, $[R]_{[C]}, [R]_{[C\pm1]} \approx [R]_0$. Therefore, in the limit of $\Delta t \to 0$, Equation 4.15 can be rewritten into a differential equation.

$$
\begin{aligned}
\frac{dP_c(t)}{dt} = {} & -k_f([L]_0 - sf[C-1])[R]_0 P_{c-1}(t) + k_r[C+1]P_{c+1}(t) \\
& -\left\{k_f([L]_0 - sf[C])[R]_0 + k_r[C]\right\}P_c(t)
\end{aligned} \tag{4.16}
$$

where $c = 1, 2, 3, \ldots, (r_0 - 1)$. For $c = 0$ and $c = r_0$, the corresponding equations are as below.

$$
\frac{dP_0(t)}{dt} = -k_f[L]_0[R]_0 P_0(t) + k_r P_1(t) \tag{4.17}
$$

$$
\frac{dP_{r_0}(t)}{dt} = k_f[L]_0 P_{r_0-1}(t) - k_r[R]_0 P_{r_0}(t) \tag{4.18}
$$

For our system, we assume no bound antibodies present at $t = 0$ and thus the initial condition is the following Equation 4.19.

$$
P_c(t=0) = \begin{cases} 0 & if\ c \neq 0 \\ 1 & if\ c = 0 \end{cases} \tag{4.19}
$$

The set of Equation 4.16~4.18 can be solved analytically by transforming those $(r_0 + 1)$ coupled linear ordinary differential equations into a single partial differential equation. The detailed derivation of solution could be found elsewhere [14, 28]. Using the analytical solutions, we can get the expected value of [C] (denoted as $< [C] >$) and its variance σ_c^2 at equilibrium.

$$
<[C]_{eq}> = \left(\sum_{c=0}^{r_0}[C]P_c\right)_{eq} = \frac{[R]_0[L]_0}{sf[R]_0 + K_D} \tag{4.20}
$$

$$
\left(\sigma_c^2\right)_{eq} = \left(\sum_{c=0}^{r_0}\left([C] - <[C]>\right)^2 P_c\right)_{eq} = \frac{[R]_0[L]_0 K_D}{\left(sf[R]_0 + K_D\right)^2} \tag{4.21}
$$

Notice that the expected value of [C] at equilibrium (Equation 4.20) is identical to the solution $[C]_{eq}$ (Equation 4.9) given by the deterministic continuum model (Equation 4.8). Combining Equation 4.20 and Equation 4.21, we can evaluate the effect of stochastic and discrete reaction events on $[C]_{eq}$ in terms of CV.

$$
\frac{\partial[C]_{eq}}{[C]_{eq}} = \frac{(\sigma_c)_{eq}}{[C]_{eq}} = \left(\frac{K_D}{[R]_0[L]_0}\right)^{1/2} \tag{4.22}
$$

For the parameter values used in our system (Table 4.1), we would expect 10.71%CV, 3.39% CV and 1.07% CV in $[C]_{eq}$ at $[L]_0 = 0.1$pM, 1pM, 10pM, respectively, in the case of $K_D = 1nM$ and $[R]_0 = 6000\ \#/\mu m^2$. The relative fluctuations in $[C]_{eq}$ would increase if beads coated with antibodies of poor affinity (larger K_D) or at low binding site density (smaller $[R]_0$) are used to capture target analyte. Notably, Equation 4.22 applies to all kinds of binding assays under condition of negligible antibody depletion, including the immunosandwich assays performed in bulk scale. Our stochastic discrete model has incorporated the fluctuations in binding kinetics by simulating the reversible binding reaction between target analyte and immobilized antibody as individual discrete-time event.

4.4 Modeling Results of Closed-Array Assays on Sample with Fixed Target Concentration

In the case of external source of target analytes, our numerical simulations on both deterministic continuum model and stochastic discrete model indicate that the temporal profile of capture efficiency, $[C]/[L]_0$, is not dependent on the initial concentration of target molecule in the system (Figure 4.3A, B). Meanwhile, microwell of smaller dimension, increase in surface concentration of binding site or decrease in antibody dissociation constant (i.e. increase in k_{on}) would result in faster equilibrium (Figure 4.3). This is in agreement with the analytical expression of transient solution, $[C](t)$, to the kinetic equation of binding reaction (Equation 4.10). Additionally, the mean behavior predicted by the stochastic discrete model is consistent with the simulation outcomes of the deterministic continuum model, with only minor deviation when the binding rate of the entire system is extremely low. In the case of small microwell ($50\ \mu m \times 50\ \mu m \times 50\ \mu m$) that is suitable for assaying non-adherent cells or cells with limited spreading, both models predicts near-100% capture efficiency after 1-h incubation period for systems with $K_d = 1nM$ and $[R]_0 = 6k\ \#/\mu m^2$. However, when larger microwell ($100\ \mu m \times 100\ \mu m \times 189\ \mu m$) are used, the same parameter settings would only result in ~40% capture efficiency after 5-h incubation, making the secretion/shedding detection of cells with large spreading area or high motility, more challenging. On the other hand, one could limit the cell spreading area and cellular migration space by surface patterning of extracellular matrix molecules and anti-fouling materials on the walls of microwells, hence allowing the usage of small microwells for those actively migrating cells.

We next examine the fluctuations in the number of captured target analytes. Our simulations on the stochastic discrete model reveal that the fluctuations of analyte-antibody complex number decrease over time and reach a pseudo-steady state when the molecular capture has reached equilibrium state in the system (Figure 4.3, column III). In Figure 4.4, we plotted the coefficient of variation (CV) of the equilibrium number of analyte-antibody complexes as a function of antibody dissociation constant K_d, surface concentration of total binding sites $[R]_0$ and the initial concentration of target analytes $[L]_0$, respectively. In accordance with Equation 4.22, we observed a linear relationship between $Log(CV)$ vs. $Log(K_d)$, $Log(CV)$ vs. $Log([R]_0)$, and $Log(CV)$ vs. $Log([L]_0)$, with a slope of (0.470 ± 0.001), (-0.458 ± 0.024) and (-0.495 ± 0.025), respectively. This good agreement of numerical simulation results with Equation 4.22 supports that the fluctuations in

binding kinetics are the major source of variation in binding outcomes at equilibrium. And thus, we could rely on the stochastic discrete model to calculate the intrinsic noise of a given system for any time point during sample incubation. Furthermore, our results indicated that the uncertainty in binding-based molecule detection would increase in the case of capture antibody with poor affinity (large K_d), low binding site availability (lower $[R]_0$) or few target molecules (smaller $[L]_0$). Enlarging the microwell size would also increase the CV for same amount of target analytes in the system. For antibody with $K_d = 1nM$ and binding site density of 6000 $\#/um^2$ (equivalent to $10^{-8}\, mol/m^2$), 100 molecules of target analytes would result in 12.6% CV and 2.6% CV after 5-h incubation time with antibody-coated bead in closed-array system with large and small microwell, respectively. This kind of fluctuations is intrinsic to the binding reaction and establishes the lower bound to the detection uncertainty of molecule quantification using binding-based approach. Thus, caveat should be taken when translating the binding outcomes into the amount of target analytes present within system.

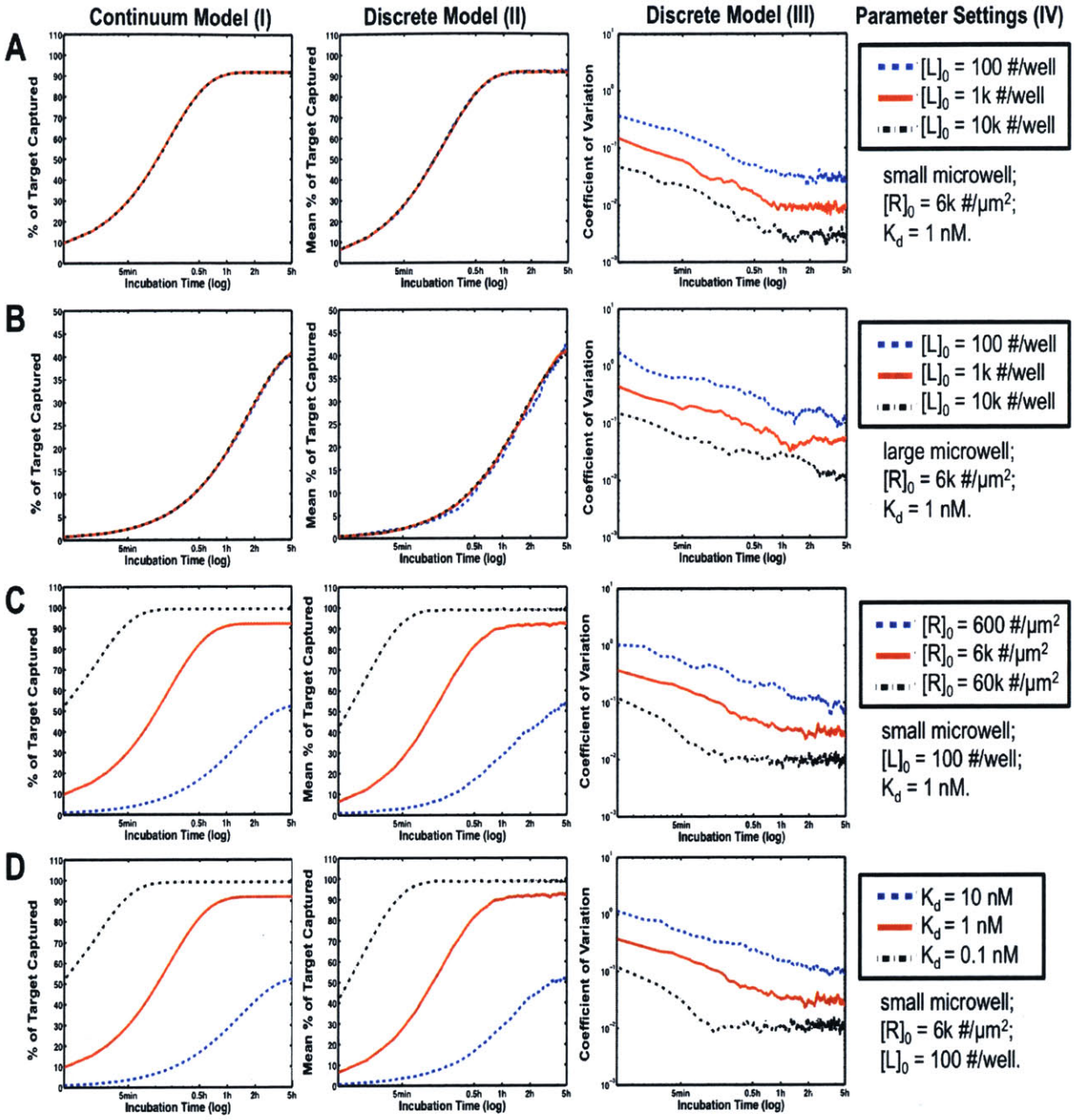

Figure 4.3 Temporal profile of molecular capture in closed-array configuration for external source of target analytes. Column (**I**) shows the capture efficiency predicted by our deterministic continuum model. Column (**II**) and (**III**) depict the average capture efficiency and coefficient of variation (CV) of the captured analyte number, respectively, both of which are from numerical simulations on our stochastic discrete model. Column (**IV**) lists the parameter settings and legends used for each row. The capture efficiency is defined as the parentage of total target analyte being captured by the immobilized antibodies in the system. X-axis represents the incubation time in logarithmic scale. Y-axes of column (**I, II**) are in linear scale for capture efficiency, while y-axis of column (**III**) is in logarithmic scale for CV values. For stochastic discrete model, different values of random number seeds were used to implement simulations on same set of parameters. In the case of small microwell with dimension of $50\ \mu m \times 50\ \mu m \times 50\ \mu m$ (**A, C, D**), $n = 50$ for $[L]_0 = 100\ \#/well$, $n = 22$ for both $[L]_0 = 1k\ \#/well$ and

$[L]_0 = 10k\ \#/well$. In the case of large microwell with dimension of $100\ \mu m \times 100\ \mu m \times 189\ \mu m$ (**B**), $n = 22$ for all conditions.

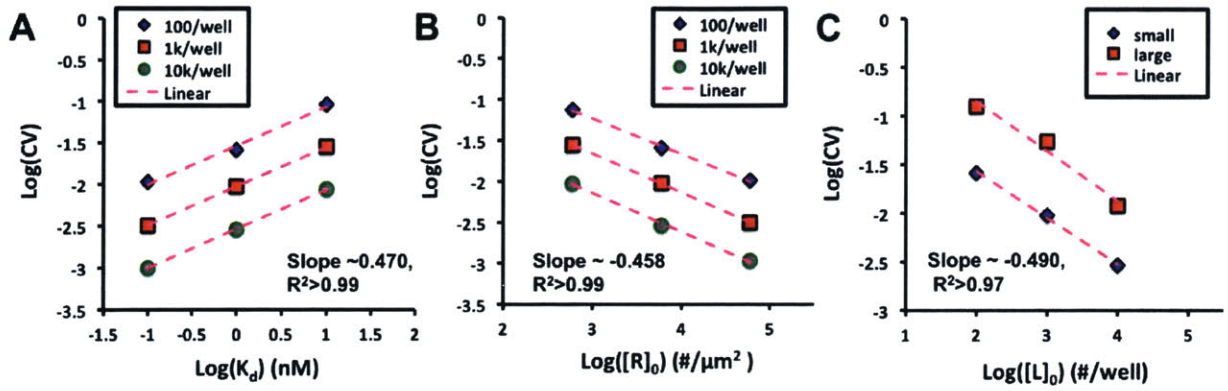

Figure 4.4 Coefficient of variation (CV) of the captured analyte number at equilibrium for closed-array molecular capture of target analytes from external source. The plots are based on numerical simulations of the stochastic discrete model. The CV values depicted in the plots are the average value of CV over the last 10 min of the 5-h incubation time ($t = 4\ h\ 50\ \text{min} \sim 5\ h$). During this time period, majority cases of analyte capture have reached equilibrium with relatively stable CV values. The parameter settings for each plot are (**A**) small microwell ($50\ \mu m \times 50\ \mu m \times 50\ \mu m$), $[R]_0 = 6k\ molecules/\mu m^2$ with different $[L]_0$ shown in legend; (**B**) small microwell, $K_d = 1\ nM$ with different $[L]_0$ shown in legend; (**C**) $[R]_0 = 6k\ molecules/\mu m^2$, $K_d = 1\ nM$ with either small microwell or large microwell ($100\ \mu m \times 100\ \mu m \times 189\ \mu m$). Both x-axis and y-axis are in logarithmic scale. The purple dashed lines represent the linear least-squares fitting of data. In the case of small microwell (**A, B, C**), $n = 50$ for $[L]_0 = 100\ \#/well$, $n = 22$ for both $[L]_0 = 1k\ \#/well$ and $[L]_0 = 10k\ \#/well$. In the case of large microwell (**C**), $n = 22$ for all conditions.

4.5 Modeling Results of Closed-Array Assays on Single-Cell Shedding

When applying the closed-array immunosandwich assay to single-cell shedding detection, the system contains a cell that is releasing target analytes over time. As a result of the interplay between target generation and target binding to antibodies within confined space, the molecular capture of the entire system usually goes through three characteristic phases in this case of cellular source of target analytes (Figure 4.5). During the first phase, the forward reaction rate of antibody-analyte binding is slower than the analyte generation rate by the cell, resulting in more target analytes present in solution phase than on bead surface. With more molecules accumulated in solution phase, the forward reaction rate keeps increasing to be higher than the target generation rate. The system then proceeds into the second phase featured by relatively stable profile for the amount of target analytes in solution over time. Meanwhile, the resulting capture efficiency also increases until the binding sites are gradually saturated. In ensuring period of time, the system moves into the third phase with a slower binding reaction rate than the target generation rate and hence experiences a decrease in the capture efficiency.

Generally speaking, the ideal end point for closed-array incubation of cells with capture antibody should fall into the latter part of second phase, where the system has high capture efficiency and a relatively large dynamic range in measuring different analyte-releasing

rates given the present of sufficient unoccupied binding sites. However, there are practical constraints on the length of closed-array incubation for live cells. The confinement of live cells eliminates the transportation of nutrients and wastes across the compartment boundaries. Although high viability has been reported for cancer cell line after 4 days of confinement in sub-nanoliter volume of droplets [29], the viability of many other mammalian cells, particularly the primary immune cells, diminishes significantly when the closed-array incubation time exceeds 4~6 h [30]. Besides, long-term confinement would also impact cellular phenotypes. One typical case is the droplet-encapsulated cancer cells, which exhibited very limited cell growth after encapsulation [29]. Thus, a reasonable live-cell assay should have a closed-array incubation time less than 4 h. Furthermore, given the well-known fact that cellular signaling is a dynamic process, live-cell shedding assay with even less incubation time is always desired and would be valuable to reveal the dynamic temporal behavior of cell shedding.

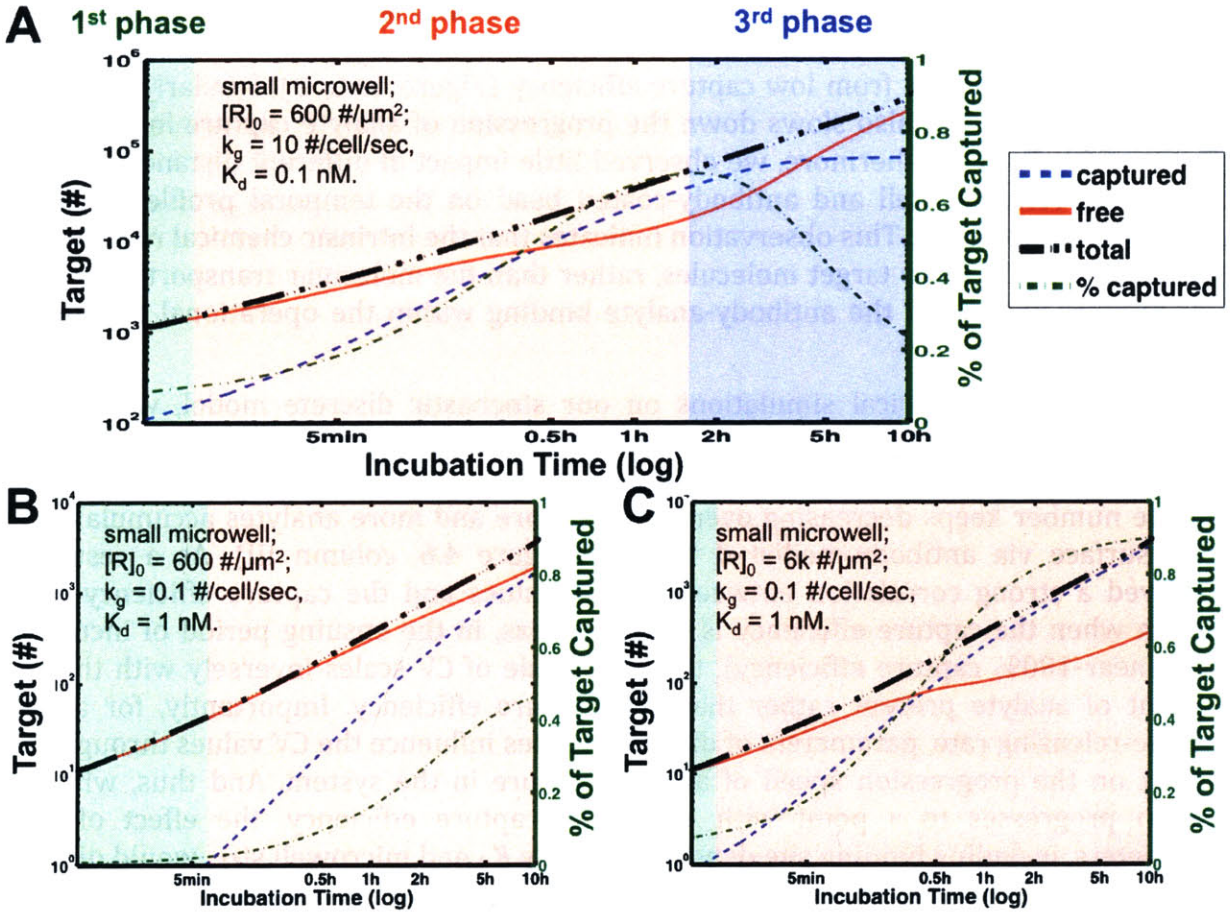

Figure 4.5 Temporal profile of target analyte distribution for single-cell shedding detection in closed-array configuration. There are three characteristic phases of molecular capture in the system under study. The first phase (shaded in green) is featured by a slower antibody-analyte binding rate than the target generation rate by the cell and thus has very low capture efficiency. The second phase (shaded in red) is characterized by a rapid increase in capture efficiency and a relatively stable profile of target molecules in solution over time. The third phase starts when the capture efficiency starts to decrease as a result of binding site saturation. Plots are based on simulation results of the deterministic continuum

model in the case of sealed microwell containing only one antibody-coated bead and one analyte-releasing cell. X-axis represents the incubation time in logarithmic scale. Plots are shown for the quantities of target analytes accumulated in the whole system (black dash-dot-dot line), free in the fluid phase (red solid line) and captured on antibody-coated bead surface (blue dashed line), respectively, with y-axis on the left in logarithmic scale. Green dash-dot lines depict the percentage of total target analytes being captured by antibodies, with y-axis on the right in liner scale. The parameter settings used for simulation are shown in each plot.

To identify the optimal design for live-cell shedding detection using closed microwell, we used both deterministic continuum model and stochastic discrete model to study the effect of different parameters on assay performance. As shown in Figure 4.6A & B, the temporal profile of capture efficiency is largely insensitive to different analyte-releasing rates from the cell (k_g) for the parametric space under study. This feature enables the closed-array immunosandwich assay to quantify a wide range of analyte-releasing rate with a fixed incubation time period. Whereas, antibody with low affinity (larger K_d) or low surface density (lower $[R]_0$) could result in slower progression of analyte capture and thus longer time period that suffers from low capture efficiency (Figure 4.6C, D). Similarly, microwell with larger dimension also slows down the progression of analyte capture in the system (Figure 4.6A, B, E). Furthermore, we observed little impact of different distances between the analyte-releasing cell and antibody-coated bead on the temporal profile of capture efficiency (Figure 4.6F). This observation indicates that the intrinsic chemical reaction step between antibodies and target molecules, rather than the molecular transport step, is the rate-limiting process of the antibody-analyte binding within the operational envelope of interest.

With the aid of numerical simulations on our stochastic discrete model, we can also investigate the impact of various parameters on the intrinsic noise of single-cell shedding assay using closed microwell. The relative magnitude of fluctuations (CV) in captured analyte number keeps decreasing over time as more and more analytes accumulate onto bead surface via antibody-mediated binding (Figure 4.6, column III). As a result, we observed a strong correlation between the CV values and the capture efficiency of the system when the capture efficiency is low. Whereas, in the ensuing period of incubation (with near-100% capture efficiency), the magnitude of CV scales inversely with the total amount of analyte present rather than the capture efficiency. Importantly, for a given analyte-releasing rate, parameters of different values influence the CV values through their impact on the progression speed of analyte capture in the system. And thus, when the system progresses to a point with very high capture efficiency, the effect of those parameters, including binding site density, antibody K_d and microwell size, would diminish. On the contrary, the impact of analyte-releasing rate from the cell persists during the entire incubation period. And we observed a liner relationship between $Log(CV)$ and $Log(k_g)$ at the end of 10-h incubation time for all conditions simulated (Figure 4.7). Therefore, the optimal system for close-array detection of single-cell shedding should enable high capture efficiency within the operation window of incubation time and the optimal length of incubation time should be as long as the practical constraints allow.

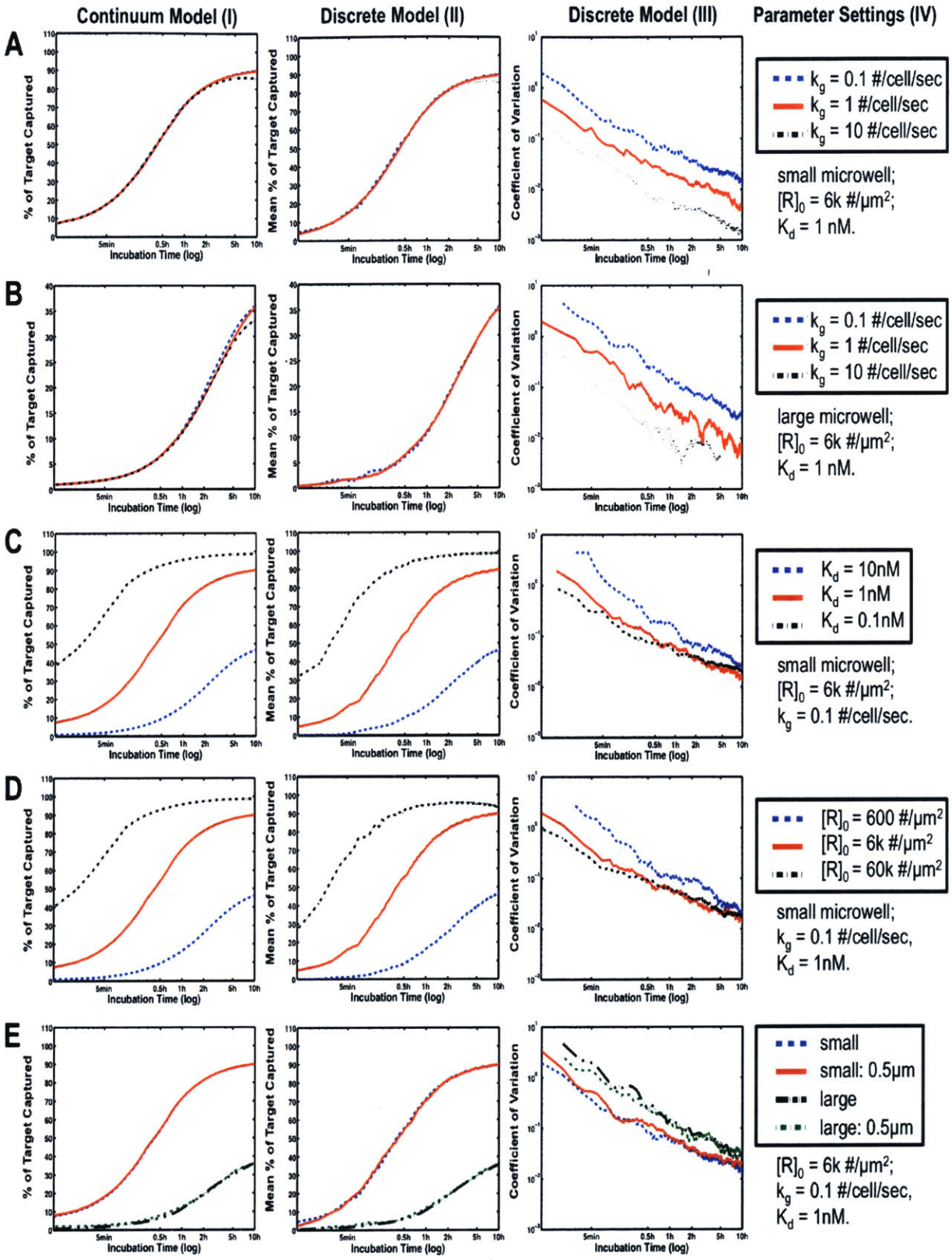

Figure 4.6 Temporal profile of molecular capture in closed-array configuration for cellular source of target analytes. Plots are based on simulation results of two models in the case of sealed microwell

containing only one antibody-coated bead and one analyte-releasing cell. Column (**I**) shows the capture efficiency predicted by our deterministic continuum model. Column (**II**) and (**III**) depict the average capture efficiency and coefficient of variation (CV) of the captured analyte number, respectively, both of which are from numerical simulations on our stochastic discrete model. Column (**IV**) lists the parameter settings and legends used for each row. The capture efficiency is defined as the parentage of total target analytes being captured by antibody-coated bead. X-axis represents the incubation time in logarithmic scale. Y-axes of column (**I, II**) are in linear scale for capture efficiency, while y-axis of column (**III**) is in logarithmic scale for CV values. The coordinates of cell and bead used for simulation are shown in Figure 4.1E and Figure 4.1F for the default settings (**A-E**) and the case of bead-cell distance = 0.5 μm (**E**), respectively. For stochastic discrete model, different values of random number seeds were used to implement simulations on same set of parameters. $n = 21$ for all conditions.

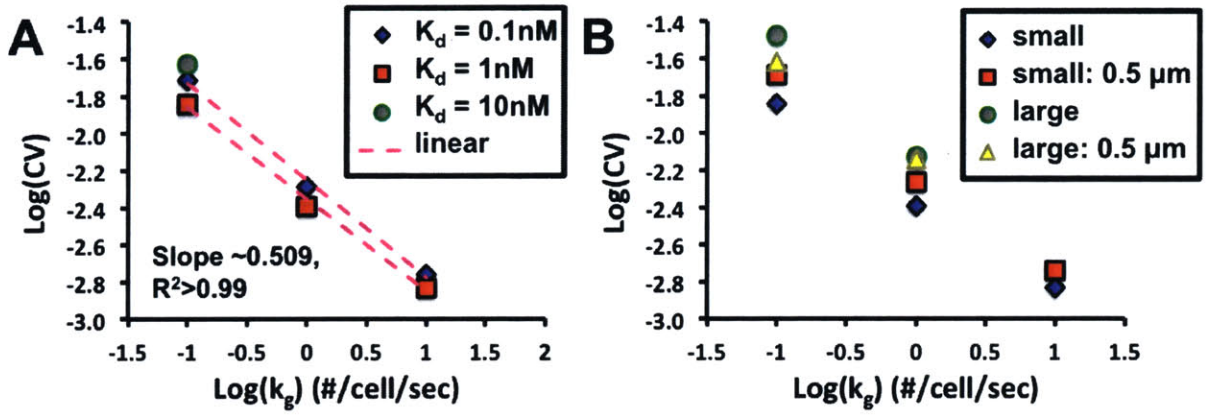

Figure 4.7 Coefficient of variation (CV) of the captured analyte number after 10-h incubation of an analyte-releasing cell with an antibody-coated bead in closed microwell. The plots are based on numerical simulations of the stochastic discrete model. The CV values depicted in the plots are the average value of CV over the last 10 min of the 10-h incubation time ($t = 9\ h\ 50\ \text{min} \sim 10\ h$). During this time period, majority cases of analyte capture within small microwell ($50\ \mu m \times 50\ \mu m \times 50\ \mu m$) have reached the 2nd phase with more than 80% capture efficiency and a relatively stable temporal profile of capture efficiency. One exception is the case of small microwell and $K_d = 10nM$, where the system has less than 50% capture efficiency. Meanwhile, all the simulated cases of large microwell ($100\ \mu m \times 100\ \mu m \times 189\ \mu m$) have lower than 40% capture efficiency after 10-h incubation time. The parameter settings for each plot are (**A**) small microwell, $[R]_0 = 6k\ molecules/\mu m^2$ with different K_d shown in legend; (**B**) small or large microwell, $K_d = 1\ nM$, $[R]_0 = 6k\ molecules/\mu m^2$ with bead-cell distance either at default setting or as close as 0.5 μm. Both x-axis and y-axis are in logarithmic scale. $n = 21$ for all conditions, with one exception: $n = 12$ for large microwell with analyte releasing rate $k_g = 1\ molecule/cell/sec$.

It's noteworthy that the analytical expressions for capture efficiency and CV values (Equation 4.10 and 4.21), which are derived for the case of external source of target analytes, can be used to estimate the impact of different parameter values qualitatively, even in the case of cellular source of target analytes. Thus, when the simulation results are available for a given set of parameters, one could get a rough estimation on the assay performance under different parameter settings by applying the two equations to the available data. In Table 4.2, we list the capture efficiency and CV values of captured analyte number that reasonable systems could achieve in the case of $k_g = 0.1\ \#/cell/sec$ after 1-h,

2-h or 4-h incubation time. It can be used as a guide to estimate the simulation outcomes of other systems and to design the experimental system.

Table 4.2 Capture efficiency and coefficient of variation (CV) in captured analyte number based on the numerical simulations of deterministic continuum model (M1) and stochastic discrete model (M2) in the case of $k_g = 0.1\ \#/cell/sec$.

Parameter Setting*	1-h Incubation			2-h Incubation			4-h Incubation		
	Cap Eff (%)		CV	Cap Eff (%)		CV	Cap Eff (%)		CV
	M1	M2	M2	M1	M2	M2	M1	M2	M2
Standard**	69.59	69.53	0.066	80.90	80.90	0.035	86.64	86.42	0.009
$K_d = 0.1\ nM$	95.29	95.54	0.054	97.27	97.47	0.039	98.26	98.34	0.028
$K_d = 10\ nM$	15.36	15.04	0.155	25.79	25.76	0.070	37.39	36.50	0.051
$[R]_0 = 600\ \#/\mu m^2$	15.14	14.92	0.118	25.31	25.00	0.086	36.66	36.23	0.051
$[R]_0 = 60k\ \#/\mu m^2$	95.46	94.17	0.065	97.34	95.40	0.039	98.30	95.49	0.026
Bead-cell: 0.5μm***	69.75	68.91	0.074	80.96	81.28	0.040	86.67	86.46	0.028
Large	10.79	10.04	0.150	18.62	18.20	0.085	27.78	26.52	0.065
Large: 0.5 μm***	11.92	11.09	0.159	18.50	18.72	0.067	26.81	26.96	0.057

*Only parameters with different values from the standard case are listed.

**Standard case has following parameter settings: small microwell ($50\ \mu m \times 50\ \mu m \times 50\ \mu m$) with only one antibody-coated bead and one analyte-releasing cell, $k_g = 0.1\ \#/cell/sec$, $K_d = 1\ nM$, $[R]_0 = 6k\ molecules/\mu m^2$, default setting for bead-cell distance.

*** The coordinates of cell and bead used for simulation are shown in Figure 4.1F, with 0.5 μm distance between the surfaces of bead and cell.

4.6 Experimental Characterization with Recombinant Protein

Since the readout of immunosandwich assay is fluorescence signal, a calibration curve is usually required to translate the fluorescence signal into the amount of target analytes being detected in the sample. A calibration curve can be obtained by characterizing the assay performance on a series of standard samples containing known amount of target analytes. In this section, we conduct the closed-array immunoassay using the microwell array platform developed in Chapter 3 and characterize its performance in molecule detection. We chose c-Met ectodomain shedding as our experimental model case. c-Met, also known as hepatocyte growth factor (HGF) receptor, is a receptor tyrosine kinase that engages in many signaling pathways and has significant implications in both normal and

pathologic processes [31]. Abnormal activation of c-Met or c-Met overexpression has been widely observed in many cancers where c-Met supports the invasive growth of cancer cells [32]. On the other hand, the active pericelluar proteases could shed away the ectodomain of c-Met from cell surface and generate soluble decoy c-Met which works as a endogenous antagonist for c-Met binding with its ligands. Moreover, ADAM17-dependent c-Met shedding has been shown to involve in the resistance development of KRAS mutant colorectal cancer against MEK inhibitors [33], further emphasizing the importance of studying c-Met shedding in cancer research.

We first characterize the behavior of closed-array immunosandwich assay using large microwell of $100\ \mu m \times 100\ \mu m \times 189\ \mu m$ dimension. As shown in Figure 4.8A, for standard sample of given analyte concentration, we observed a decrease in the average per bead fluorescence signal when there were more antibody-coated beads present in the same sealed microwell. This is in agreement with our computational models. Our experimental setup uses capture antibodies of $K_d < 0.15\ nM$ at surface density of $[R]_0 \approx 6k\ \#/\mu m^2 \approx 10^{-8}\ mol/m^2$ on beads. With parameters of these values, the two models predict that the capture efficiency of entire system within large microwell is ~81 % and ~92% for 1-bead case and 2-bead case, respectively, after 2-h incubation. Thus, in this case, the amount of target analytes being captured by each bead would generally reduce for a closed microwell with more beads present. Besides, for typical optical detection, the signal-to-noise ratio of instrument readout correlates with the density of fluorophores rather than their total amount on beads. Thus, on one hand, in situations where the total amount of target molecules in the system is well below the available binding sites and total capture efficiency is sufficiently high – such as our experimental system for assaying samples with fixed concentration of target molecules, we should use smaller antibody capture area within each microwell for analyte detection to increase the optical detection sensitivity. On the other hand, in situations with low total capture efficiency, which is likely due to poor antibody affinity or large microwell dimension, increasing the capture area (i.e. more beads) would increase the capture efficiency of the entire system significantly and hence enhance the detection sensitivity when integrating the fluorescence signal from all capture area. For simplicity, we would focus on microwells with only one antibody-coated bead in the rest of Chapter 4.

As expected, for both large and small microwell systems, we observed an upward shift in the bead signal distribution of 1-bead case as the concentration of recombinant protein increased (Figure 4.8B, C). When combining data from systems with different microwell sizes, we noticed that the amount of captured analytes correlated more closely to the absolute amount of analytes present within individual sealed microwell rather than the concentration of analytes. For example, standard sample containing $10\ ng/ml$ recombinant protein ($6.4k\ \#/well$ in small well) exhibited a small-well signal distribution resembling the large-well signal distribution of $0.5\ ng/ml$ sample ($4.4k\ \#/well$ in large well). This result also indicated that our experimental system has achieved very high capture efficiency for low-abundance molecules ($< 10k\ \#/well$) and microwell size is not a limiting factor for molecular capture. However, despite the high capture efficiency, the distribution of fluorescence signal for individual beads is very wide under each condition. As shown in Figure 4.8D, standard samples displayed CV of 0.4~0.7 at concentration of $500\sim10k\ \#/$

well and the CV value reduced to ~0.2 when recombinant concentration is ~88k #/*well*. Removing data points with higher than 75th and 90th percentile values of the whole signal distribution does not impact the value of CV significantly, implying that the high magnitude of CV is not due to the presence of minority outliers.

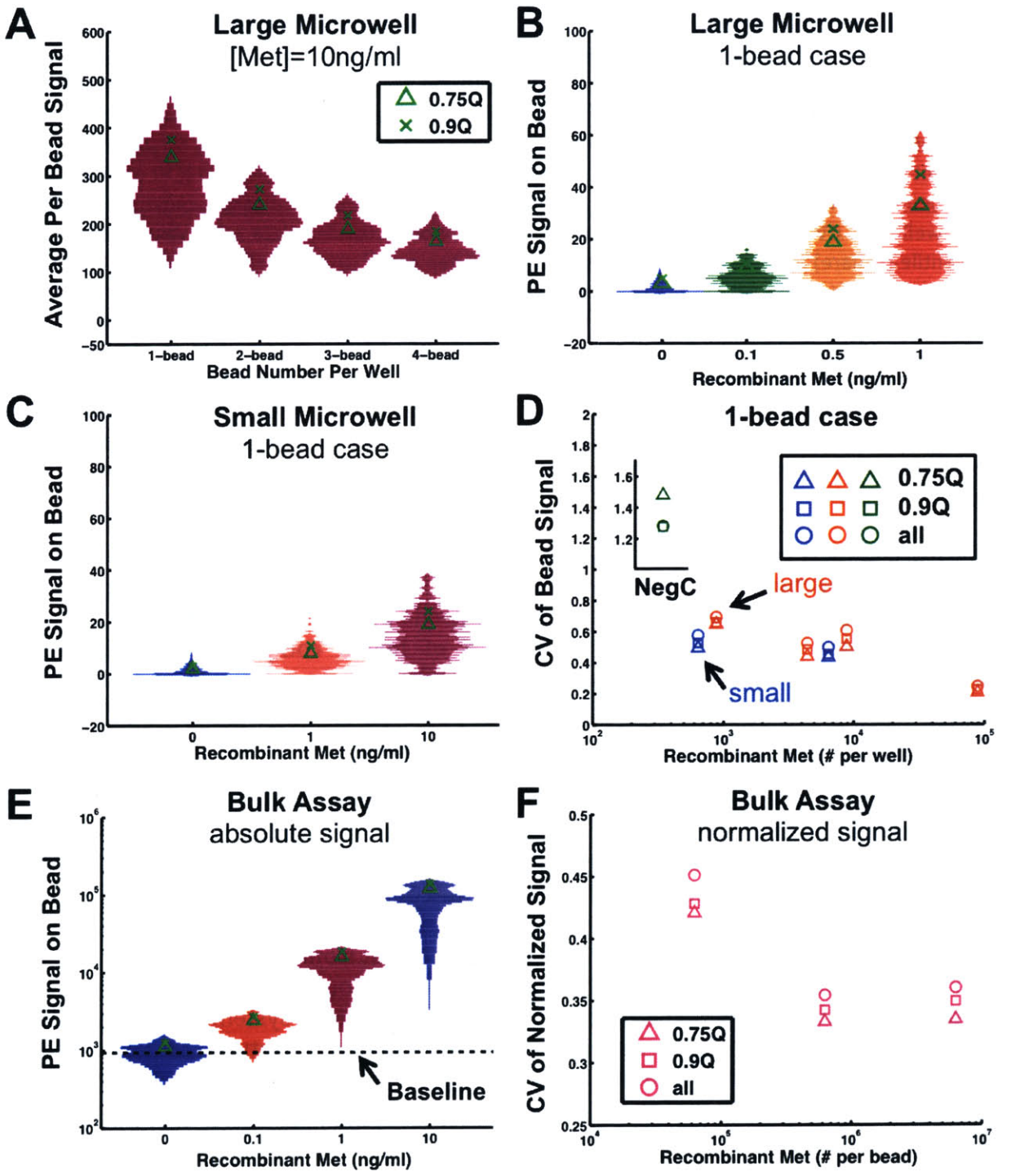

Figure 4.8 Experimental comparisons of close-array detection (**A, B, C, D**) and bulk assay (**E, F**) on standard sample. The fluorescence intensity of beads in PE channel is an indicator for the amount of

target molecules being captured by antibody-coated beads. In close-array immunosandwich assays, the antibody-based capture of target molecules were performed by incubating recombinant c-Met proteins with antibody-coated beads in sealed microwells of different well sizes. In bulk assay, the target capture step was done by mixing antibody-coated beads with 80 μL of sample at ~7500 beads/ml concentration. To evaluate the impact of outliers, the 75th (0.75Q) and 90th (0.9Q) percentile values of data distribution are marked by bright green triangles and crosses, respectively, for each condition. (**A**) Histogram of average per bead PE signal for microwells with 1, 2, 3 or 4 beads in the case of large microwell ($100\ \mu m \times 100\ \mu m \times 189\ \mu m$) and recombinant protein concentration of $10\ ng/mL$ (equivalent to $88k\ molecules/well$ of target analytes). $n > 120$. (**B, C**) Histogram of PE signal on beads for microwells with only 1 bead in the case of large microwell and small microwell ($50\ \mu m \times 50\ \mu m \times 50\ \mu m$), for different concentrations of target molecules. $n > 450$. (**D**) Coefficient of variation (CV) of bead PE signal for 1-bead case in closed-array immunosandwich assays, as a function of target molecule number per microwell. The CV values were calculated for all data points (circle), data with values less than 90th percentile (square) and data with values less than 75th percentile (triangular), respectively. Blue markers represent the CV values for results from assays with small microwells. Red markers are for results from assays with large microwells. Dark green markers depict the results from negative control sample. (**E**) Histogram of PE signal on beads in the case of immunosandwich assays at bulk level. The black dashed line marks the median PE intensity of negative control (NegC) with target analyte concentration equal to zero. This value is considered as the baseline intensity for bulk assay. (**F**) Coefficient of variation (CV) of normalized bead PE signal for bulk assay, as a function of average target number per bead. The normalized bead PE signal is calculated by subtracting the baseline intensity from the original bead signal. $n > 200$.

There are several causes of this wide data scattering. On one hand, as discussed in section 4.3, thermal fluctuations could generate 0.01~0.05 CV in the exact number of target analytes being encapsulated within each microwells at concentration of $500\sim10k\ \#/well$ and this would translate directly to the CV of bound complex at equilibrium. The probabilistic nature of binding reaction also results in data scattering and gives rise to additional 0.002~0.01 and 0.01~0.05 CV in the case of small and large microwell, respectively, at concentration of $500\sim10k\ \#/well$ (Figure 4.4). On the other hand, there are practical factors contributing to data scattering, including variation in bead quality (size, fluorescence background signal, antibody coating efficiency, etc), artifacts in optical detection and fluorescence signal processing (uneven illumination, image background subtraction, etc), and non-uniform dye aggregation during the downstream binding step of biotinlyated detection antibody and streptavidin-conjugated PE fluorophores. Firstly, for the variation in bead quality, we have done pre-screening to remove antibody-coated beads with abnormal size and fluorescence background signal from our analysis and thus these two factors should not be the primary contributor of readout variation in our experimental system. Secondly, by applying Equation 4.12 to our experiment system, we realized that the impact of different binding site densities on the fluctuations of captured target number was relatively small. Given high affinity antibodies ($K_D \approx 0.15\ nM$), large average binding site density ($[R]_0 \approx 10^{-8}\ mol/m^2$) and small microwell dimension ($V_{well} = 0.125\ nL$ or $1.89\ nL$), 10% CV in $[R]_0$ would only result in roughly 1% CV in $[C]_{eq}$. Thus, variation in antibody coating efficiency is unlikely to be the primary source of readout variation either. Thirdly, to evaluate the impact of optical detection, we characterized the immunosandwich assay at bulk level by incubating antibody-coated beads with standard samples (of fixed total target amount) in tubes and measuring the fluorescence signal via

flow cytometer, which has more uniform optical condition than that in microscopy imaging of microwell array. For bulk assay, each bead can sample a large volume in its neighborhood (characteristic diffusion distance $l_v \sim 1mm$). Hence, the average amount of analytes being sampled by each antibody-coated bead is high and not sensitive to thermal fluctuations. The absolute signal obtained by bulk assay also scattered over a wide range of values, despite its good correlation with sample concentration (Figure 4.8E). After subtracting the baseline signal (i.e. median fluorescence signal of negative control) from raw data of bulk assay, the normalized signal has ~0.45 CV at sample concentration of $0.1\,ng/ml$ ($\sim 62.6k\ molecules/bead$) and decreases its CV to ~0.35 when sample concentration further increased (Figure 4.8F). Compared to the CV values (0.5~0.6) given by the closed-array assay at $\sim 10k\ molecules/well$, bulk assay gave only slightly lower CV value with similar per bead/well target amount. Thus, artifacts in optical detection should not contribute to experimental readout variation significantly. What remain for further study are the artifacts in fluorescence signaling processing procedure and the non-uniform dye aggregation during downstream step of the assay. Minimizing the impact of these two practical factors might help to improve the detection resolution of closed-array immunosandwich assay. Taken together, these results suggest that experimental artifacts, rather than the intrinsic noise derived from detection mechanism, are the major contributors of the data scattering observed in closed-array immunosandwich assay with standard samples of fixed total target amount. One should take into account those non-biological sources of data scattering when translating results of single-cell shedding assay using similar platform into the biological variability of cells.

4.7 Detection of Single-Cell Shedding in Closed Array

We then conduct single-cell shedding assay to quantify c-Met shedding of parental HCC827 cells using antibody-coated beads and sealable microwell array. Parental HCC827 contains mutation in EGFR gene and is a cell line for non-small cell lung cancer. Minor subpopulation of parental HCC827 cells has been discovered to harbor MET amplification and thought to be the origins of resistant HCC827 cells that also exhibit gene amplification in MET and emerge after long-term treatment of tyrosine kinase inhibitors (TKI therapy)[34]. Single-cell detection of c-Met ectodomain shedding would then provide unique insights for the study of resistance development in non-small cell lung cancer.

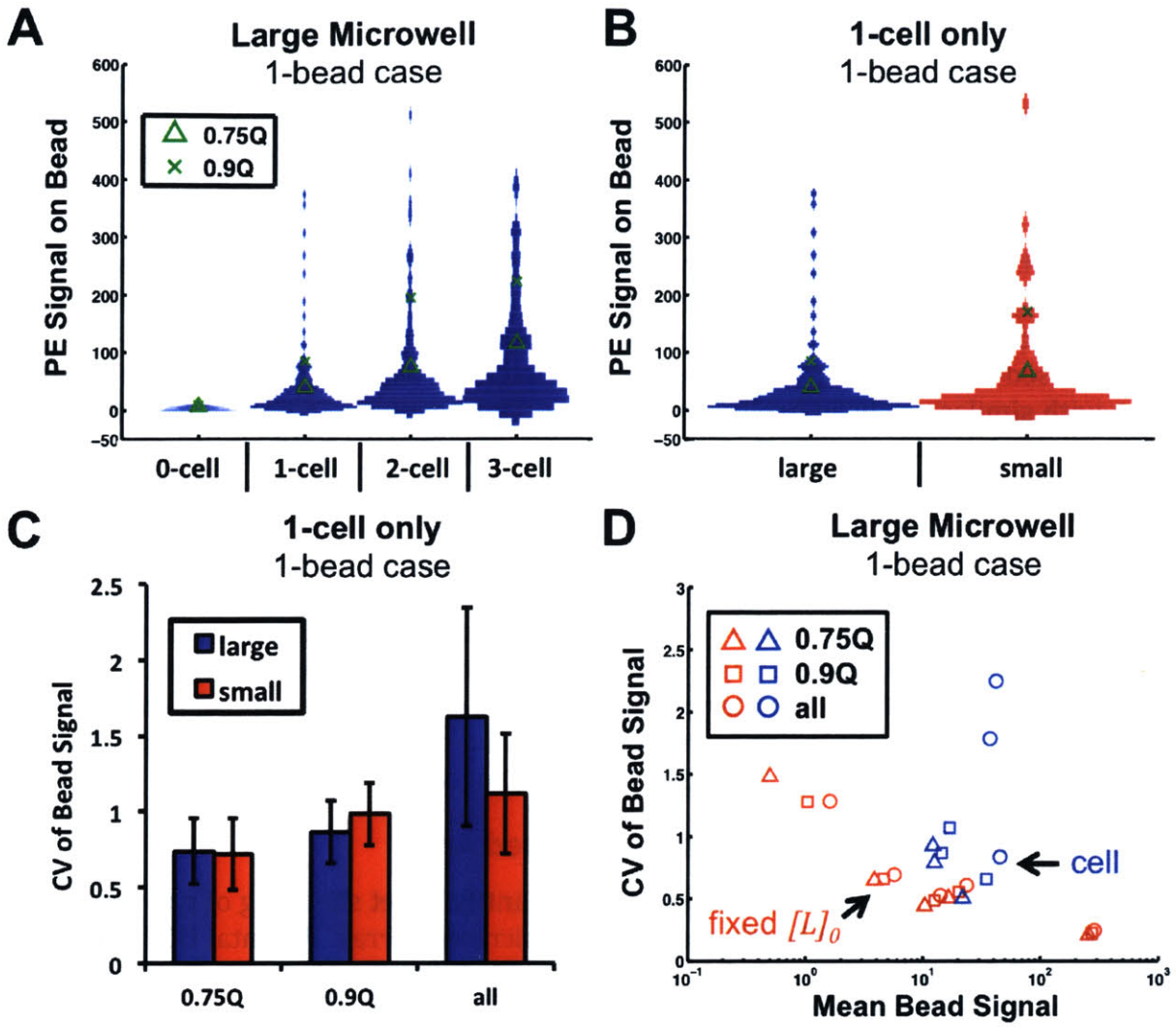

Figure 4.9 Quantification of c-Met ectodomain shedding of parental HCC827 cells using closed-array Immunosandwich assay. The fluorescence intensity of beads in PE channel is an indicator for the amount of shed c-Met molecules being bound onto the antibody-coated beads. To evaluate the impact of outliers, the 75th (0.75Q) and 90th (0.9Q) percentile values of data distribution are marked by bright green triangles and crosses, respectively, for each condition. (**A**) Histogram of PE signal on beads for microwell with only one antibody-coated bead but different number of cells in the case of large microwell ($100\ \mu m \times 100\ \mu m \times 189\ \mu m$). $n > 100$. (**B**) Histogram of PE signal on beads for microwell with only one bead and one cell in the case of small (red, $50\ \mu m \times 50\ \mu m \times 50\ \mu m$) and large microwell (blue). $n > 80$. (**C**) Coefficient of variation (CV) of bead PE signal for 1-bead, 1-cell case in closed-array immunosandwich assays. Error bars represent standard deviation from a triplicate using three different cell-loaded arrays. (**D**) Coefficient of variation (CV) of bead PE signal as a function of mean bead signal for large microwells containing only one antibody-coated bead. X-axis represents mean fluorescence signal of 1-bead well in log scale. Blue marks are for the data from a triplicate of single-cell shedding assays. Red marks depict the data taken from Figure 4.8D and are for closed-array immunosandwich assay using standard samples containing recombinant c-Met protein at $0.1, 0.5, 1, 10\ ng/ml$, respectively. The CV values were calculated for all data points (all), data with values less than 90th percentile (0.9Q) and data with values less than 75th percentile (0.75Q), respectively.

As shown in Figure 4.9A, the distribution of bead fluorescence signal shifts upwards as the number of cells within the closed microwell increases, indicating a positive correlation between the total amount of shed c-Met molecules and the cell number. Moreover, we observed slightly higher mean fluorescence signal for microwells containing only one HCC827 cell in the case of small microwell than that in large microwell case (Figure 4.9B), which is probably due to the higher capture efficiency within smaller microwell and is in agreement with our simulation results (Figure 4.6E). Furthermore, cell-containing microwells displayed wider distribution of bead signal with CV >0.7 (Figure 4.9D), as compared to the corresponding assays with standard samples ($0.5\sim10\ ng/ml$) where recombinant protein-filled microwells showed similar mean fluorescence signal but lower CV (<0.6). Notably, the data scattering observed in assays of standard samples dictates the resolution of quantification at which one can distinguish between cells with different shedding rates. Thus, the higher CV observed in single-cell assays reveals the existence of biological variability among the c-Met shedding rate of individual cells. Nevertheless, it remains difficult to translate the fluorescence readout of single-cell assays into the shedding rate for individual cells with high precision due to the large CV observed in their counterpart assays with standard samples. Further efforts in minimizing the experimental artifacts are necessary to improve the resolution of quantifying low-abundance shed molecules at single-cell level.

4.6 Section Summary

Protease-mediated molecular shedding plays an important role in extracellular signaling network and involves in disease progression of cancer and drug resistance development. Single-cell measurement on molecular shedding would help to enrich our understanding on those pathological processes and potentially shed lights on novel therapies. While immunosandwich assays in conjugated with microfluidic-based spatial confinement have enable quantitative detection of antibody production and cytokine secretion at single-cell level, the applicability of those assays in single-cell shedding regime, which has much lower target generation rate, has not been exclusively characterized. In this chapter, we have discussed the theoretical limits of low-abundance molecule detection and identified fluctuations in source concentrations and binding kinetics as the origins of intrinsic noise derived from binding-based detection mechanism. With the aid of numerical simulations on both deterministic continuum model and stochastic discrete model, we then further characterize the operational envelope for closed-array immunosandwich assay as a function of microwell size, antibody affinity, binding site density and the abundance of target analytes. We also evaluate the impact of stochastic events (e.g. the discrete processes of molecule diffusion and reaction) on assay performance with an emphasis on intrinsic detection uncertainty (coefficient of variation, CV). Lastly, we characterize the assay performance experimentally using standard samples and live HCC827 cells. The experimental results suggest that practical factors, particularly the non-uniform dye aggregation and artifacts in fluorescence signal processing, are the primary determinants of assay resolution at which one can distinguish between cells with different shedding rates. While the impacts of those practical factors on assay outcomes need to be further minimized for quantitative measurement, it's essential to consider those non-biological sources of data scattering when extracting the level of biological variability from raw

binding outcomes of immunosandwich assays. In summary, this chapter has provided a careful characterization on binding-based molecule detection in closed configuration and could guide the upstream design and downstream analysis of single-cell shedding measurement.

4.7 Section Acknowledgements

The thesis contributor would like to thank Ms. Allison M. Claas for conducting the standard Luminex assays and the helpful discussions. The work in this chapter is financially supported by the Singapore-MIT Alliance for Research and Technology (SMART) Centre (BioSyM). The numerical simulations on stochastic discrete model are performed using MCell, whose development is supported by the NIGMS-funded (P41GM103712) National Center for Multiscale Modeling of Biological Systems (MMBioS).

4.8 References

[1] Athauda, G., et al., *c-Met Ectodomain Shedding Rate Correlates with Malignant Potential.* Clinical Cancer Research, 2006. **12**(14): p. 4154-4162.

[2] Han, Q., Bradshaw, E.M., Nilsson, B., Hafler, D.A., and Love, J.C., *Multidimensional analysis of the frequencies and rates of cytokine secretion from single cells by quantitative microengraving.* Lab on a Chip, 2010. **10**(11): p. 1391-1400.

[3] Konry, T., Golberg, A., and Yarmush, M., *Live single cell functional phenotyping in droplet nano-liter reactors.* Scientific Reports, 2013. **3**: p. 3179.

[4] Warren, L., Bryder, D., Weissman, I.L., and Quake, S.R., *Transcription factor profiling in individual hematopoietic progenitors by digital RT-PCR.* Proceedings of the National Academy of Sciences, 2006. **103**(47): p. 17807-17812.

[5] Sakakihara, S., Araki, S., Iino, R., and Noji, H., *A single-molecule enzymatic assay in a directly accessible femtoliter droplet array.* Lab on a Chip, 2010. **10**(24): p. 3355-3362.

[6] Zhu, H., et al., *Detecting Cytokine Release from Single T-cells.* Analytical Chemistry, 2009. **81**(19): p. 8150-8156.

[7] Jin, A., et al., *A rapid and efficient single-cell manipulation method for screening antigen-specific antibody-secreting cells from human peripheral blood.* Nat Med, 2009. **15**(9): p. 1088-1092.

[8] Torres, A.J., Hill, A.S., and Love, J.C., *Nanowell-Based Immunoassays for Measuring Single-Cell Secretion: Characterization of Transport and Surface Binding.* Analytical Chemistry, 2014. **86**(23): p. 11562-11569.

[9] Henn, A.D., et al., *Modulation of Single-Cell IgG Secretion Frequency and Rates in Human Memory B Cells by CpG DNA, CD40L, IL-21, and Cell Division.* The Journal of Immunology, 2009. **183**(5): p. 3177-3187.

[10] Charlet, M., Kromenaker, S.J., and Srienc, F., *Surface IgG content of murine hybridomas: Direct evidence for variation of antibody secretion rates during the cell cycle.* Biotechnology and Bioengineering, 1995. **47**(5): p. 535-540.

[11] Regehr, K.J., et al., *Biological implications of polydimethylsiloxane-based microfluidic cell culture.* Lab on a Chip, 2009. **9**(15): p. 2132-2139.

[12] Merkel, T.C., Bondar, V.I., Nagai, K., Freeman, B.D., and Pinnau, I., *Gas sorption, diffusion, and permeation in poly(dimethylsiloxane).* Journal of Polymer Science Part B: Polymer Physics, 2000. **38**(3): p. 415-434.

[13] Wang, J., Douville, N., Takayama, S., and ElSayed, M., *Quantitative Analysis of Molecular Absorption into PDMS Microfluidic Channels.* Annals of Biomedical Engineering, 2012. **40**(9): p. 1862-1873.

[14] Linderman, J.J., Mahama, P.A., Forsten, K.E., and Lauffenburger, D.A., *Diffusion and Probability in Receptor Binding and Signaling*, in *Advances in Chemical Engineering*, W. James, Editor. 1994, Academic Press. p. 51-127.

[15] Frykman, S. and Srienc, F., *Quantitating secretion rates of individual cells: Design of secretion assays.* Biotechnology and Bioengineering, 1998. **59**(2): p. 214-226.

[16] Liao, W., Wei, F., Qian, M.X., and Zhao, X.S., *Characterization of protein immobilization on alkyl monolayer modified silicon(1 1 1) surface.* Sensors and Actuators B: Chemical, 2004. **101**(3): p. 361-367.

[17] Pellequer, J.L. and Van Regenmortel, M.H.V., *Measurement of kinetic binding constants of viral antibodies using a new biosensor technology.* Journal of Immunological Methods, 1993. **166**(1): p. 133-143.

[18] Kerr, R., et al., *Fast Monte Carlo Simulation Methods for Biological Reaction-Diffusion Systems in Solution and on Surfaces.* SIAM Journal on Scientific Computing, 2008. **30**(6): p. 3126-3149.

[19] Stiles, J.R. and Bartol, T.M., *Monte Carlo Methods for Simulating Realistic Synaptic Microphysiology Using MCell*, in *Computational Neuroscience: Realistic Modeling for Experimentalists*, E.D. Schutter, Editor. 2001, CRC Press. p. 87-127.

[20] Berg, H.C. and Purcell, E.M., *Physics of chemoreception.* Biophysical Journal, 1977. **20**(2): p. 193-219.

[21] Lauffenburger, D.A. and Linderman, J.J., *Receptors : Models for Binding, Trafficking, and Signaling: Models for Binding, Trafficking, and Signaling.* 1993: Oxford University Press, USA.

[22] Bialek, W. and Setayeshgar, S., *Physical limits to biochemical signaling.* Proceedings of the National Academy of Sciences of the United States of America, 2005. **102**(29): p. 10040-10045.

[23] Bialek, W. and Setayeshgar, S., *Cooperativity, Sensitivity, and Noise in Biochemical Signaling.* Physical Review Letters, 2008. **100**(25): p. 258101.

[24] Tranquillo, R.T., *Theoreis and models of gradient perception*, in *Biology of the Chemotactic Response*, J.P. Armitage and J.M. Lackie, Editors. 1990, Cambrige Univ. Press: Cambridge, UK. p. 35.

[25] Tranquillo, R.T. and Lauffenburger, D.A., *Analysis of leukocyte chemosensory movement.* Advanced Biosciences, 1987. **66**: p. 29-38.

[26] Gillespie, D.T., *Exact stochastic simulation of coupled chemical reactions.* The Journal of Physical Chemistry, 1977. **81**(25): p. 2340-2361.

[27] Gardiner, C., *Stochastic Methods: A Handbook for the Natural and Social Sciences.* 4 ed. 2009: Springer Berlin Heidelberg.

[28] Rhee, H.-K., Aris, R., and Amundson, N.R., *First-Order Partial Differential Equations.* Vol. 1. 1986, Englewood Cliffs, N. J.: Prenticel-Hall.

[29] Brouzes, E., et al., *Droplet microfluidic technology for single-cell high-throughput screening.* Proceedings of the National Academy of Sciences, 2009. **106**(34): p. 14195-14200.
[30] Love, J.C., Ronan, J.L., Grotenbreg, G.M., van der Veen, A.G., and Ploegh, H.L., *A microengraving method for rapid selection of single cells producing antigen-specific antibodies.* Nat Biotech, 2006. **24**(6): p. 703-707.
[31] Organ, S.L. and Tsao, M.-S., *An overview of the c-MET signaling pathway.* Therapeutic Advances in Medical Oncology, 2011. **3**(1 Suppl): p. S7-S19.
[32] Gentile, A., Trusolino, L., and Comoglio, P., *The Met tyrosine kinase receptor in development and cancer.* Cancer and Metastasis Reviews, 2008. **27**(1): p. 85-94.
[33] Van Schaeybroeck, S., et al., *ADAM17-Dependent c-MET-STAT3 Signaling Mediates Resistance to MEK Inhibitors in KRAS Mutant Colorectal Cancer.* Cell Reports, 2014. **7**(6): p. 1940-1955.
[34] Turke, A.B., et al., *Pre-existence and clonal selection of MET amplification in EGFR mutant NSCLC.* Cancer cell, 2010. **17**(1): p. 77-88.

Chapter 5 Conclusions

As the increasing recognition of cell-to-cell heterogeneity in many biological and clinical problems, the demands for tools and methodologies enabling single-cell study on various aspects keep booming. But there are still many unmet needs in each phase of single-cell study, including sample preparation, single-cell measurement and data interpretation. Driven by the those needs in current single-cell study, this thesis seeks to contribute to the field by providing (1) tool facilitating sample preparation, (2) platform enabling activity measurement of cellular microenvironment, and (3) critical analysis on the limits of antibody- based analyte quantification for single-cell proteomic study.

Sample preparation is often an essential step of single-cell study, particularly in the case where minority of the cell population is the matter of interest. Size-based cell separation has been recognized as an important label-free approach for enriching the rare cells for downstream study. However, the throughput, separation resolution and artificial impact on cell state remain problematic, especially when it comes to sensitive primary cells in blood. In Chapter 2, we investigate the particle focusing and separation behavior within curved microfluidic channel and develop a novel inertial cell sorter for high-throughput size-based cell separation. The novel design of cell sorter consists of a 1-inlet, 2-outlet spiral microfluidic channel with trapezoid cross-section and has higher separation resolution than the conventional spiral cell sorter with rectangular cross-section. We demonstrate the capacity of the novel cell sorter in isolating sensitive leukocytes from blood (1~2% hematocrit) with high efficiency (>80%) but no artifacts on the immunophenotypes of isolated cells. Our design of size-based cell sorter holds a promising solution for many other size-based cell separation problems and such cases include isolation of circulating tumor cells from blood and enrichment of mesenchymal stem cells from bone marrow aspirates. Besides, since cell size is an important attribute in single-cell study due to its unique impact on cellular design and function of individual cells, our novel size-based cell sorter would facilitate downstream single-cell study by simplifying the system and enriching rare subpopulation with potential distinct functionality.

In Chapter 3, we focus on the single-cell measurement phase. While the activity of pericelluar proteases, including both those secreted and expressed on surface, plays a significant role in regulating the microenvironments of individual cells, there is no available tool for activity measurement of those proteases at single-cell level. We thus establish a microfluidic platform enabling functional characterization of pericellular proteases on many single cells simultaneously in a time-dependent manner. The platform works for both suspension cells and adherent cells, and is compatible with other image-based detection methods. By applying our platform to study PMA-mediated protease response of HepG2 cells, we demonstrate that single-cell protease activation upon drug stimulation could be heterogeneous not only in terms of activity magnitude but more surprisingly with respect to temporal profile - with cells exhibiting transient activity increase asynchronously. Moreover, we explore the behavior of single-cell protease activity in the settings of anti-cancer drug resistance development using parental and gefitinib-

resistant HCC827 cells. The preliminary results of single-cell measurements exhibit deviation from the population-averaged assay outcomes and suggest a potential role of cell death and cell-cell communication on the protease response of HCC827 cells at bulk level. Therefore, our platform offers prospect for studying the roles of pericellular protease activities in governing cell behaviors in a context-dependent manner.

Chapter 4 addresses the resolution problem in data interpretation phase, when it comes to low-abundance molecule detection. Quantification of molecules at extremely low abundance is critical for proteomic study of single cells. Current methods for single-cell molecule detection usually relies on the antibody-mediated capture for target quantification (e.g. immunosandwich assay) and employs spatial confinement of individual cells to increase the target concentration for better detection sensitivity. However, in the case of protease-mediated molecular shedding, the target generation rate by individual cells is often lower than 1 *molecule/cell/sec* and hence imposes significant challenges in detecting the target analytes quantitatively. Using our sealable microwell platform developed in Chapter 3 as the experimental system, we build the corresponding theoretical model for low-abundance molecular capture within closed microwell in form of both the deterministic continuum system and stochastic discrete system. With the aid of numerical simulations, we then perform critical characterization on the operational envelope for immunosandwich assay in closed configuration, with an emphasis on the ultimate limits of detection uncertainty that is intrinsic to binding-based detection mechanisms. Lastly, we experimentally characterize the assay performance with standard samples and live HCC827 cells, and identify experimental artifacts, particularly the non-uniform dye aggregation and artifacts in fluorescence signal processing, as the primary determinants of detection resolution in actual experiment. Thus, Chapter 4 highlights the necessity in considering those non-biological sources of data scattering when interpreting the detection outcomes of binding-based single-cell molecule measurements. It also serves as a guide for proper experimental design and downstream analysis of single-cell shedding measurement.

Appendix

A.1 Supporting Information for Chapter 3

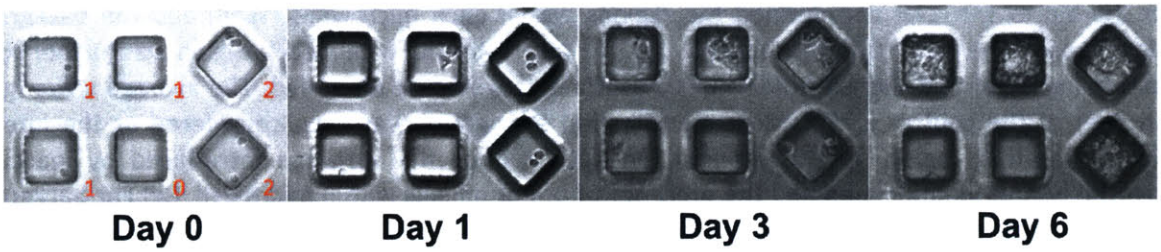

Figure A.1 Representative images for HepG2 cells cultured on collagen-coated microwell array. The red digits indicate the number of cells in each microwell immediately after seeding on Day 0. Cell spreading and proliferation was observed over time during complete medium culture. And the images were taken using a phase contrast microscope.

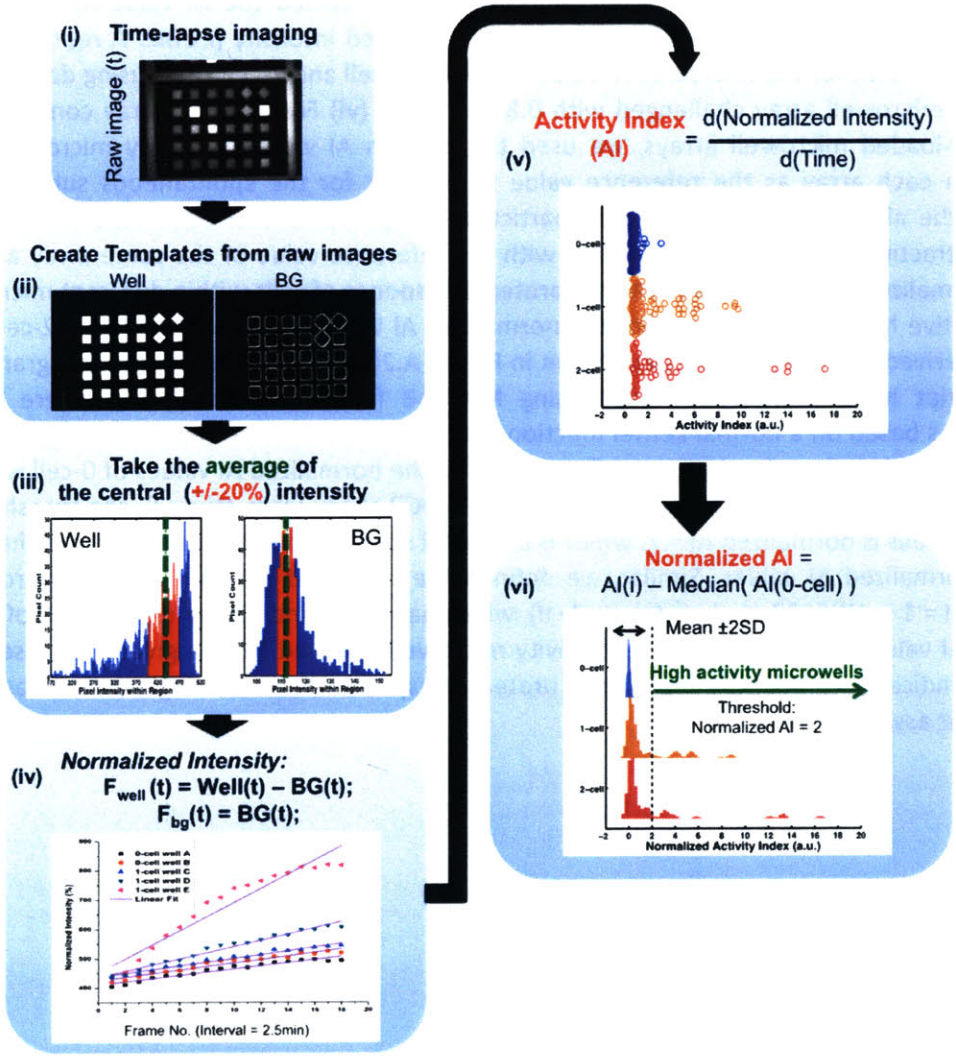

Figure A.2 Schematic for signal acquisition, processing and normalization. (**i**) The time-lapse raw images for the substrate cleavage were captured by fluorescence inverted microscope and then stabilized using Image Stabilizer plugin of Image J® software. Given the non-uniform illumination within observation window and the well-to-well interference due to light scattering, a normalization method was developed for signal processing. (**ii**) Briefly, two templates were generated based on the raw images with the aid of MATLAB and defined the regions within each microwells (Well) and the background regions around the wells (BG), respectively. (**iii**) The pixel intensity within each region was further sorted in ascending order and the extreme values at both ends would be discarded. The average value (green dash line) of the central ± 20% pixel intensity (red histogram) was then considered as the intensity indicator for that region. In this manner, one can reduce the variation introduced by inaccurate microwell border identification and the presence of bright objects within microwell. (**iv**) For background regions, the average value became the normalized intensity. But for microwell regions, the average value of each well region was further subtracted by the normalized intensity of its surrounding background region. Then, one can obtain time-lapse profile of normalized intensity for individual microwells. Example profiles of microwells with 0 or 1 cell are shown here. (**v**) We modeled the protease-mediated substrate cleavage as the classical Michaelis-Menten model, where the initial rate of cleavage is proportional to the concentration of active enzyme in the system with excessive substrate of nearly constant concentration. Therefore, we defined the protease activity index (AI) as the increasing rate (i.e. slope) of normalized fluorescence intensity and extracted the AI value for each region via robust linear least-squares fitting of the time-lapse normalized intensity profile. A representative "bee swarm" plot is shown for the microwell AI values of 0-cell, 1-cell and 2-cell wells using data derived from a cell-loaded microwell array challenged with 0.8 μM PMA. (**vi**) For array-to-array comparison among different cell-loaded microwell arrays, we used the median AI value of empty microwells (negative control) from each array as the reference value to account for the spontaneous substrate cleavage occurred in the absent of cells within that particular array. We further calculated the normalized AI value by subtracting each microwell AI value with the reference value of the same array and used the resultant normalized AI value to evaluate the protease response of cells within different microwell array. A representative histogram is shown for the normalized AI values of 0-cell, 1-cell and 2-cell wells, and the data is derived from the same assay shown in Figure A.2(v). Notice that all the histograms shown in this manuscript have been smoothened using MATLAB function *ksdensity().m* where the density estimation was based on a normal kernel function and the locations of kernel smoothing windows were robustly estimated via function *histogram().m*. Based on the normalized AI values of 0-cell wells, we also defined a threshold for high activity microwells. For HepG2 study (case study I), the threshold for high activity microwells is normalized AI = 2, which is beyond 2 standard deviations away from the mean of 0-cell wells' normalized AI values. Similar, we defined the threshold for high activity microwells to be normalized AI = 1 in HCC827 study (case study II), which has lower and tighter distribution of 0-cell wells' normalized AI values. Percentage of high activity microwells derived from a given protease assay then provides an indicator to quantify the overall protease response of all the single cells measured during that particular assay.